Doklady Physics, Vol. 46, No. 12, 2001, pp. 829–831. Translated from Doklady Akademii Nauk, Vol. 381, No. 4, 2001, pp. 469–471.

PHYSICS

On the Fractal Kinetics of a Nonequilibrium Polyacenequinone Surface

R. V. Afanas'eva, A. A. Maksimov, and T. G. Ermakova

Presented by Academician M.G. Voronkov July 10, 2001

Received July 30, 2001

Previously, we have analyzed features of the dielectric dispersion observed in the polyacenequinone (PAQ) spectrum, namely, in its low-frequency (LF) and high-frequency (HF) regions (Fig. 1a) [1, 2]. These regions of dielectric absorption are interpreted in the framework of concepts used in semiconductor physics. We imply processes of the recharging of adsorptive surface states associated with oxygen adsorption, as well as energy levels of deep bulk centers in the surface regions of space charge for PAQ granules [2]. The question of the nature and chemical structure of the active-center surface forming the system of adsorptive bonds with oxygen was not discussed in this case, due to the absence of information on the PAQ structure. In this paper, we consider the effect of temperature variation on the dielectric spectrum with allowance for scanning electron-microscopy data for the PAQ-granule surface.

As is seen from Fig. 2, layered structural formations are intrinsic to the supermolecular organization of PAQ produced by the cyclopolycondensation of pyrene with pyromellitic dianhydride in the melt. The X-ray analysis data for PAQ, coke and graphite indicate their graphite-like structure. Therefore, we can assume that the adsorbed oxygen interacts with the polyaromatic layers, whose scale is limited by graphite-like fragments of the PAQ structure according to the intercalation mechanism. Comparison of the dielectric spectra for PAQ and the planar polyaromatic complex of naphthalene with iodine [3] (Figs. 1b and 1c) confirms the validity of this assumption. This implies that the independence of temperature for the frequency position $\nu_{m,\,lf}$ of the LF dispersion within the range from –60 to +20°C [2] can be interpreted starting from the concepts used for either the description of electron transport in biopolymers or the tunneling of electrons in the donor–acceptor (D–A) system [4]. The irreversibility of electron transitions (i.e., fixation of an electron at the acceptor) provides proceeding short-time (~10^{-13} s) dissipative processes in the interactions of a tunneling electron with the high-frequency modes of the nearest neighboring D–A groups [4]. In our case, this corresponds to the charged form of oxygen adsorption.

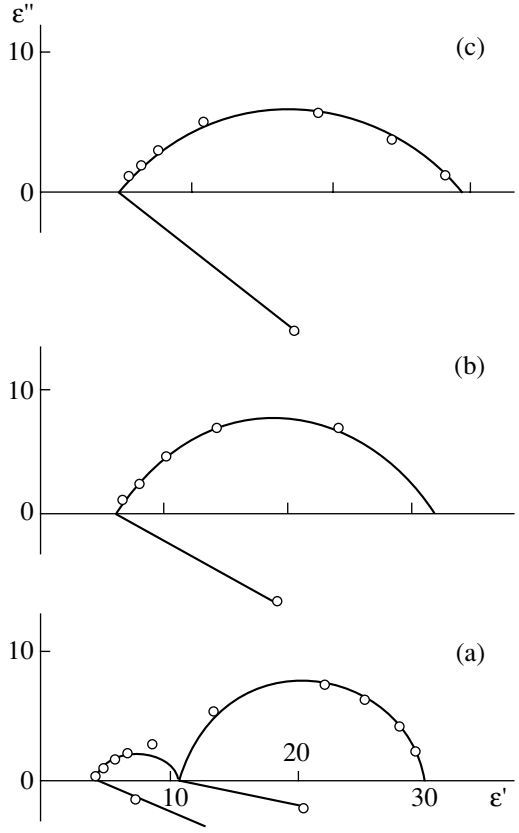

Fig. 1. Cole–Cole diagrams for (a, b) pressed PAQ samples and (c) plane polyaromatic naphthalene–iodine complexes at room temperature: (a) 5-h synthesis duration; the sample 183 μm thick is pressed at a pressure of 0.01 GPa; the diameter of silver electrodes is 8.9 mm; the measurements are carried out immediately after the reversible electric breakdown; the electric field frequencies are 0.004, 0.006, 0.02, 0.15, 0.5, 1.5, 5.0, 30 MHz [1]; (b) 5-h synthesis duration; the sample is 250 μm thick; the diameter of silver electrodes is 8.9 mm; the measurements are carried out immediately after pressing; the electric field frequencies are 0.15, 0.5, 1.5, 5.0, 10 MHz; (c) the sample thickness is 500 μm; the diameter of silver electrodes is 1 cm; the measurements were carried out immediately after pressing; the electric field frequencies are 0.01, 0.05, 0.15, 1.5, 5.0, 12 MHz.

Favorsky Irkutsk Institute of Chemistry, Siberian Division, Russian Academy of Sciences,
ul. Favorskogo 1, Irkutsk, 664033 Russia

1028-3358/01/4612-0829$21.00

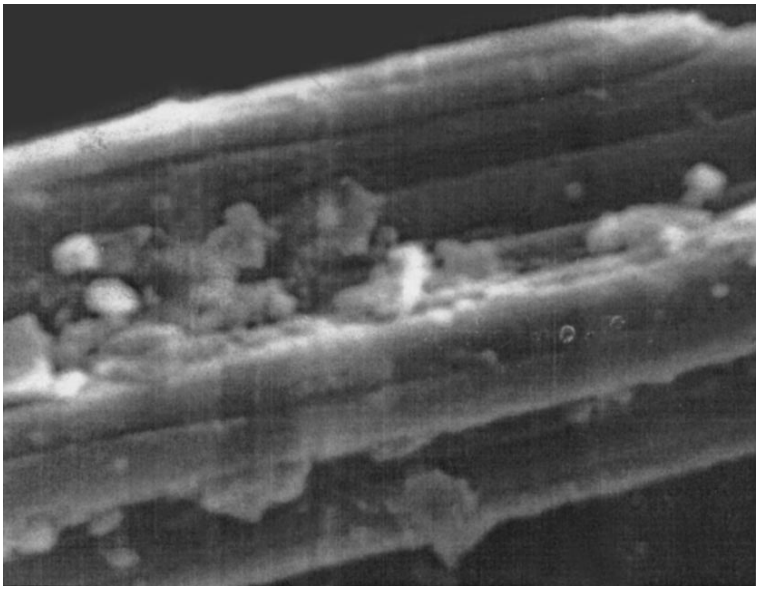

Fig. 2. Microphotograph of the surface of a PAQ granule. The microphotograph is obtained by the methods of scanning electron microscopy (the synthesis duration is 24 h, ×36000).

In the absence of dissipation, we can consider the two-level quantum system as the simplest model of a D–A pair with a tunneling electron. Such models are presently being intensely studied in connection with the problem of incoherence in quantum devices intended for information processing [5, 6]. The component type of quantum computers is conventionally associated [5] with individual units of a medium, which are intrinsic to quantum optics. Manifestation of quantum effects in the phenomenon of dielectric polarization [7] is less known. Incidentally, their studies are of interest specifically in connection with the incoherence problem. In theory of open quantum systems being continuously measured [6], a specific dissipative process is discussed that results not in a rigid but gradual incoherence. According to [6], such a process of measuring a quantum system "can be realized as a long series of soft short interactions of a two-level system with a certain auxiliary system." In our opinion, such a possibility relates to a fractal kinetics of relaxing systems, which determines the deviation of the relaxation law from the Debye exponent [8, 9]. The concept of a discontinuous self-similar process of relaxation [9] is associated with the fractal interpretation [8, 9] of the distribution parameter of relaxation times in the Cole–Cole dependence. In this case, the time periods that correspond to the elementary events of electron-vibrational interactions are grouped into self-similar clusters on the time axis and represent a fractal set. According to [8, 9], the dimensionality $0 < D < 1$ of this set can be determined from the experimental dependence $\varepsilon''(\varepsilon')$ (Fig. 1) (i.e., of the imaginary and real parts of the complex dielectric permittivity, respectively).

Allowing for these concepts, we can interpret the LF dispersion (Fig. 1a) as a probable manifestation of the coherent superposition of two quantum electron states in a D–A system, i.e., as a quantum-information *q*-bit. However, the LF-relaxation process is not independent. The experimental evidence for the interconnection of LF and HF processes of dielectric relaxation is the existence of a common temperature range, in which both the constant behavior of $\nu_{m,\,lf}(T)$ and the correlation of $\nu_{m,\,lf}(T)$ with the temperature dependence of electrical conduction σ for pressed PAQ samples is observed [2]. The interconnection of LF and HF processes of dielectric relaxation reflects an extremely important feature of the incoherence phenomenon in the case under consideration. This feature consists in the necessity of taking into account the probability of two random events that correspond to the charged and neutral forms of oxygen adsorption [4]. Their interrelation, along with the recombination kinetics, determines the concentration of charge-free carriers at the critical net of the percolation cluster.

In the general case, the fractal kinetics corresponds to the specific kinetic schemes representing the complex combinations of serial and parallel relaxation channels, which determines the dynamics with hierarchic constraints [10]. In biophysics, such behavior is considered within the framework of the concept of electron-conformational interactions that take into account the concrete molecular-kinetic mechanisms of cooperative interactions within D–A systems (including the nearest neighbors) [4]. The physical realization of the fractal kinetics can be stipulated (in accordance with this concept) by the processes of the formation of cer-

tain steric conditions favoring or preventing the electron transfer between a donor and an acceptor.

Thus, we can assume that the appearance of the double dielectric dispersion in the PAQ spectrum and the indicated features of its behavior represent the experimentally observed manifestation of a certain sequence of elementary stages in fractal kinetics. This implies that in such a chain of cause-and-effect links of elementary events that characterize the interaction of the quantum system with the vibrational degrees of freedom related to its environment, information representing the result of these interactions is coded. The fractal dimensionality $0 < D < 1$ [8, 9], which determines the form of the $\varepsilon''(\varepsilon')$ dependence, represents (within the framework of such an interpretation) an extremely compact form of recording this information, and the value of the electrical conductance of the pressed PAQ sample reflects the transformation of the quantum information into an electric-current signal. This implies that the hierarchically cosubordinated nonequilibrium system of interrelated electronic and vibrational degrees of freedom, which are localized in the supermolecular PAQ structure, is equivalent to the functionally integrated device used for analog processing quantum information.

The concept stated above demonstrates the nontrivial nature of the polarization phenomenon corresponding to the double dielectric dispersion being manifested in the PAQ spectrum. Studying this electron relaxation polarization is of considerable interest not only in connection with the problem of adapting component types of digital computation engineering to the quantum level. A progress associated with this phenomenon is extremely important for functional microelectronics [11], as its development is able to decisively reactivate analog methods of information processing [12].

REFERENCES

1. R. V. Afanas'eva, T. G. Ermakova, and M. G. Voronkov, Dokl. Akad. Nauk **369**, 329 (1999) [Dokl. Phys. **44**, 749 (1999)].
2. R. V. Afanas'eva, T. G. Ermakova, and M. G. Voronkov, Dokl. Akad. Nauk **374**, 473 (2000) [Dokl. Phys. **45**, 507 (2000)].
3. A. A. Matnishyan, I. L. Arutyunyan, L. S. Grigoryan, and A. A. Ovchinnikov, Dokl. Akad. Nauk SSSR **277**, 1149 (1984).
4. B. A. Rubin, *Biophysics* (Knizhnyi Dom "Universitet," Moscow, 1999), Vol. 1.
5. S. Ya. Kilin, Usp. Fiz. Nauk **169**, 507 (1999).
6. M. B. Mensky, Usp. Fiz. Nauk **168**, 1017 (1998) [Phys. Usp. **41**, 923 (1998)].
7. M. P. Tonkonogov, V. A. Veksler, and E. F. Orlova, Izv. Vyssh. Uchebn. Zaved., Fiz., No. 1, 97 (1982).
8. A. I. Olemskoĭ and A. Ya. Flat, Usp. Fiz. Nauk **163**, 12, 1 (1993) [Phys. Usp. **36**, 1087 (1993)].
9. R. R. Nigmatullin and Ya. E. Ryabov, Izv. Vyssh. Uchebn. Zaved., Fiz., No. 4, 6 (1997).
10. M. F. Shlesinger and J. Klafter, in *Fractals in Physics*, Ed. by L. Pietronero and E. Tosatti (North Holland, Amsterdam, 1986; Mir, Moscow, 1988).
11. Yu. F. Osadchiĭ, O. A. Gludkin, and A. I. Gurov, *Analog and Digital Electronics: Hot Line* (Telekom, Moscow, 1999).
12. Ya. A. Fedotov, V. V. Starostin, and A. A. Shchuka, *Electronics of Fourth Generation* (Znanie, Moscow, 1985).

Translated by T. Galkina

Doklady Physics, Vol. 46, No. 12, 2001, pp. 832–834. Translated from Doklady Akademii Nauk, Vol. 381, No. 4, 2001, pp. 472–474.

PHYSICS

Electrodynamic Properties of a Finely Layered Medium

A. P. Vinogradov and A. M. Merzlikin

Presented by Academician A.M. Dykhne July 31, 2001

Received August 1, 2001

It is well known that when homogenizing Maxwell equations in inhomogeneous media, in the general case, we arrive at nonlocal material equations [1]. However, the majority of theories treating effects of spatial dispersion exhibit a phenomenological nature [2]. In the present study, we make an attempt to rigorously analyze the situation for the simplest case of a one-dimensional medium. Moreover, we restrict our analysis by the consideration of a problem in the long-wave approximation. This implies that the inhomogeneity scale ξ is much smaller than the wavelength $\lambda = \frac{2\pi}{k_0}$ (the subscript 0 at the wave vector k stands for free space). In this case, we may expect only small corrections to static values of effective parameters. We show below that even in this approximation, the homogenization of Maxwell equation for a one-dimensional system is inadmissible.

For a periodic system, the exact solution to the stochastic problem is well known. For example, if the electric field is applied along the layers, then the effective permittivity is equal to the average value for the dielectric constant. If the field is directed in the direction perpendicular to the layers, we should average the reciprocal quantity. For time-dependent fields, the problem of wave propagation in an unbounded periodic medium consisting of layers with permittivity values ε_1 and ε_2 was solved by Rytov [3, 4]. In his studies, the dispersion equation for the refractivity index n^{Ryt}

$$\cos(k_0 n^{\mathrm{Ryt}}(d_1 + d_2)) = \cos(k_0\sqrt{\varepsilon_1}d_1)\cos(k_0\sqrt{\varepsilon_2}d_2) - \frac{\varepsilon_1 + \varepsilon_2}{2\sqrt{\varepsilon_1\varepsilon_2}}\sin(k_0\sqrt{\varepsilon_1}d_1)\sin(k_0\sqrt{\varepsilon_2}d_2) \quad (1)$$

was derived in the framework of the Bloch–Floquet approach. Here, an effective impedance $Z^{\mathrm{Ryt}} = \frac{\langle E\rangle}{\langle H\rangle}$ (averaging occurs over a period) is introduced. This made it possible to deal with the effective permeability μ_{eff} and permittivity $\varepsilon_{\mathrm{eff}}$. In the long-wave approximation, the first-order (with respect to kd) corrections were found [5]. Unfortunately, the results obtained cannot be considered as acceptable from the physical standpoint, since either $\varepsilon^{\mathrm{Ryt}}$ or μ^{Ryt} possess negative imaginary parts depending on the position of the origin.

In order to clarify reasons responsible for this behavior, we consider the problem on the basis of a numerical experiment. We have shown that in an one-dimensional system even in the long-wave approximation, effective parameters, being not self-averaging quantities, do not tend to any limit with increasing the size h.

In the case of the normal incidence of a wave onto a finely layered sample of finite thickness; the actually measurable quantities are the reflection coefficient R and transmission coefficient T, which are linked by the M matrix [5]

$$\begin{pmatrix} T \\ 0 \end{pmatrix} = M\begin{pmatrix} 1 \\ R \end{pmatrix}.$$

The M matrix can be experimentally determined by measuring the coefficients of transmission T and reflection R, while impinging an electromagnetic wave onto the sample from the right and left sides (the relevant subscripts are R and L, respectively):

$$M = \begin{Vmatrix} T - \frac{R_R R_L}{T} & \frac{R_R}{T} \\ -\frac{R_L}{T} & \frac{1}{T} \end{Vmatrix}. \quad (2)$$

Based on $\det M = 1$, we can show that $T_L = T_R = T$, which also follows from the reciprocity theorem.

For the known R and T, we are able to unambiguously determine the effective impedance Z_{eff}, the effective wave number k_{eff}, and the effective admittance Y_{eff} for the sample [6]:

$$Y_{\mathrm{eff}} = \sqrt{\frac{[(1-R)^2 - T^2]}{(1+R)^2 - T^2}},$$

$$\exp(ik_{\mathrm{eff}}L) = \frac{T(1 + 1/Z_{\mathrm{eff}})}{1/Z_{\mathrm{eff}} + R/Z_{\mathrm{eff}} + 1 - R},$$

$$\varepsilon_{\mathrm{eff}} = \frac{Y_{\mathrm{eff}}k_{\mathrm{eff}}}{k_0}, \quad \mu_{\mathrm{eff}} = \frac{k_{\mathrm{eff}}/k_0}{Y_{\mathrm{eff}}}.$$

Other methods of determining the effective parameters do not lead to a qualitative change of the entire pattern.

Institute of Theoretical and Applied Electrodynamics, Joint Institute of High Temperatures, Russian Academy of Sciences, Izhorskaya ul. 17/19, Moscow, 127412 Russia

1028-3358/01/4612-0832$21.00 © 2001 MAIK “Nauka/Interperiodica”

We consider a sample consisting of alternating layers with the equal thickness d, which have the permittivity values ε_1 and ε_2. This sample possesses different symmetry with respect to the normally impinging wave depending on whether the number of layers is even or odd. The sample consisting of odd number of layers has the same layer at both its beginning and end. Therefore, the response of the sample is insensitive to the reversion of the wave-propagation direction. If this composite sample contains an even number of layers, then the first and final layers are different. Therefore, in the case of transparent media the reflection coefficients R_L and R_R can differ in their phase, while in the case of absorption they also differ by their moduli.

The even number of layers. We denote the matrix of the first two layers as m_{12}. Then the M matrix of the sample consisting of $2N$ layers is $M = (m_{12})^N = (m_{12})^{L/(2d)}$. We reduce m_{12} to the Jordan form $m_{12} = SJS^{-1}$ (S and J matrices are independent of L).[1] In this case, $M = (SJS^{-1})^N = SJ^{L/(2d)}S^{-1}$ and J matrix has the form

$$J = \begin{pmatrix} \alpha + i\sqrt{1-\alpha^2} & 0 \\ 0 & \alpha - i\sqrt{1-\alpha^2} \end{pmatrix},$$

where α corresponds to the expression standing in the right-hand side of dispersion equation (1). Finally, we find

$$M = S\begin{pmatrix} \exp(ik_0 n^{\mathrm{Ryt}} L) & 0 \\ 0 & \exp(-ik_0 n^{\mathrm{Ryt}} L) \end{pmatrix} S^{-1}.$$

This representation has a simple physical sense. Analyzing the M matrix of a heterogeneous layer with the thickness L, the refractivity index n, and admittance Y, we can see that this matrix is of the form

$$M = \begin{pmatrix} \frac{1+Y}{2Y} & \frac{Y-1}{2Y} \\ \frac{Y-1}{2Y} & \frac{1+Y}{2Y} \end{pmatrix} \times \begin{pmatrix} \exp(ik_0 nL) & 0 \\ 0 & \exp(-ik_0 nL) \end{pmatrix} \begin{pmatrix} \frac{1+Y}{2Y} & \frac{Y-1}{2Y} \\ \frac{Y-1}{2Y} & \frac{1+Y}{2Y} \end{pmatrix}^{-1};$$

i.e., the J matrix is the propagation matrix, while the S matrix describes the boundary effects. We note that the M matrix of a homogeneous layer has four elements depending on two independent parameters $k_0 L\sqrt{\varepsilon\mu}$ and $\sqrt{\frac{\varepsilon}{\mu}}$. Hence, there must exist two independent equations connecting M-matrix elements. Indeed, $\det(M) = 1$ and $M_{12} = -M_{21}$. The first equation is satisfied by the M matrix of any inhomogeneous sample. As is seen from expression (2), the second equation is satisfied only by composite samples symmetric with respect to the variation in the direction of an impinging wave.

The form of the S matrix of an inhomogeneous sample is rather cumbersome. Therefore it is more convenient in our analysis to consider its expansion in terms of $k_0 d$. Within first-order accuracy, we have in the even case

$$M = M_1 + \begin{pmatrix} 0 & 1 \\ 1 & 0 \end{pmatrix} \frac{(\varepsilon_2 - \varepsilon_1)\sin(k_0 n^{\mathrm{Ryt}} L)}{4\sqrt{(\varepsilon_2 + \varepsilon_1)/2}} k_0 d,$$

where M_1 is the M matrix for a homogeneous layer with the permittivity $\frac{\varepsilon_1 + \varepsilon_2}{2}$. It is worth noting that the correction term proportional to $k_0 d$ is symmetric. This fact makes it impossible to attribute to the M matrix of the even case the form of the M matrix for a homogeneous layer with certain effective parameters. An attempt to allow for effects of spatial dispersion in the first order with respect to $k_0 d$ leads to the fact that the effective parameters begin to depend on the layer thickness. This dependence has periodic nature [6]. The amplitude for the deviation from the average value has an order of $(k_0 d)^2$ and $k_0 d$ for the real and imaginary parts, respectively.

The odd case. The odd case differs from the even one only by the existence of the last layer. With the accuracy to the first order in $k_0 d$, the M matrix for the odd case has the form $M = M_1 + M_2 k_0 d$, where

$$M_2 = \cos(k_0 n^{\mathrm{Ryt}} L)\begin{pmatrix} \frac{i(1+\varepsilon_1)}{2} - \frac{(\varepsilon_2 + 3\varepsilon_1)\tan(k_0 n^{\mathrm{Ryt}} L)}{4\sqrt{(\varepsilon_2 + \varepsilon_1)/2}} & \frac{i}{2}(\varepsilon_1 - 1) \\ -\frac{i(\varepsilon_1 - 1)}{2} & -\frac{i}{2}(1+\varepsilon_1) - \frac{(\varepsilon_2 + 3\varepsilon_1)\tan(k_0 n^{\mathrm{Ryt}} L)}{4\sqrt{(\varepsilon_2 + \varepsilon_1)/2}} \end{pmatrix}.$$

[1] The S matrix is defined ambiguously: there exist infinitely many matrices reducing the given matrix to the Jordan form.

The property of symmetry of the M matrix allows us to determine the effective parameters of the sample, namely,

$$(Y_{\text{eff}}^{\text{DD}})^2 = \frac{\varepsilon_1 + \varepsilon_2}{2} + \frac{(\varepsilon_1 - \varepsilon_2)}{2}\sqrt{\frac{\varepsilon_1 + \varepsilon_2}{2}}\cot(k_0 n^{\text{Ryt}} L)k_0 d,$$

$$\cos(k_0 n_{\text{eff}}^{\text{ODD}} L) = \cos(k_0 n^{\text{Ryt}} L) - \frac{(\varepsilon_2 + 3\varepsilon_1)\sin(k_0 n^{\text{Ryt}} L)}{4\sqrt{(\varepsilon_2 + \varepsilon_1)/2}}k_0 d.$$

However, these parameters depend on the sample thickness. This dependence manifests itself most clearly near the frequency of the perfect transmission $k_0 n^{\text{Ryt}} L = \pi l$, $l = 0, 1, 2, \ldots$, where the effective parameters can attain arbitrarily high values. This statement is confirmed by numerical experiments, Fig. 1 [6]. Fluctuations of peak amplitudes are associated with the discreteness of the thickness values and with the incommensurability of the period and the effective wavelength.

In conclusion, we would like to note that, as $k_0 d \longrightarrow 0$, the M matrix nonuniform tends to the M matrix of a homogeneous layer with the thickness L and the effective parameters $\varepsilon_{\text{eff}} = \dfrac{\varepsilon_1 + \varepsilon_2}{2}$ and $\mu_{\text{eff}} = 1$. The nonuniform nature of this tendency of the M matrix is associated with the appearance of the term $n^{\text{Ryt}}(k_0 d)L$ in the J matrix. Thus, for an arbitrary infinitesimal $k_0 d$, there exist L beginning from which the inequality $n^{\text{Ryt}}(k_0 d)L - n^{\text{Ryt}}(0)L > \pi$ is valid. In other words, in order to pass to the static case, it is first necessary for the frequency $k_0 d$ to approach zero and only afterwards to increase the size of the system under consideration. Apparently, this behavior is associated with the fact that a certain scale much exceeding the wavelength is inherent in the problem, namely, the transverse size of the system (cf. the solution to the problem of diffraction on an infinite wire [7]).

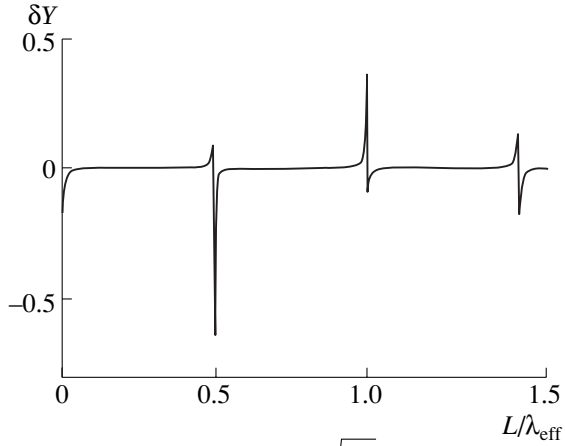

Dependence of the quantity $\delta Y = \sqrt{\dfrac{\varepsilon_{\text{eff}}}{\mu_{\text{eff}}}} - Y^{\text{Ryt}}$ on the sample thickness L for the odd number of layers. The sample thickness is normalized to the effective wavelength $\lambda_{\text{eff}} = \lim\limits_{L \to \infty}\left(\dfrac{2\pi}{k_{\text{eff}}}\right)$; $\varepsilon_1 = 2$, $\varepsilon_2 = 3$, and $k_0 d = 0.01$.

The absence of a finite-frequency limit as $L \longrightarrow \infty$ has its analog in quantum mechanics. Actually, the problem of the above-barrier scattering of a particle on a steplike potential is not the ultimate case of scattering on a Π-like potential in the case when the width of this potential tends to infinity.

We also note that in spite of the apparent plateau of $Y_{\text{eff}}(L)$ for $L < \lambda/2$, the deviations in the phase of the exact solution from that corresponding to a homogeneous medium with Rytov's parameters has an order of $k_0 d$. This follows from the results of the numerical simulation [6] yielding $Y_{\text{eff}}(L) - Y^{\text{Ryt}} \sim d/L$.

Summarizing the above results, we can say that introducing the effective values of the dielectric and magnetic permittivity for the description of one-dimensional media is possible only in the quasistatic limit $d \ll L \ll \lambda$. It is this particular case when static mixing formulas are true: e.g., for the normal incidence, $\varepsilon_{\text{eff}} = \langle\varepsilon\rangle$ and $\mu_{\text{eff}} = \langle\mu\rangle$. An attempt to allow for corrections associated with the radiation retardation on the length of the inhomogeneity scale leads to the absence of intrinsic material parameters. The effective parameters obtained depend on the sample thickness L, thereby describing not the material but the sample. In this case, the deviation of the sample effective parameters from the values obtained by Rytov [3, 4] for $L = \infty$ can reach hundreds of percent even for a small value of $k_0 d$.

ACKNOWLEDGMENTS

The authors are grateful to A.N. Lagar'kov and S.A. Rybak for fruitful discussions.

This work was supported in part by the Russian Foundation for Basic Research, project nos. 00-15-96570 and 01-02-17962.

REFERENCES

1. E. Sanchez-Palencia, *Nonhomogeneous Media and Vibration Theory* (Springer-Verlag, Berlin, 1980; Mir, Moscow, 1984).
2. V. M. Agranovich and V. L. Ginzburg, *Crystal Optics with Spatial Dispersion and Excitons* (Nauka, Moscow, 1979; Springer-Verlag, New York, 1984).
3. S. M. Rytov, Zh. Éksp. Teor. Fiz. **29**, 605 (1955) [Sov. Phys. JETP **2**, 466 (1956)].
4. S. M. Rytov, Akust. Zh. **2**, 71 (1956) [Sov. Phys. Acoust. **2**, 68 (1956)].
5. L. M. Brekhovskikh, *Waves in Layered Media* (Akad. Nauk SSSR, Moscow, 1957; Academic, New York, 1960).
6. A. P. Vinogradov and A. M. Merzlikin, in *Proceedings of PIERS'01, Osaka, July 18–22, 2001*.
7. R. B. Vaganov and B. Z. Katsenelenbaum, *Foundations of Diffraction Theory* (Nauka, Moscow, 1982).

Translated by G. Merzon

Doklady Physics, Vol. 46, No. 12, 2001, pp. 835–838. Translated from Doklady Akademii Nauk, Vol. 381, No. 6, 2001, pp. 756–759.

PHYSICS

Size and Temperature Effect on Polymorphic Transformations in Alkali Halide Crystals

D. L. Vinokurskiĭ*, S. V. Karpenko*, A. Kh. Kyarov, and A. I. Temrokov***

Presented by Academician V.E. Fortov February 19, 2001

Received May 10, 2001

Considerable recent advances have been made in the theory of the structural phase transitions under high-pressure conditions. However, most of the theoretical papers deal with the calculation of parameters characterizing polymorphic transformations in crystals of infinitely large size at zero temperature. In the present paper, we study the features of structural phase transitions under high pressures in ionic crystals of the M^+X^- type using the density-functional technique [1]. The case of finite-size crystals is considered. A special emphasis is made on the calculation of the characteristic pressure of the B1 ⟶ B2 phase transition (transition from the NaCl-type structure to the CsCl-type structure) as a function of temperature.

Polymorphic transformations are first-order phase transitions giving rise to structural changes in solid crystals. The phase with the NaCl-type structure (B1) is stable at zero external pressure. At a certain pressure p_0, the Gibbs free energies G_1 and G_2 of dielectric phases with the NaCl- and CsCl-type structures become equal and the B1 ⟶ B2 structural phase transition takes place. With a further increase in pressure, the CsCl-type phase (B2) becomes stable. At even higher pressures, the insulator–metal transition can be observed [2, 3]. The Gibbs free energy of the crystal under hydrostatic compression at zero temperature can be represented in the form [4] (subscript i numbers two phases, B1 and B2)

$$G_{\mathrm{Bi}} = U_{\mathrm{Bi}}(R_{\mathrm{i}}) - \frac{\alpha_{\mu i}}{R_i} + pV_i + 4\pi r^2 k\sigma_i, \qquad (1)$$

where $\alpha_{\mu i}$ is the Madelung constant of the corresponding structural modification, R_i is the equilibrium interionic distance, V_i is the unit cell volume, U_i is the interionic pair potential [5], σ_i is the specific surface free energy (below referred to as the surface energy), r is the radius of a crystal grain, and k is the factor taking into account the deviation of the crystal from the spherical shape ($k = 1$ in the case of an ideal spherical crystal). It follows from relationship (1) that the accuracy characterizing calculations of the Gibbs free energy and hence the pressure corresponding to the polymorphic transformation depends on the adequacy of the interionic pair interaction potential $U(R)$ applied. In the present paper, we use pair potentials determined in a self-consistent manner and based on the theory of inhomogeneous electron gas [5].

In our calculations, we took into account the interactions of ions within seven coordination spheres. Thus, the values of $U_{\mathrm{Bi}}(R_i)$ can be represented as

$$U^{(i)}(R) = \sum_{k=1}^{7} N_k^{(i)} U_k^{(i)}(a_k^{(i)} R^{(i)}), \qquad (2)$$

where $a_k = \dfrac{R_k}{R_1}$ is the ratio of radii of the kth and first coordination spheres and $N^{(i)}$ is the number of ions per unit cell. With due regard to $p = -\dfrac{\partial U^{(i)}}{\partial V^{(i)}}$, we can rewrite relationship (1) using (2):

$$G_{\mathrm{B1}} = \sum_{k=1}^{7} N_k^{(i)} U_k^{(i)}(a_k^{(i)} R^{(i)}) - V^{(i)} \frac{\partial}{\partial V^{(i)}} \left[\sum_{k=1}^{7} N_k^{(i)} U_k^{(i)}(a_k^{(i)} R^{(i)}) \right] - \frac{\alpha_\mu^{(i)}}{R^{(i)}} + 4\pi r^2 k\sigma^{(i)}. \qquad (3)$$

To calculate the surface energy $\sigma^{(i)}$ of polymorphic modifications, we used the Gibbs definition of the surface energy [6]

$$\sigma(hkl) = \sum_i \sum_{j=0}^{\infty} (W_j^{(i)} - W_\infty^{(i)}) n_j(hkl), \qquad (4)$$

where $\sigma(hkl)$ is the surface energy of crystal face (hkl), $W_j^{(i)}$ is the energy per particle (ion) in the jth crystal

* *Institute of Applied Mathematics and Automation, Kabardino-Balkar Scientific Center, Russian Academy of Sciences, ul. Shortanova 89a, Nalchik, 360000 Russia*

** *Kabardino-Balkar State University, ul. Chernyshevskogo 173, Nalchik, 360004 Russia*

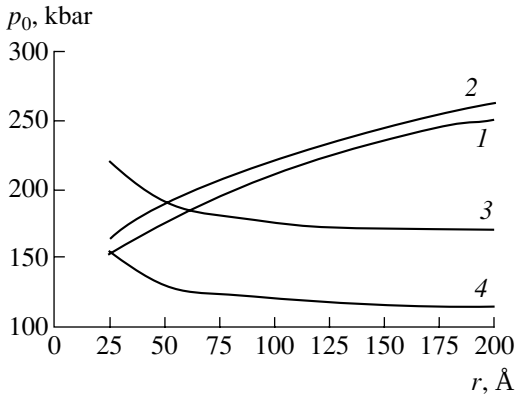

Fig. 1. Pressure corresponding to the B1–B2 phase transition in lithium halide salts as a function of the crystal size: (*1*) LiF ($k = 1$); (*2*) LiF ($k = 2$); (*3*) LiCl, (*4*) LiBr.

layer corresponding to the *i*th type of interionic interaction forces, $W_\infty^{(i)}$ is the similar quantity in the crystal bulk, and $n_j(hkl)$ is the number of particles per unit area at the crystal face (*hkl*) in the *j*th plane.

A simple calculation method for the surface energy was developed in the studies of Zadumkin and Temrokov [7]. The method suggests to divide the crystal into a mesh of planar elements and to perform summation over a set of such meshes. This particular approach is employed below to calculate the surface energy of the ionic compounds under study.

In the zeroth approximation used here, expression (4) takes the form

$$\sigma(hkl) = n_0(hkl)\sum_i (W_0^{(i)} - W_\infty^{(i)}). \quad (5)$$

The relationship obtained can be easily brought to the following form:

$$\sigma(hkl) = n_0(hkl)\sum_i (\beta_i - 1)W_\infty^{(i)}, \quad (6)$$

where we introduced the notation $\beta_i = \dfrac{W_S^{(i)}}{W_\infty^{(i)}} = \dfrac{A_S^{(i)}}{A_V^{(i)}}$ for the ratio of sums over both the infinite planar mesh and the infinite lattice for the *i*th type of the interionic interaction forces.

Thus, the final expression for the Gibbs free energy of the crystal can be written as

$$G_{\mathrm{Bi}} = \sum_{k=1}^{7} N_k^{(i)} U_k^{(i)}(a_k^{(i)} R^{(i)})$$

$$- V^{(i)}\frac{\partial}{\partial V^{(i)}}\left[\sum_{k=1}^{7} N_k^{(i)} U_k^{(i)}(a_k^{(i)} R^{(i)})\right] - \frac{\alpha_\mu^{(i)}}{R^{(i)}} \quad (7)$$

$$+ 2\pi r^2 k n_0(hkl)\sum_i (\beta^{(i)} - 1)W_\infty^{(i)}.$$

Note that we assumed (for simplicity of the model) that the crystal has (100) faceting in its B1 modification and (110) faceting in the B2 modification, since these faces correspond to the minimum surface energy at $T = 0$ K and $p = 0$. Minimizing the Gibbs free energy and calculating the interionic distance at the given pressure, we can determine the difference $\Delta G = G_{\mathrm{B2}} - G_{\mathrm{B1}}$. If p_0 is the pressure of polymorphic transformation, then the condition determining the phase transition is

$$G_1(p_0) = G_2(p_0). \quad (8)$$

In the course of finding a numerical solution to equation (8), the phase-transition point was determined with a specified accuracy as

$$|G_1(p_0) - G_2(p_0)| < \varepsilon,$$

where ε is the given calculation error. The value of ε was chosen in such a way that the pressure corresponding to the transition can be found with an accuracy to 0.5 kbar. Using this technique, we calculated the pressure values for the B1 to B2 transition for alkali halide crystals with sizes ranging from 25 to 200 Å. The calculated dependence of the pressure corresponding to the polymorphic transformation on the crystal size is shown in Fig. 1 for lithium halide salts. The analysis of the data obtained demonstrates that the pressure corresponding to the polymorphic transformation increases with the decrease in the crystal size for the alkali halide crystals under study, except for LiF. Note also that, for a nonspherical crystal grain ($k = 2$), the transition pressure turns out to be on the average by 8–10% higher than that for an ideal spherical crystal ($k = 1$). Lithium fluoride crystals exhibit a special type of behavior: the pressure corresponding to the B1–B2 transition decreases with the crystal size. The anomalous behavior of this crystal stems from the fact that the surface energy for the phase with the CsCl-type structure (B2) is lower than that for the phase with the NaCl-type structure (B1). Therefore, the surface contribution to the Gibbs free energy promotes the phase transition, reducing the pressure value corresponding to the transition. For all other alkali halide crystals, this size effect leads to an increase in the pressure corresponding to the polymorphic transformation with the decrease in the crystal size.

We now turn to the discussion of the polymorphic B1–B2 transformations at nonzero temperatures, restricting our analysis to the case of an infinite crystal. The electron contribution to the lattice energy given by the first term in (7) is almost temperature-independent, since the electron gas is degenerate in the temperature range under study $T < T_{\mathrm{melt}}$. To take into account the temperature dependence of the phonon contribution to the energy, we suggest using the third term in (7), i.e., by substitution of the Madelung constant of the struc-

ture for a certain effective parameter, namely, by the temperature factor of the Coulomb interaction K_T, which is a function of temperature. Note that we have $K_T \longrightarrow \alpha_\mu$ as $T \longrightarrow 0$ K. In this case, relationship (7) can be rewritten in the following form:

$$G_{\mathrm{Bi}} = \sum_{k=1}^{7} N_k^{(i)} U_k^{(i)} (a_k^{(i)} R^{(i)})$$

$$- V^{(i)} \frac{\partial}{\partial V^{(i)}} \left[\sum_{k=1}^{7} N_k^{(i)} U_k^{(i)} (a_k^{(i)} R^{(i)}) \right] - \frac{K_T^{(i)}}{R^{(i)}} \qquad (9)$$

$$+ 2\pi r^2 k n_0 (hkl) \sum_i (\beta^{(i)} - 1) W_\infty^{(i)}.$$

To calculate the values of the $K_T(T)$ parameter as a function of temperature, we used the method of molecular dynamics. The values of K_T can be found using the expression [8]

$$K_T = R_0 \sum_{j \neq 1} (\pm) \frac{1}{r_{ij}}, \qquad (10)$$

where R_0 is the equilibrium interionic distance and r_{ij} is the set of coordinates of the chosen number of particles in the system (we modeled a system of $N = 10^4$ particles with charges $|q| = 1$). The number of particles in the system was assumed to be constant, and their total momentum was taken to be zero. The equations of motion for particles are the equations corresponding to Newton law:

$$\frac{d^2 r_i(t)}{dt^2} = \frac{\sum_{i<j} F_i(r_{ij})}{m}. \qquad (11)$$

Numerically solving equations (11), we used the discretization of the second-order differential operator in the left-hand side of (11). This discretization gives rise to the following explicit difference equation for central differences:

$$\frac{d^2 r_i(t)}{dt^2} = \tau^{-2} [r_i(t+\tau) - 2r_i(t) + r_i(t-\tau)] = \frac{F_i(t)}{m}. \qquad (12)$$

The initial positions of particles are specified at the sites of the corresponding crystal lattice, and equations (12) are solved using the velocity Verlet algorithm [9]. The manifold of ionic coordinates defined in such a way is used in computations of the Coulomb interaction parameter at a given temperature T; this computation is then repeated for the next temperature value $T + \Delta T$, etc., up to the temperature value on the order of T_{melt}. In Fig. 2, we show the $K_T(T)$ plots for NaCl- and CsCl-type structures.

Based on the calculated $K_T(T)$ functions for both structures (B1 and B2), we performed calculations of

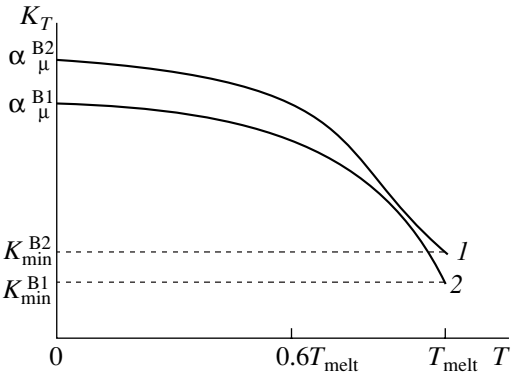

Fig. 2. Temperature dependence of the Coulomb interaction parameter: (*1*) B1 structure, $\alpha_\mu^{B1} = 1.747558$, $K_{\min}^{B1} = 1.432998$; (*2*) B2 structure, $\alpha_\mu^{B2} = 1.762670$, $K_{\min}^{B2} = 1.551149$.

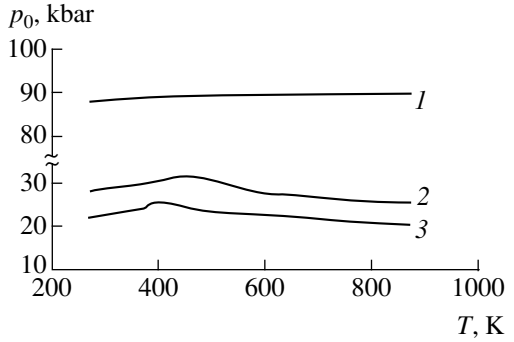

Fig. 3. Temperature dependence of the pressure corresponding to the polymorphic transformation for potassium halide compounds: (*1*) KF; (*2*) KCl; (*3*) KBr.

the pressure values corresponding to the polymorphic transformation as a function of temperature. In Fig. 3, we present the temperature dependence of the B1–B2 transition pressure for potassium halide salts. In agreement with experiment [10], the calculated values of the transition pressure have only a slight linear dependence on temperature. For lithium, sodium, and rubidium compounds (except RbBr), as well as for potassium fluoride, the pressure corresponding to the polymorphic transformation slowly increases $\left(\frac{\Delta p}{\Delta T} > 0\right)$, whereas for KCl, KBR, and RbBr crystals, we have $\frac{\Delta p}{\Delta T} < 0$. Note that for KCl, KBr, and RbBr crystals, the $p_0(T)$ curve exhibits a peak at a certain temperature T_{cr}: $T_{\mathrm{cr}}(\mathrm{KCl}) = 491$ K, $T_{\mathrm{cr}}(\mathrm{KBr}) = 387$ K, and $T_{\mathrm{cr}}(\mathrm{RbBr}) = 393$ K. In other words, the phase transition corresponds to the zero entropy jump at $T = T_{\mathrm{cr}}$, $\Delta S(T_{\mathrm{cr}}) = 0$. The experimental data [10] for KBr demonstrate that the measured $p_0(T)$ curve can exhibit a peak at $T \approx 150$–370 K. Thus, we come to the conclusion that there exists an isotherm such that the sign of the latent heat of the

B1–B2 structural transformation is changed when this isotherm is crossed.

REFERENCES

1. V. F. Ukhov, R. M. Kobeleva, G. V. Dedkov, and A. I. Temrokov, *Electron and Statistical Theory of Metals and Ionic Crystals* (Nauka, Moscow, 1982).
2. J. L. Feldman, B. M. Klein, and M. J. Mehl, Phys. Rev. B **42**, 2752 (1990).
3. A. I. Temrokov, *Surface Energy and Surface Tension of Solids*, Doctoral Dissertation in Physics and Mathematics (Nalchik, 1982).
4. S. V. Karpenko, A. Kh. Kyarov, and A. I. Temrokov, Teplofiz. Vys. Temp. **38**, 748 (2000).
5. A. Kh. Kyarov and A. I. Temrokov, Izv. Vyssh. Uchebn. Zaved., Fiz., No. 6, 3 (1994).
6. J. W. Gibbs, in *The Collected Works of J. Willard Gibbs* (Yale Univ. Press, New Haven, 1948; Gostekhteorizdat, Moscow, 1950), Vols. 1, 2.
7. S. N. Zadumkin and A. I. Temrokov, Izv. Vyssh. Uchebn. Zaved., Fiz., No. 9, 40 (1968).
8. V. M. Danilenko, *Models of Actual Crystals* (Naukova Dumka, Kiev, 1983).
9. D. W. Heermann, *Computer Simulation Methods in Theoretical Physics* (Springer-Verlag, Berlin, 1986; Nauka, Moscow, 1990).
10. A. J. Darnell and W. A. McCollum, J. Phys. Chem. Solids **31**, 805 (1970).

Translated by K. Kugel

Doklady Physics, Vol. 46, No. 12, 2001, pp. 839–841. Translated from Doklady Akademii Nauk, Vol. 381, No. 6, 2001, pp. 760–762.

PHYSICS

Structure of the Steady-State Detonation Wave in Pressed RDX

A. V. Utkin, S. A. Kolesnikov, and Academician V. E. Fortov

Received June 5, 2001

According to the classical theory [1], the detonation decomposition of an explosive is caused by the effect of a shock wave that initiates an exothermic chemical reaction. Therefore, a steady-state detonation wave consists of both a shock wave and an accompanied chemical-transformation zone. In this pressure-drop zone, the substance expands; i.e., a von Neumann spike forms. The reaction zone ends up with the Chapman–Jouguet plane in which the particle velocity with respect to the wave front is equal to the local sound velocity. Inside the zone, the flow is subsonic, which provides an energy intake to the shock-wave front. Such a characteristic of the flow allows rigorous substantiation of a selection rule for the velocity of the steady-state detonation. Many experimental studies have confirmed the validity of this model for heterogeneous explosives. However, there is recent sufficiently convincing evidence that, in certain explosives (RDX [2], HMX [2], TNETB [3, 4], ZOX [3]), the von Neumann spike does not arise at a high initial density. The final state forms as a result of the pressure growth, which contradicts classical concepts. Moreover, it is unclear whether the Chapman–Jouguet regime is realized in this case and by what means the detonation velocity is controlled. To answer these key questions of the theory, we should experimentally investigate all details of the transition from the detonation regime marked by the von Neumann spike to a flow with monotonically growing parameters in the reaction zone. In this study, we have carried out such investigations for RDX and have determined, in particular, for which initial density ρ_0 this effect does occur and how the von Neumann spike disappears.

Samples of different initial density were prepared using RDX powder with an average particle size of ~80 μm. Figure 1 presents the detailed particle-size distribution. A small amount of acetone (less than 1% by mass) was added to the powder being pressed to obtain a density ρ_0 ranging from 1.50 to 1.74 g/cm^3 (RDX_1). A higher density (up to 1.776 g/cm^3) was attained by increasing the mass fraction of acetone up to 10% and holding the samples under pressure (RDX_2).

A scheme of the experimental setup is shown in Fig. 1. In the explosives under investigation, detonation was initiated by a shock wave with an amplitude exceeding 4 GPa, which was generated by a plane-wave generator (*1*). The formation of steady-state detonation regimes was provided by charges 30 mm in diameter with lengths varying from 40 to 80 mm. Wave profiles were recorded by a VISAR laser interferometer having a time resolution of about 3 ns and a velocity-measurement accuracy to ±5 m/s. The probing radiation was reflected from aluminum foil (*2*) with a thickness of 200 to 400 μm, which was located between the charge end face and a water window (*3*). Experimental data yield the velocity of the foil surface adjoining water and show the detailed structure of the reaction zone in the detonation wave.

Figure 2 shows the experimental data for RDX_1. For densities lower than 1.72 g/cm^3, the pattern recorded is typical of heterogeneous explosives. After the shock front, we observe a velocity drop at the foil–water interface. The duration and amplitude of this drop are deter-

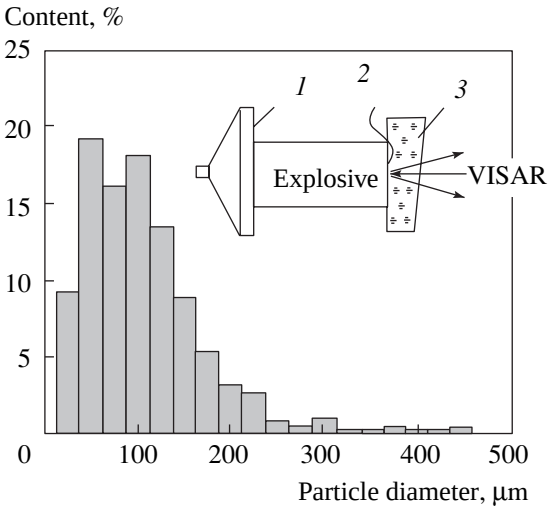

Fig. 1. Particle-size distribution in the parent RDX powder. The insert shows a sketch of the experimental setup: (*1*) plane-wave generator, (*2*) aluminum foil, and (*3*) water window.

Institute of Problems of Chemical Physics, Russian Academy of Sciences, Chernogolovka, Moscow oblast, 142432 Russia

1028-3358/01/4612-0839$21.00

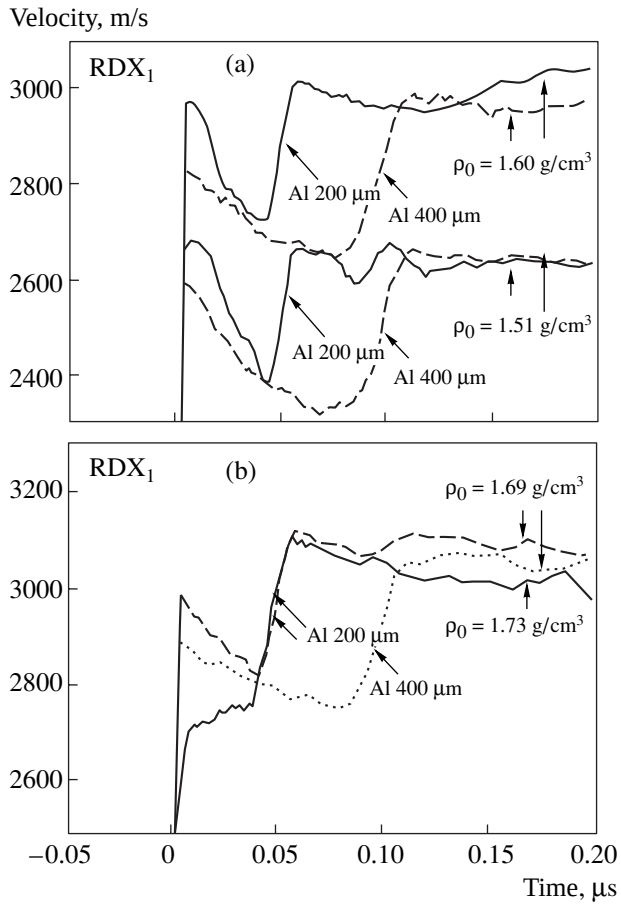

Fig. 2. Velocity of motion of aluminum foils separating an explosive from the water window in the experiments with RDX_1 of a different density ρ_0.

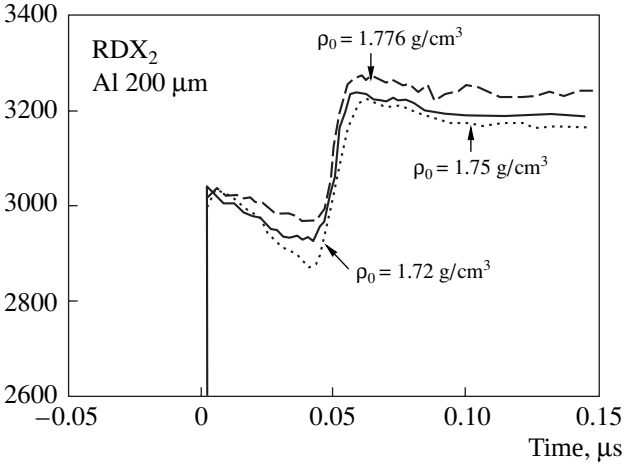

Fig. 3. Velocity of motion of aluminum foils separating an explosive from the water window in the experiments with RDX_2 of a different density ρ_0.

mined by parameters of the von Neumann spike in RDX. The subsequent increase in the velocity is caused by circulation of both compression and rarefaction waves in the foil. We can see that as the shock wave propagates, the velocity peak decays. An increase in the foil thickness from 200 to 400 μm results in a decrease in the velocity-peak amplitude by approximately 100–200 m/s. Therefore, the exact determination of the von Neumann spike amplitude requires thinner foils to be used in the experiments and subsequent extrapolation of the results obtained to zero foil thickness. However, this was not the purpose of our work, since we were interested in studying the qualitative evolution of the von Neumann spike due to the increase of the initial density, because this information is not lost even in relatively thick foils.

For densities of 1.51 and 1.60 g/cm^3, the descending part of the velocity profile has a kink at ~30 ns, while the total peak duration is about 70 ns (Fig. 2a). Therefore, we can speak of the existence of two stages of the RDX decomposition in the detonation wave. Previously, a similar mode was observed in trotyl [5]. According to the authors of [5], the first high-rate stage is associated with the appearance of gaseous reaction products, while the second stage, whose characteristic time reaches about 200 μs, is caused by the formation of the condensed carbon phase. A similar characteristic of the chemical reaction in RDX probably leads to the origination of the kinks in the velocity profiles.

An increase in the initial density causes minor variations in the duration of the velocity peak and, on the other hand, a noticeable decrease in its amplitude, from approximately 400 m/s at 1.51 g/cm^3 to 200 m/s at 1.69 g/cm^3. When ρ_0 exceeds 1.72 g/cm^3, the von Neumann spike disappears and the situation changes radically. After the jump, instead of a velocity drop, a monotonic velocity increase is observed. The velocity profile corresponding to ρ_0 = 1.73 g/cm^3 is shown in Fig. 2b. It is noteworthy that the particle velocity of explosion products in the final state (in the presence of the von Neumann spike, this is the Chapman–Jouguet point) grows with increasing initial density. The only exception is a certain vicinity of the critical density for which the velocity variation becomes anomalous. For ρ_0 = 1.73 g/cm^3, the particle velocity is equal to that for 1.69 g/cm^3 (Fig. 2b). At the same time, according to the experiments performed, the density variation by 0.04 g/cm^3 must increase the velocity by approximately 50 m/s. This fact can be explained only by the passage to the undercompression detonation mode at the moment of the disappearance of the von Neumann spike.

Experimental results for RDX_2 are shown in Fig. 3. They differ in principle from the expected RDX_1 data extrapolated to the higher density range. The von Neumann spike is distinctly recorded throughout the entire investigated range of initial densities. With increasing ρ_0 from 1.72 to 1.776 g/cm^3, the spike amplitude drops approximately twice. Thus, by analogy with RDX_1, the critical initial density characterized by the disappearance of the von Neumann spike is expected to exist and

to be close to 1.78 g/cm^3 in RDX_2. This conclusion agrees with the data presented in [2]. We also note that at a density of 1.72 g/cm^3 the final velocity (Fig. 3) turns out to be higher than for RDX_1 of the density 1.73 g/cm^3 (Fig. 2b) at which the von Neumann spike disappears. This fact confirms again that the undercompression detonation possibly exists in the vicinity of the critical density.

According to the results obtained, the character of the parameter variation in the reaction zone of the steady-state detonation wave essentially depends on the internal structure of the samples under investigation. In turn, this structure is determined not only by the initial dispersivity of the RDX powder but by the method of its production. As is well known [6], during the compaction of an explosive, its particles are destroyed and, as a consequence, their size distribution changes. Studies of HMX [6] have shown that pressing not only changes the relative size distribution of the particles but also abruptly decreases their average size. Naturally, pressing conditions affect the character of the particle destruction. Pressing with a small amount of acetone forms many potential reaction centers. This leads to a higher decomposition rate of the explosive so that the majority of it reacts in the shock-wave front. As a result, a detonation wave arising at $\rho_0 > 1.72$ g/cm^3 has no von Neumann spike. Pressing with a large amount of acetone allows the same density to be obtained in RDX consisting of fewer damaged particles. As a result, the reaction rate decreases and the von Neumann spike forms.

As was noted above, the classical model fails to describe a steady-state detonation wave without the von Neumann spike, which propagates in the undercompression mode. Nevertheless, the authors of [7, 8] emphasize the possibility for a considerable part of explosive to react immediately in the shock-wave front so that only explosive afterburning occurs in experimentally observed von Neumann spikes. Analyzing the effect of the shock-wave front width on the reaction-zone structure, the author of [8] devotes much attention to the fact that the state formed immediately behind the shock-front corresponds to the nonequilibrium shock Hugoniot for the explosive. Then this state relaxes to the equilibrium shock Hugoniot, and the chemical reaction occurs.

The possibility of propagating a steady-state detonation wave having no von Neumann spike is analyzed in [9, 10]. A mathematical model of the phenomenon is considered with allowance for the width of the shock-wave front, which is determined by the viscosity. In the case of low viscosity, a steady-state detonation mode qualitatively similar to the classical one is formed. The only difference corresponds to a smaller amplitude of the von Neumann spike and to the fact that a certain fraction of the explosive turns out to be reacted in the compression-wave front. However, an increase in the reaction rate qualitatively changes the structure of the detonation front; i.e., the final state described by the detonation Hugoniot is attained as a result of monotonic pressure growth. In this case, the detonation can occur in the undercompression mode, and the detonation rate is determined both by the kinetics of the chemical reaction and the compression-wave structure, rather than only by thermodynamics and gas dynamics, which is predicted by the classical detonation theory.

ACKNOWLEDGMENTS

This work was supported by the Russian Foundation for Basic Research, project no. 00–03–32308a.

REFERENCES

1. Ya. B. Zel'dovich, *Theory of Shock Waves and Introduction to Gas Dynamics* (Akad. Nauk SSSR, Moscow, 1946).
2. V. K. Ashaev, G. S. Doronin, and A. D. Levin, Fiz. Goreniya Vzryva, No. 1, 95 (1988).
3. A. V. Utkin, in *Proceedings of the XII Symposium on Combustion and Explosion* (IPKhF RAN, Chernogolovka, 2000), Part 2, p. 168.
4. A. V. Utkin, S. V. Pershin, and V. E. Fortov, Dokl. Akad. Nauk **374**, 486 (2000).
5. C. M. Tarver, R. D. Breithaupt, and J. W. Kury, J. Appl. Phys. **81**, 7193 (1997).
6. N. J. Burnside, S. F. Son, B. W. Asay, and C. B. Skidmore, in *Proceedings of the Conference on Shock Compression of Condensed Matter, 1997* (American Inst. of Physics, Woodbury, 1998), p. 571.
7. V. S. Trofimov, in *Detonation: Critical Phenomena. Physicochemical Conversions in Shock Waves* (OIKhF RAN, Chernogolovka, 1978), pp. 11–15.
8. A. N. Dremin, Fiz. Goreniya Vzryva **36** (6), 31 (2000).
9. F. A. Williams, *Combustion Theory* (Addison-Wesley, Reading, 1964; Nauka, Moscow, 1971).
10. W. Fickett, *Introduction to Detonation Theory* (Univ. of California Press, Berkeley, 1985; Mir, Moscow, 1989).

Translated by Yu. Verevochkin

Doklady Physics, Vol. 46, No. 12, 2001, pp. 842–848. Translated from Doklady Akademii Nauk, Vol. 381, No. 6, 2001, pp. 763–769.

PHYSICS

Post-Induction Processes in the Case of Thermal Explosion in Porous-Medium–Gaseous-Reagent–Solid-Product Systems

K. G. Shkadinskiĭ*, N. I. Ozerkovskaya, and Academician A. G. Merzhanov****

Received June 9, 2001

In the theory of thermal explosion (see e.g., [1]), basic attention is attracted to processes occurring in homogeneous and quasi-homogeneous systems. In these systems, the rate of exothermic chemical transformation is mainly governed by temperature effects, while critical phenomena are determined by a relationship between the heat-release rate and the rate of heat removal to the environment. For a long time, post-induction processes were outside the scope of analysis, since the simple thermal-kinetic models used in theory were inapplicable. However, widespread studies of self-propagating high-temperature synthesis [2, 3] and applications of thermal explosion as a promising technological method for performing synthesis [4] have excited interest in the investigation of post-induction processes [5]. In the course of the high-temperature synthesis of nitrides, oxides, hydrides, and other metal–gas compounds, we deal with a typical situation. In the course of these processes, a gaseous reagent consisting of identical molecules is absorbed in the process of interaction with a solid porous reagent to form a solid product. At moderate pressures, the amount of the intraporous gas in the solid porous reagent is smaller than that required for stoichiometry. Therefore, the filtration transport from the outside is extremely important, since diffusion is absent. An effect of filtration on the critical conditions governing the thermal explosion (induction period) is analyzed in [6].

In the present study, we have found a complete solution to the unsteady filtration problem of thermal explosion, which includes the post-induction period during which synthesis takes place. For simplicity, in the mathematical model proposed, all defining features of the process are preserved. We consider the reaction: porous medium + gas $\longrightarrow$ solid product. The macrokinetic law of exothermic interaction is assumed to be exponentially dependent on temperature and is weakly sensitive to pressure [7].

* *Institute of Chemical-Physics Problems, Russian Academy of Sciences, Chernogolovka, Moscow oblast, 142432 Russia*

** *Institute of Structural Macrokinetics and Problems of Materials Technology, Russian Academy of Sciences, Chernogolovka, Moscow oblast, 142432 Russia*

THE MATHEMATICAL MODEL

We consider a set of equations written out in the dimensionless form.

The heat-balance equation:

$$\tilde{c}\tilde{\rho}\frac{\partial\theta}{\partial\tau} + c\rho(1-m)V\frac{\partial\theta}{\partial\xi} = \frac{1}{\mathrm{Fk}}\frac{\partial}{\partial\xi}\left(\lambda(m,\eta)\frac{\partial\theta}{\partial\xi}\right) + \frac{1}{\mathrm{Td}}m_0\frac{\partial\eta}{\partial\tau}; \quad (1)$$

the mass-balance equation for the intraporous gas:

$$\frac{\partial}{\partial\tau}[\rho(1-m)] = \frac{1}{\mathrm{Fk}_f}\frac{\partial}{\partial\xi}\left[\rho(1-m)k_f(m,\eta)\frac{\partial P}{\partial\xi}\right] - \nu m_0\frac{\partial\eta}{\partial\tau}; \quad (2)$$

and the macrokinetics-transformation equation:

$$\frac{\partial\eta}{\partial\tau} = \mathrm{Td}\exp\left(\frac{\theta}{1+\mathrm{Ar}\theta}\right)\varphi(\eta, P). \quad (3)$$

The gas density and the velocity of the gas motion are determined according to the pressure from the equation of gas state

$$P = \rho(1+\mathrm{Ar}\theta), \quad (4)$$

and from the Darcy equation

$$V = -\frac{k_f(m,\eta)}{\mathrm{Fk}_f}\frac{\partial P}{\partial\xi}, \quad (5)$$

respectively. The boundary and initial conditions are:

$$\xi = 0: \frac{\partial\theta}{\partial\xi} = 0, \quad V = 0;$$
$$\xi = 1: \lambda(m,\eta)\frac{\partial\theta}{\partial\xi} = -\mathrm{Bi}\theta, \quad P = P_0; \quad (6)$$

$$\tau = 0: \theta = -\mathrm{Ze}; \quad V = 0; \quad P = P_0; \quad \eta = 0. \quad (7)$$

1028-3358/01/4612-0842$21.00 © 2001 MAIK “Nauka/Interperiodica”

Here, $m = m_0(1 - \eta) + m_0(1 + \nu)\frac{\eta}{\rho_p}$ is the volume fraction of the condensed matter; $\tilde{c}\tilde{\rho} = c\rho(1 - m_0) + m_0(1 - \eta) + c_p\rho_p(1 + \nu)m_0\eta$ is the heat capacity per unit volume; $\tilde{\lambda}(m, \eta) = \lambda_k m + \lambda_g(1 - m)$ is the effective heat conductivity (λ_k and λ_g are the heat conductivities for the original substance and the gas, respectively); $k_f(m, \eta) = (1 - m(\eta))^{5/3}$ is the filtration factor; and

$$\varphi(\eta, P) = \begin{cases} 1 & \text{if } \eta < 1 \text{ and } P > 0 \\ 0 & \text{if } \eta = 1 \text{ or } P = 0 \end{cases}$$

is the kinetic law.

In addition, we use the following dimensionless variables and parameters:

$\theta = \frac{E}{RT_0^2}(T - T_0)$ is the temperature;

$\eta = \frac{C_0 - C}{C_0}$ is the transformation depth;

$\tau = \frac{k_0 \exp\left(-\frac{E}{RT_0}\right)}{\mathrm{Td}} t$ is time;

$\xi = \frac{x}{R_0}$ is the spatial coordinate;

$V = \frac{u\mathrm{Td}}{R_0 k_0 \exp\left(-\frac{E}{RT_0}\right)}$ is the filtration rate in the porous sample;

$\mathrm{Fk} = \frac{Q\rho_c}{\lambda_c}\frac{E}{RT_0^2}R_0^2 k_0 \exp\left(-\frac{E}{RT_0}\right)$ is the Frank-Kamenetskiĭ criterion;

$\mathrm{Fk}_f = \frac{Q\mu_0 \times \mu}{c_c\rho_c r^2 RT_0}\frac{E}{RT_0^2}R_0^2 k_0 \exp\left(-\frac{E}{RT_0}\right)$ is the filtration criterion;

$\mathrm{Td} = \frac{c_c}{Q}\frac{RT_0^2}{E}$ is the Thodes criterion;

$\mathrm{Ar} = \frac{RT_0}{E}$ is the Arrhenius criterion;

$\mathrm{Bi} = \frac{\alpha R_0}{\lambda}$ is the Biot criterion; and

$\mathrm{Ze} = \frac{E}{RT_0^2}(T_0 - T_i)$ is the Zel'dovich criterion.

Furthermore, T, T_0, and T_i are the current, environment, and initial temperatures, respectively; P_0 and P are the initial and current pressures; C_0 and C are the initial and current concentrations of the condensed reagent; E and k_0 are the activation energy and the preexponential factor of the reaction; Q is the reaction thermal effect (per unit volume of the substance); ρ, ρ_c, and ρ_p and c, c_c, and c_p are the densities and specific heat capacities for the gas, the condensed substance, and the reaction product, respectively; α is the coefficient of the heat transfer into the environment; m and m_0 are the volume fractions of the condensed substance at the current and initial time moments; μ and μ_0 are the viscosity and the molecular mass of the gas; ν is the stoichiometric coefficient of the reaction; u is the filtration rate; R is the universal gas constant; R_0 is the sample radius; and r is the characteristic size of particles of the porous substance.

ANALYSIS OF THE RESULTS

The given problem is of a multiparameter nature and involves a large number of various effects. Since we cannot discuss all of them, we restrict our consideration by describing the most important. In the analysis, it is convenient to distinguish two principal phenomena: the thermal interaction of the reacting porous mass with the environment and the deficiency of the gaseous reagent in the process of exothermic chemical interaction. The deficiency is defined as an inconsistency between the needed and available resources of the gaseous reagent so that it depends on the dynamics of the process. For example, in the initial period, the process develops slowly and can be maintained by the original intraporous gas or by the relatively low-intensity filtration flow. At the fast stages, there arises a deficiency of the gaseous reagent. For simplicity, we consider three states of the gas deficiency, i.e., (a) the case when the deficiency is absent, (b) the case when the deficiency manifests itself, and, finally, (c) the case when a significant level of the deficiency is established. The level (a) corresponds to a thermal explosion of quasi-homogeneous systems. We now recall basic features of the structures under study [8] and dynamics of characteristic post-induction processes with allowance for the stage of the initial heating ($\mathrm{Ze} \neq 0$). For small values of the Fk criterion, after a short heating period the exothermic heat release has time to dissipate into the environment. In this case, the slow transformation occupies the bulk of the reagents and occurs in a weak-gradient field. With increasing the Fk criterion (in its relatively narrow variation range), the process of the chemical interaction abruptly changes. In this case, the heat released in the process of exothermic chemical transformation no longer has time to dissipate into the environment. As a result, the temperature of the reacting mixture elevates, the rate of the chemical interaction increases, and the heat release more noticeably exceeds the heat removal. This self-accelerated process is the essence of the thermal explosion. The thermal ignition forms a frontal transformation mode going away from the center of the reacting volume towards its outer boundary [5, 8].

If the value of Fk is sufficiently large and the thermal interaction proceeds in the mode corresponding to the preliminary heating of the original low-temperature medium ($Ze \neq 0$), then the front formation is determined by the stage of heating the reagents by a hot environment (the so-called ignition regime [9]). The front of the high-temperature synthesis shifts away from the surface towards the central part of the reaction volume. For intermediate values of the Fk criterion, the self-ignition nucleus lies between the surface and the central part of the volume. In this case, two fronts of high-temperature transformation are formed. One of them shifts towards the center, while the other moves in the opposite direction.

In the course of interaction between a porous medium and a chemically active gas in the absence of its deficiency (at sufficiently large intraporous pressures or under the condition of an intense gas transport from the environment), we observe the formation of the same space-and-time structures of the temperature field and similar front dynamics in the post-induction period [5, 8]. Certain distinctions arise only due to the convective mass-and-heat transfer, the intraporous pressure variations, etc.

For example, in the case of the formation of two transformation fronts (when frontal regimes are maintained by the intense filtration transport of the gaseous reagent into the reaction zone), the post-induction dynamics of the thermal explosion turns out to be different from dynamics in homogeneous and quasihomogeneous media (Fig. 1). Here, the filtration flow turns out to be opposite the front propagating towards the surface of the porous mass and cocurrent to the front moving to the center. The counter filtration flow not only supplies the reaction zone of the front moving towards the surface with gas but also passes by it, being consumed in the front propagating towards the center. As a result, the temperature in the reaction zone is lowered to a critical value corresponding to the combustion disruption (time moment *2* in Fig. 1). Only the front moving towards the center remains active. As is seen, the temperature in the zone of the other active front drops to the environmental temperature [Fig. 1, $\theta(\tau, \xi)$ changing at the time moment *3*]. After completing the combustion process in the central zone of the porous system, passing of the cold gas through the zone of the extinguished front is stopped. Therefore, the process of its cooling is completed. In a certain induction period, the extinguished front arises again by the repeated self-ignition process and propagates towards the surface (the time moment *4* in Fig. 1). Thus, the complete transformation of the porous system proceeds by two self-ignitions of the condensed medium.

Features of the thermal explosion in porous systems begin to manifest themselves when the deficiency of the gas component appears. For the intermediate deficiency level (b), the induction period of the thermal explosion virtually preserves its features in quasihomogeneous systems. All the features manifest themselves in the post-induction period. In the absence of thermal explosion, we deal with a low-temperature weak-gradient field. At the initial stage, the chemical interaction is of a bulk nature. Furthermore, the interaction proceeds in the near-surface zone. In the inner part of the volume, the transformation is hampered by the deficiency of the active gas. However, after the complete transformation of the near-surface part it becomes inert, and the active gas is easily filtered into inner layers. The transformation of the inner part of the porous system has a layered-frontal character [10]. It is worth noting that decreasing the permeability of porous reaction products to zero can make the transformation of the inner volume of the porous compound impossible.

The increase in the Fk criterion (passage into the parametric zone of the thermal explosion in the center of the reaction volume) gives rise to self-ignition and to the formation of the incomplete-transformation front. The front will move from the center to periphery, its transformation incompleteness being caused by the deficiency of the gaseous reagent. The degree of the transformation in the front is determined by the amount of inner gas resources and those transported by filtration. Upon approaching the surface, the transformation depth in the front becomes complete. At this time moment, a reverse afterburning front is formed and then propagates towards the center of the porous compound. In the filtration combustion front, transformation completeness is attained and the propagation rate is determined by the filtration processes for the active gaseous reagent.

At higher values of the Fk parameter, two combustion fronts with incomplete transformation are formed (Fig. 2). The front moving towards the center uses the resources of the gaseous reagent, which are concentrated in the central part of the reaction zone. These resources are insufficient; moreover, the deepest layers give up intraporous gas (by filtration) to the approaching front. Therefore, the resources of the gaseous reagent drop, and the transformation depth in the front also decreases as it approaches the center. The front propagating towards the periphery (as in the preceding case) increases the degree of the transformation. When the complete transformation depth is attained in the reaction front (the time moment *2* in Fig. 2), we observe the formation of the reverse front providing the final transformation of inner layers of the porous medium. At large values of the Fk criterion (in the ignition regime), the propagation of only one front of the complete transformation towards the center is observed.

We now analyze temperature dynamics of the process under consideration. The slower afterburning front, often being limited by slow filtration gas transport, is accompanied by a considerable heat loss in the environment. The heat loss can be rather significant, so it is possible to observe two qualitatively different temperature dynamics for the propagation of the afterburn-

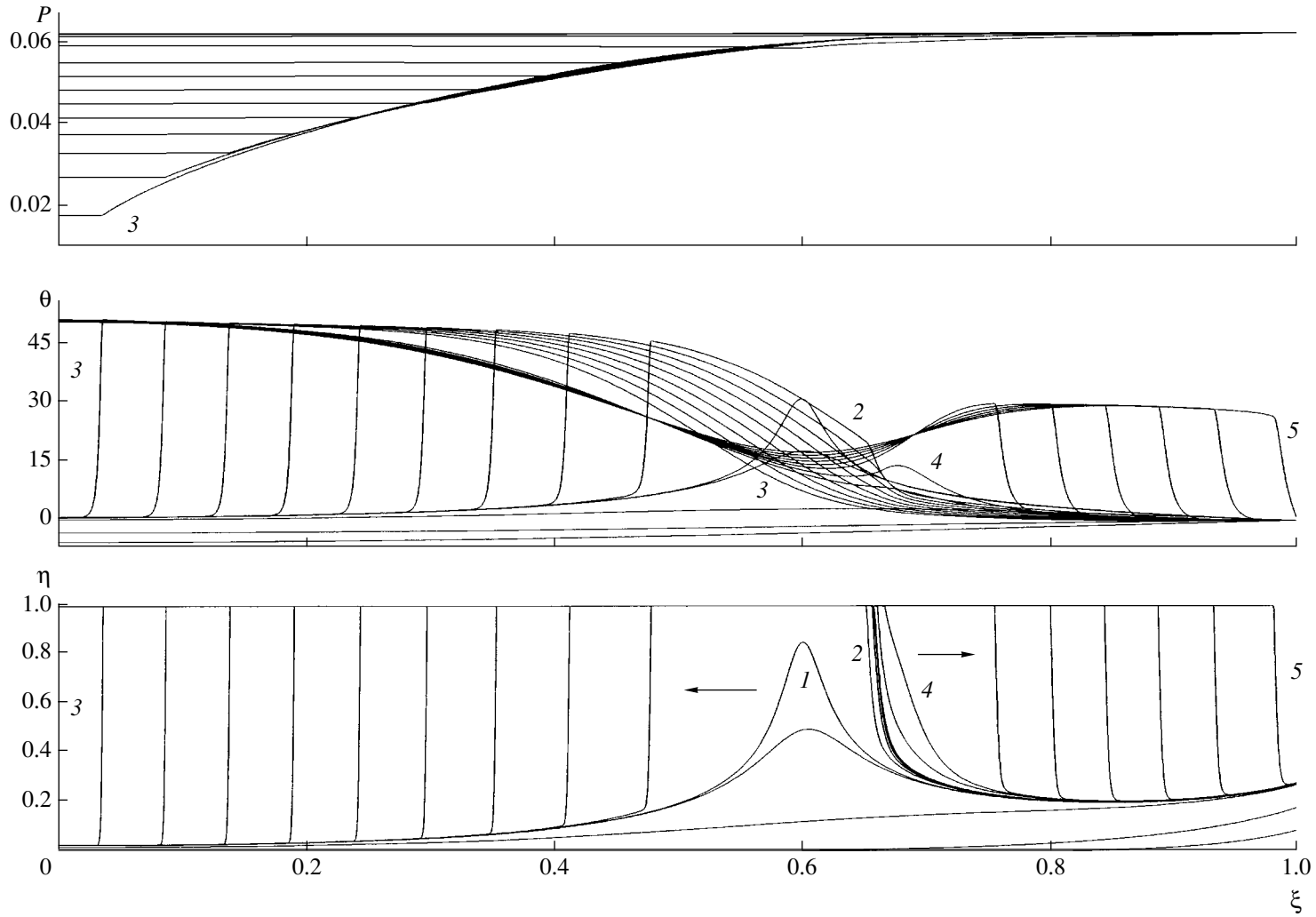

Fig. 1. Dynamics of thermal explosion in the double self-ignition mode (Fk = 20.8, Fk_f = 2.6, Td = 0.0185, Ar = 0.055, Bi = 450, Ze = 7.2, P_0 = 0.062, m_0 = 0.5, and ν = 0.5): (*1*) thermal self-ignition, τ = 15.2124; (*2*) disruption of the transformation front propagating towards the surface, τ = 15.2176; (*3*) time moment of combustion of the central zone in the porous compound, τ = 15.3713; (*4*) repeated self-ignition, τ = 15.3937; (*5*) completion of the combustion process, τ = 15.4478.

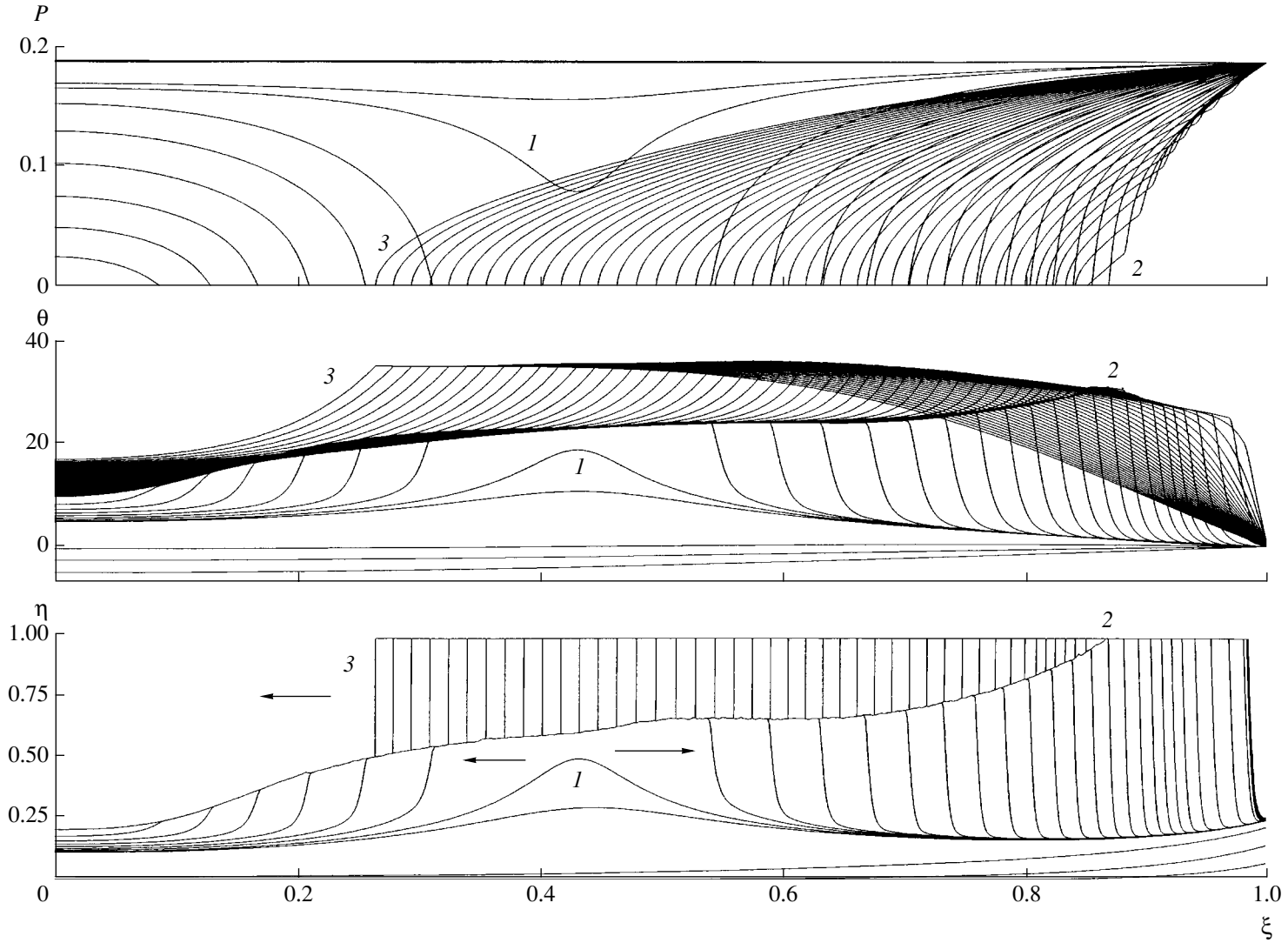

Fig. 2. Space-and-time distribution of thermal-explosion characteristics under conditions of the intermediate deficiency level of the gaseous reagent (Fk = 13.32, Fk_f = 1.56, Td = 0.0185, Ar = 0.055, Bi = 360, Ze = 7.2, P_0 = 0.188, m_0 = 0.5, and ν = 0.5): (*1*) thermal self-ignition, τ = 13.5809; (*2*) time moment for the appearance of the reverse final-transformation front, τ = 13.631; (*3*) filtration-combustion front, τ = 14.0445.

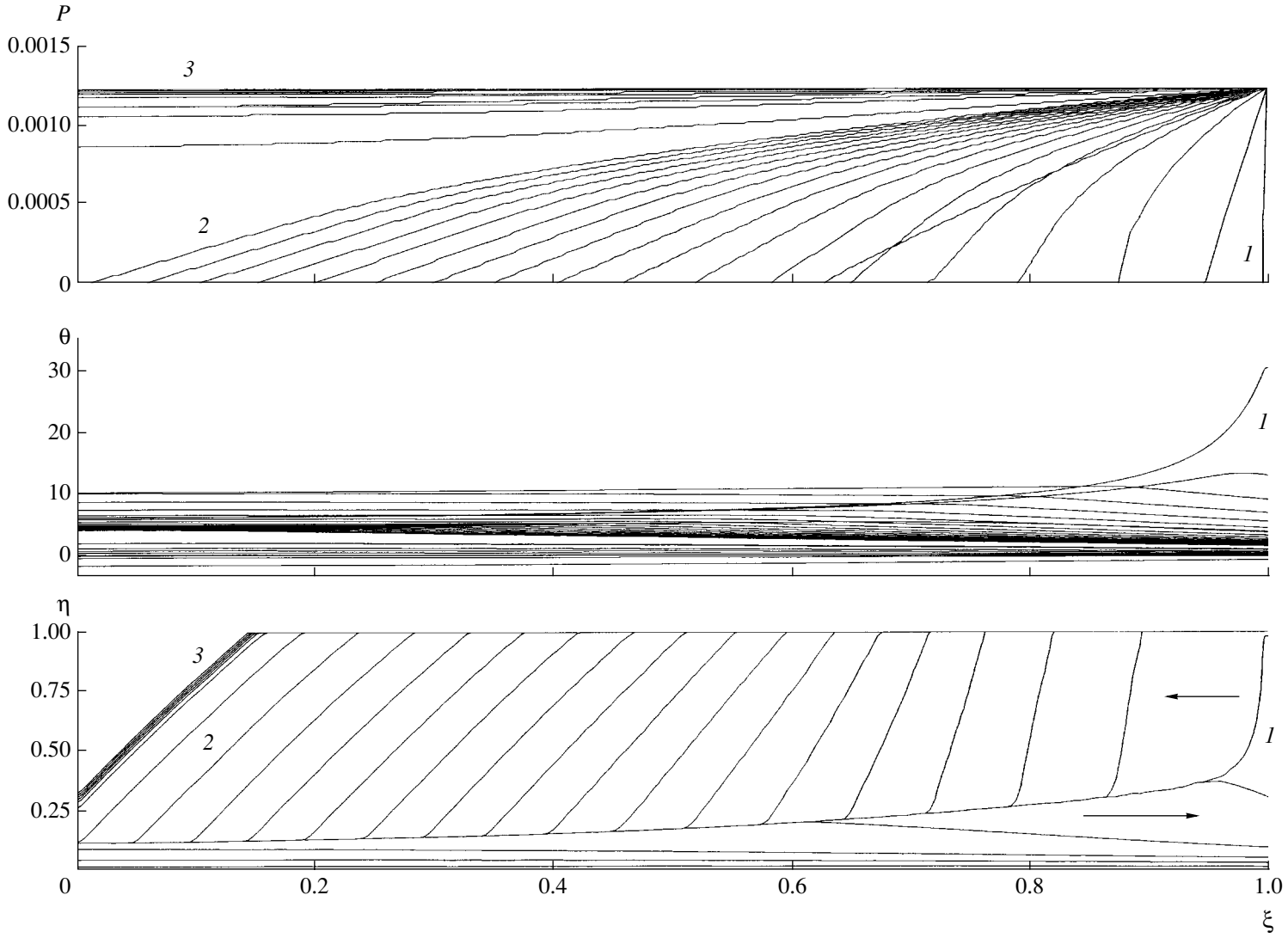

Fig. 3. Dynamics of the thermal explosion limited by the filtration transport of the gaseous reagent from the outside (Fk = 0.48, Fk_f = 0.06, Td = 0.0065, Ar = 0.045, Bi = 1, Ze = 3.6, P_0 = 0.00124, m_0 = 0.5, and ν = 0.5): (*1*) thermal self-ignition, τ = 7.4369; (*2*) time moment of the disruption into the low-temperature afterburning mode, τ = 13.1879; (*3*) low-temperature transformation mode, τ = 23.9389.

ing front. In the first case, we deal with heating the reaction products as a result of the exothermic transformation, which is characteristic of thermal fronts, and the decrease in the temperature of heated products, which is caused by heat removal into the environment. In the second case, the exothermic transformation of the incompletely reacted initial porous compound can only partially compensate the process of heat removal. The temperature in the front does not increase. Its variation is determined by the interaction of the energy release in the front of the low-rate filtration combustion and the slow heat exchange with the environment. The additional transformation can turn out to be so slow that there occurs a self-accelerating thermal damping of the exothermic transformation of the porous medium (combustion disruption), which is reverse to the thermal explosion. The completeness of the interaction proceeds in the layered-frontal mode (see [10]).

Under conditions of small pressures and weak filtration, the deficiency of the gaseous reagent becomes a significant factor in dynamics of the thermal explosion both in the induction and post-induction periods [(*c*) level]. In the case of increased heat removal, the temperature of the porous compound is close to the environmental temperature. In the inner zone, the intraporous gas is almost completely exhausted as a result of the chemical transformation. The most favorable conditions for the progress of the exothermic reaction are realized in the near-surface region of the porous compound in which the chemical interaction is replenished by filtration gas flow. A situation arises similar to that described by Zel'dovich in [11] for intradiffusion regimes. The thickness of the chemical-transformation zone is limited by the transport of the gaseous reagent. In turn, this transport is limited by chemical consumption. The origination of the thermal explosion (thermal self-ignition) under the condition of the gaseous-reagent deficiency is possible only in the near-surface region and only under conditions of a strongly-exothermic reaction capable of maintaining the self-accelerating temperature regime of chemical interaction in the zone limited by the filtration transfer. The transformation occurring in the post-induction period is disrupted into the low-temperature regime and corresponds to layered-frontal dynamics. Either the layered or frontal character of the transformation is determined by the size of the medium, by the thickness of the burnt near-surface layer, and by the filtration characteristics of the original compound and the final product. Even in the case when the initial resources of the gaseous reagent provoke the appearance of self-ignition inside the porous volume, the self-accelerating temperature process occurring in it is damped by burning out the gaseous reagent, and the process of spontaneous ignition shifts towards the surface. The space-and-time distributions for pressure, temperature, and transformation depth are shown in Fig. 3.

CONCLUSIONS

Knowledge of the thermal-explosion characteristics for the class of porous media under consideration makes it possible to properly organize the conditions of their storage and to evaluate the feasibility of the low-temperature transformation at the stage of storage.

The established characteristics of dynamics of the exothermic chemical interaction allow us to control the temperature and pressure of the process at the qualitative level, as well as the volume and frontal character of the transformation, by changing or choosing the amount of interacting condensed mass, its filtration parameters, initial temperature, and the pressure of the external gaseous medium. This is of particular interest for developing functionally gradient materials.

At the same time, the complicated nonlinear dependences of temperature and concentration fields testify to an essential inhomogeneity of the synthesis processes in the thermal-explosion mode, which may stimulate the inhomogeneity of characteristics of synthesis products in applications of the phenomenon of thermal explosion as a technological method.

REFERENCES

1. A. G. Merzhanov, V. V. Barzykin, and V. G. Abramov, Khim. Fiz. **15** (6), 3 (1996).
2. A. G. Merzhanov and I. P. Borovinskaya, Dokl. Akad. Nauk SSSR **204**, 366 (1972).
3. A. G. Merzhanov, Izv. Akad. Nauk, Ser. Khim., No. 1, 8 (1997).
4. V. V. Barzykin, Int. SHS J. **2**, 390 (1993).
5. A. G. Merzhanov, N. I. Ozerkovskaya, and K. G. Shkadinskiĭ, Dokl. Akad. Nauk **362**, 60 (1998).
6. K. G. Shkadinskiĭ and N. I. Ozerkovskaya, Dokl. Akad. Nauk **373**, 69 (2000).
7. P. Kofstad, *High-Temperature Oxidation of Metals* (Wiley, New York, 1966; Mir, Moscow, 1969).
8. A. G. Merzhanov, N. I. Ozerkovskaya, and K. G. Shkadinskiĭ, Khim. Fiz. **29** (10), 79 (2000).
9. A. G. Merzhanov, V. G. Abramov, and V. T. Gontkovskaya, Dokl. Akad. Nauk SSSR **148**, 156 (1963).
10. K. G. Shkadinskiĭ, N. I. Ozerkovskaya, and A. G. Merzhanov, Dokl. Akad. Nauk **378**, 784 (2001).
11. Ya. B. Zel'dovich, Fiz. Khim. **13**, 163 (1939).

Translated by Yu. Vishnyakov

Doklady Physics, Vol. 46, No. 12, 2001, pp. 849–852. Translated from Doklady Akademii Nauk, Vol. 381, No. 5, 2001, pp. 610–613.

TECHNICAL PHYSICS

Effects of Shape Memory and Superelasticity in Aged TiNi Single Crystals

Yu. I. Chumlyakov*, Corresponding Member of the RAS S. P. Efimenko, I. V. Kireeva*, E. Yu. Panchenko*, H. Sehitogly***, K. Gall****, and L. H. Yahia*******

Received July 9, 2001

Thermoelastic martensitic transformations from a high-temperature B2 phase to a monoclinic B19' phase can occur in TiNi single crystals as a result of cooling–heating processes and under the action of applied loads. In Ti–Ni alloys, these transformations give rise to the effects of shape memory and superelasticity [1, 2]. If B19' martensite arises under loading at temperatures $T > A_f$ (A_f is the final temperature of the reverse martensitic transformation while heating), then, under unloading, becoming thermodynamically unstable, it can be transformed into the B2 phase. Thus, the superelasticity is associated with the reversible martensitic transformations in the process of loading–unloading cycles. In the TiNi single crystals of the stoichiometric composition, the necessary conditions for the appearance of superelasticity are attained only after thermomechanical treatment, e.g., after cold deformation (ε = 20–30%) followed by annealing at T = 673–773 K. For nickel concentrations exceeding 50.6 at. %, the conditions for superelasticity appear due to the precipitation of disperse particles of Ti_3Ni_4 at annealing temperatures T = 673–773 K after both quenching and cold deformation ε = 30% [1, 2]. The precipitation of disperse particles improves the strength properties of the B2 phase due to dispersion solidification and suppresses the plastic flow processes in this phase in both direct and reverse martensitic transformations under loading [2]. As a result, the martensite crystals arising under loading preserve a high mobility and, being unloaded, transform into the B2-phase. The disperse particles of Ti_3Ni_4 have an atomic-ordered orthorhombic structure, undergo no thermoelastic transformations, and, consequently, their properties are inherited by martensite crystals. Since the lattice parameters for a particle and the matrix are different, the particles turn out to be sites of internal stresses and can serve as preferable nucleation centers of martensite.

In this study, we investigated an effect of the disperse Ti_3Ni_4 particles on the shape memory and superelasticity in (Ti–51 at. % Ni) single crystals aligned for tension in the ⟨111⟩ direction. Experiments with single crystals make it possible to avoid certain difficulties associated with the effects of grain boundaries in polycrystals on the development of thermoelastic martensitic transformations.

The Ti–51 at. % Ni crystals were grown by the Bridgman method. The preparation technique is described in [3].

We have shown experimentally that the aging of the crystals at (A) 823 K for 1.5 h, (B) at 773 K for 1 h, and (C) at 673 K for 1 h results in the precipitation of four crystallographically equivalent modifications of disperse Ti_3Ni_4 particles possessing a lens-like shape and habitus planes of the (111) type (Table 1).

Figure 1 shows curves for the released and absorbed heat, which were obtained by the method of differential scanning calorimetry in the course of heating–cooling cycles. As is seen, the number of peaks for the heat release on cooling depends on both the size d of particles and the distance L between them. In the crystals (A), three peaks of heat release are observed upon cooling. The first high-temperature peak is related to a B2–R transformation. This conclusion is based on a comparison between the temperatures for the onset R_s and the end R_f of the martensitic B2–R transformation and data obtained for polycrystals consisting of disperse particles with a close size [1, 2]. The second and third peaks are associated with the R–B19' martensite transformation. The former high-temperature R–B19' peak is related to the fact that disperse particles in (A) crystals are preferable martensite-nucleation sites due to the local stress fields produced by the particles. At the same time, the latter (R–B19') peak is related to the transformation in the bulk of the material. The reverse (B19'-R) transformation occurs as a single stage. The

* *Siberian Physicotechnical Institute, Novosobornaya pl. 1; Tomsk State University, pl. Revolyutsii, Tomsk, 634050 Russia*
** *Baĭkov Institute of Metallurgy, Russian Academy of Sciences, Leninskiĭ pr. 49, Moscow, 117334 Russia*
*** *University of Illinois, Urbana, USA*
**** *University of Colorado, Colorado, USA*
***** *Ecole Polytechnique de Montreal, Montreal, Canada*

1028-3358/01/4612-0849$21.00

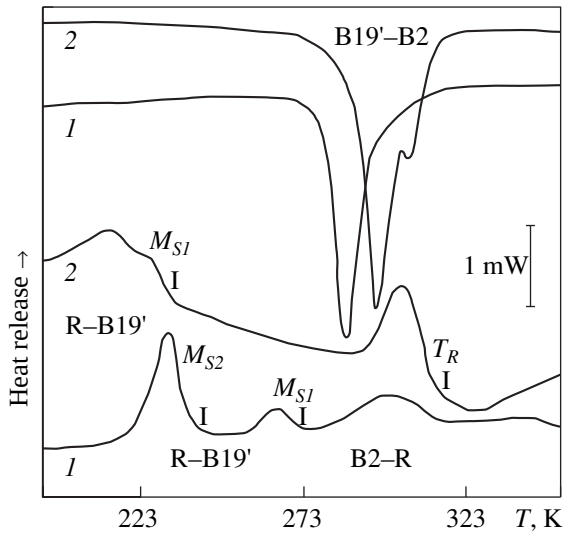

Fig. 1. Curves obtained by the method of differential scanning calorimetry for the (Ti–51 at. % Ni) single crystals after different thermal treatment: (*1*) 823 K, 1.5 h; (*2*) 773 K, 1 h.

decrease in particle sizes and interparticle distances in (B) crystals virtually does not change the values of R_s and R_f compared to (A) crystals. This conclusion is in agreement with the available data obtained while investigating (B2-R) transformations [1, 2]. In (B) crystals, both the direct (R–B19') and the reverse (B19'–B2) martensitic transformations are not divided into two-stage processes. Here, the peaks are superimposed with one another, forming a complicated shape (Fig. 1, curve *2*). After aging at 673 K for 1 h, the further decrease in particle sizes down to 30 nm and in the interparticle distances L = 30–40 nm results in insignificant changing R_s and shifting the points M_s and M_f of the martensitic R–B19' transformation towards the low-temperature region T < 77 K [1]. Thus, by changing the particle size and interparticle distances in Ti–51 at. % Ni single crystals, we can control not only temperatures of the direct and reverse martensitic transformations and the temperature hysteresis but also the number of stages of the (R–B19') transformation.

The disperse particles decrease the effect of the shape memory compared to quenched crystals and provide conditions for the appearance of superelasticity, which is unobserved in the quenched state. From Table 2, we can see that under tensile deformation of a ⟨111⟩ (Ti–51 at. % Ni) crystal the superelasticity reaches 8.8% and approaches a value calculated theoretically with allowance for only lattice deformations. This implies that, under deformation at $T < M_f$ (M_f is the final temperature of the martensitic transformation on cooling), a self-accommodating system of martensite crystals, which arises on cooling to the temperature $T < M_f$, transforms into a defect-free single crystal of the B19'-martensite due to the motion of interphase boundaries. Heating to $T > A_f$ leads to the transformation of this single crystal into the B2-phase single crystal [1]. In the case of (A), (B), (C) crystals containing disperse particles, the effect of the shape memory decreases nearly twice compared to quenched crystals (Table 2). Hence, the disperse particles make the detwinning difficult in the course of deformation at $T < M_f$, and B19'-phase single crystals are not formed. Physically, suppressing the detwinning of the B19'-martensite crystals is associated with the necessity to attain a compatibility [4] in the martensitic deformation of the matrix and the elastic deformation of Ti_3Ni_4 par-

Table 1. Parameters of the (Ti–51 at. % Ni) single-crystal microstructure after different thermal treatment

Thermal treatment	Particle size, nm	Interparticle distance, nm	Volume fraction of particles, %	Concentration of Ni in the matrix after aging, at. %
(A) crystal 823 K, 1.5 h	430	360–380	9.0	50.52
(B) crystal 773 K, 1 h	100	90–110	9.1	50.51
(C) crystal 623 K, 1 h	30	30–40	9.4	50.49

Table 2. Functional properties of Ni–Ti ⟨111⟩ single crystals

Alloy	Thermal treatment	Shape memory effect ε_{SE}, %	ΔT_{SE}, K	ε_{SE} at $T = A_f + 10$ K
Ti–51 at. % Ni	Quenching at 1203 K for 1 h	Experiment 8.8%, theory 9.8%	–	–
	(A) 823 K, 1.5 h	5.5	30	5.4
	(B) 773 K, 1 h	5.5	30	5.3
	(C) 673 K, 1 h	5.4	150	4.2
Ti–51.5 at. % Ni	823 K, 1.5 h	3.5	35	3.0

ticles which undergo no (B2–B19') martensitic transformations. Therefore, the (001)⟨100⟩ compound twinning observed experimentally by methods of electron microscopy of thin foils in aged polycrystals with a close composition [5] can be considered as geometrically necessary twinning arising in the B19'-martensite crystals while developing the thermoelastic (B2–B19') martensitic transformation in a structure-inhomogeneous material. Such aging polycrystals and single crystals of TiNi can be considered as natural nanocomposite materials in which disperse Ti_3Ni_4 particles of a diameter d = 30–400 nm provide the reinforcement. Note that, in this case, they do not undergo (B2–B19') martensitic transformation, whereas the Ti–Ni matrix can be transformed into B19' martensite both on cooling and under loading. Such an approach makes it possible to explain a change in the twinning type of the (Ti–50.2 at. % Ni) polycrystals with twinning according to the type I and II for grain sizes $d > d_{cr}$ = 2 μm to the compound ⟨100⟩(001) twinning with $d < d_{cr}$ [6]. In this case, as in alloys with disperse particles, the compatibility of martensitic deformation of neighboring grains is attained due to the compound twinning of B19' martensite. The compound twinning has the smallest Bürgers vector (b = 0.2 nm) compared to twinning according to types II and I [7]. Therefore, the process of the twinning of B19' martensite by dislocations with the smaller Bürgers vector and the preservation of the deformation compatibility of neighboring grains in microcrystals of TiNi become most favorable from the energy standpoint. In aged crystals, the density of compound twins will now depend on both the volume fraction of Ti_3Ni_4 particles and the distance between them. Therefore, the decrease in the effect of the shape memory in Ti–51.5 at. % Ni crystals compared to Ti–51 at. % Ni (Table 2) is related to increasing the density of compound twins in accordance with conclusions of the gradient theory of plasticity [4].

For crystals in different structural states, the dependence $\sigma_{cr}(T)$ is presented in Fig. 2. As is seen, all curves $\sigma_{cr}(T)$ are characterized by three different intervals. The first high-temperature interval is characterized by an ordinary dependence of $\sigma_{cr}(T)$ and is associated with the B2-phase deformation. The crystals (C) have the best properties in the B2 phase due to the strong effects of the dispersion solidification, which are caused by both elastic fields of disperse Ti_3Ni_4 particles and their atomic order. The second linear interval in the $\sigma_{cr}(T)$ curve, which is related to developing the martensitic transformation under loading, is anomalous. Under loading, the temperature range of the martensitic transformation ΔT depends on the level of B2-phase strength properties. In the (C), (B), and (A) crystals, ΔT = 300, 150, and 100 K, respectively. For the quenched crystals, ΔT = 250 K (Fig. 2). The comparison of the M_s temperatures obtained by methods of differential scanning calorimetry with the data taken from the temperature dependence $\sigma_{cr}(T)$ shows that its minimum corresponds

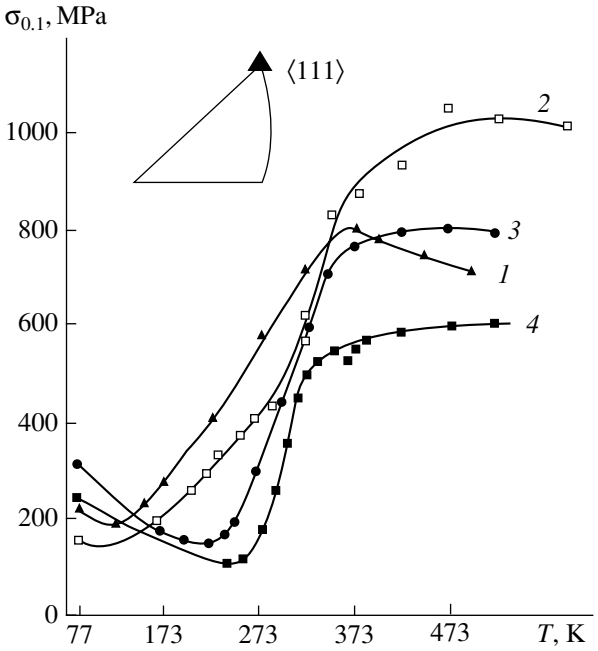

Fig. 2. Temperature dependence of axial stresses $\sigma_{0.1}$ for the (Ti–51 at. % Ni) ⟨111⟩ single crystals under tension after different thermal treatment: (*1*) quenching at 1203 K, (*2*) 673 K, 1 h, (*3*) 773 K, 1 h, and (*4*) 823 K, 1.5 h.

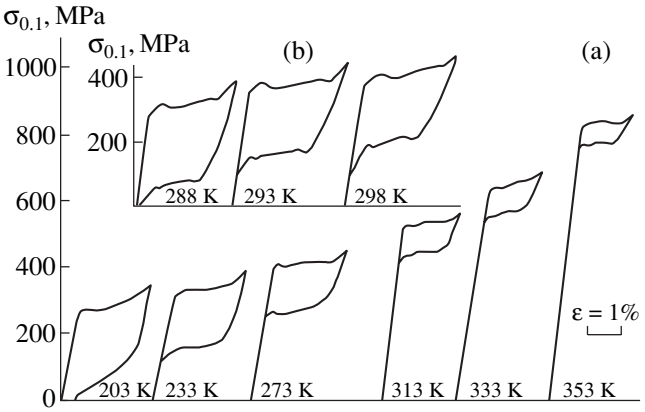

Fig. 3. Superelasticity loop as a function of the testing temperature for (Ti–51 at. % Ni) ⟨111⟩ single crystals under tension after different thermal treatment: (a) 673 K, 1h, (b) 823 K, 1.5 h.

to M_s. In the quenched state, the values of $\sigma_{cr}(M_s)$ are higher than those for aged crystals. The minimum values of $\sigma_{cr}(M_s)$ for (A) crystals, for which two peaks of the heat release are recorded, are associated with the two-stage development of the (R–B19') martensitic transformation. The third interval of the $\sigma_{cr}(T)$ curve (where $M_s < T <$ 77 K) is associated with the deformation of martensite crystals cooled due to the motion of both twin and interphase boundaries.

Finally, the precipitation of disperse Ti_3Ni_4 particles leads to the appearance of superelasticity in ⟨111⟩ crys-

tals under tension (Figs. 3a and 3b), which is absent in the particle-free crystals. The magnitude ε_{SE} of the superelasticity, the temperature range ΔT_{SE} for its observation (the so-called superelasticity window), and the value $\Delta\sigma$ of the mechanical hysteresis depend on the sizes and the volume fraction of particles as well as the testing temperature. First, in the case of large particles [(A) crystal], the superelasticity window is ΔT_{SE} = 30 K, while $\Delta\sigma$ = 220 MPa and slightly depends on temperature (Fig. 3b, Table 2). Second, the passage to small particles [(C) crystal] increases ΔT_{SE} up to 150 K. At the same time, $\Delta\sigma$ and ε_{SE} become temperature-dependent (Fig. 3a, Table 2). The superelasticity features mentioned above were not previously observed in Ti_3Ni_4-based single-phase alloys and, therefore, may be related to developing reversible thermoelastic transformations under loading in the crystals containing the particles. In the case of large particles [(A) crystal], where martensite crystals preserve particle properties, the formation of defects in the crystalline structure easily occurs at the particle–martensite boundary [4]. If the particles are small [(C) crystal], these processes are suppressed. Therefore, in this case the superelasticity range exceeds by a factor of 5 that for large particles.

Thus, the disperse Ti_3Ni_4 particles undergoing no martensitic transformation turn out to be an important tool in governing the sequence of the martensitic transformations. In addition, these particles determine the magnitudes of the effects of shape memory and superelasticity, of the superelasticity window, and of the mechanical hysteresis.

ACKNOWLEDGMENTS

This work was supported by the Russian Foundation for Basic Research (project nos. 99-03-32579 and 01-03-06151) and the Ministry of Education of the Russian Federation (project no. E00-3.04.29).

REFERENCES

1. K. Otsuka, Y. Shimizu, K. Shimizu, *et al.*, *Alloys with the Shape Memory Effect* (Hiroyasu Funakudo, Tokyo, 1984; Metallurgiya, Moscow, 1990).
2. V. G. Pushin, V. V. Kondrat'ev, and V. N. Khachin, *Pretransition Phenomena and Martensitic Transformations* (Yekaterinburg, 1998).
3. K. Gall, H. Sehitogly, I. Karaman, *et al.*, Acta Metal. Mater. **48**, 3311 (2000).
4. A. F. Ashby, Philos. Mag. **21**, 399 (1970).
5. C. M. Wayman, M. Nishida, and A. Chiba, Metallography **21**, 275 (1988).
6. M. Nishida, K. Kitamura, I. Itai, *et al.*, J. Phys. IV **5**, C8-635 (1995).
7. M. Nishida, H. Ohgi, I. Itai, *et al.*, Acta Metal. Mater. **43**, 1219 (1995).

Translated by Yu. Vishnyakov

Doklady Physics, Vol. 46, No. 12, 2001, pp. 853–855. Translated from Doklady Akademii Nauk, Vol. 381, No. 6, 2001, pp. 770–772.

TECHNICAL PHYSICS

On an Effect of Dislocations on the Surface Tension at the Interface between Two Materials

R. V. Goldstein* and M. E. Sarychev**

Presented by Academician A.Yu. Ishlinskiĭ June 27, 2001

Received July 12, 2001

Dislocations are one of the most important types of defects in a crystalline structure. Their presence specifies, first of all, the mechanical properties of solids [1, 2]. Recently, it was experimentally shown that dislocations also affect adhesive characteristics of both thin-film coatings [3] and multilayer systems [4]. Since the adhesive properties of materials, in turn, are determined by their surface tension [5], dislocations, in addition, must affect surface tension. At the moment, there exists no theoretical explanation of this phenomenon.

Based on a certain model, we show in this paper that the surface tension σ_{12} of the interface between two materials 1 and 2 is actually dependent on both the density and the distribution of dislocations in their bulk.

In further analysis, we employ a thermodynamic approach based on the Gibbs equation describing the change $d\sigma_{12}$ in the interface surface tension caused by the variations of thermodynamic parameters of the volumes that form the interface [6].

Let temperature and pressure in the system under consideration remain constant and the change in its thermodynamic state be associated with the change in the structural-defect state (in the case under consideration, these are dislocations) in the volumes of materials 1 and 2. Then the Gibbs equation has the form [6]

$$d\sigma_{12} = -\Gamma_1 d\mu_1 - \Gamma_2 d\mu_2, \qquad (1)$$

where $d\mu_1$ and $d\mu_2$ are the variations in the chemical potentials for the volumes of the corresponding materials, and Γ_1 and Γ_2 are the densities (calculated per unit area of the interface) of dislocations in the interface.

Here, we consider the so-called large-angle interfaces [7] that can have a thickness of several (and even larger) atomic diameters. Such interfaces consist of domains with the structure of each of the materials forming the interface and contain dislocations. The densities Γ_1 and Γ_2, which enter into Eq. (1), are considered to be continuous and independent of the dislocation volume densities in each of the materials. In this case, integrating (1), we obtain

$$\sigma_{12} - \sigma_{12}^{(0)} = -\Gamma_1(\mu_1 - \mu_1^{(0)}) - \Gamma_2(\mu_2 - \mu_2^{(0)}), \qquad (2)$$

where $\sigma_{12}^{(0)}$, $\mu_1^{(0)}$, and $\mu_2^{(0)}$ are the integration constants.

To find μ_1 and μ_2, we use the fact that the chemical potential can be obtained by differentiating any of the thermodynamic potentials or the internal energy of the solid with respect to the number of particles [8]. Applying this method to the dislocation system in each of the volumes, we obtain

$$\mu_i = \left[\frac{\partial(E_i N_i)}{\partial N_i}\right]_{s_i, v_i}, \quad i = 1, 2, \qquad (3)$$

where E_i, N_i, and s_i are, respectively, the energy of an individual dislocation, the number of these dislocations, and their entropy in the ith material, while v_i is its volume.

We consider the energies E_i for two limiting cases corresponding to reasonably high and low dislocation densities, respectively.

1. HIGH DISLOCATION DENSITIES

Let the dislocation density c_i in each of the materials be so high that the mean distance between the neighboring dislocations $d_i \sim c_i^{-1/2}$ is much smaller than the distance from the dislocations to the interface between the materials or to their free surfaces. In this case, the dislocation energy E_i is determined by the dislocation nearest neighbors [1]. In particular, for rectilinear parallel dislocations of the mixed type (superposition of the edge and screw dislocations) in the approximation suggested by Nabarro [2],

$$E_i = \frac{G_i b_i^2 L_i}{4\pi(1-\nu_i)}(1 - \nu_i \cos^2\varphi_i)\ln\frac{c_i^{-1/2}}{b_i}, \qquad (4)$$

* *Institute for Problems in Mechanics, Russian Academy of Sciences, pr. Vernadskogo 101, Building 1, Moscow, 117526 Russia*

** *Institute of Physics and Technology, Russian Academy of Sciences, ul. Krasikova 24a, Moscow, 117218 Russia*

1028-3358/01/4612-0853$21.00

where b_i, G_i, and ν_i are the modulus of the Bürgers vector, the shear modulus, and the Poisson ratio for the ith material, and L_i and φ_i are the dislocation length and the angle between the Bürgers vector and the dislocation line. Substituting formula (4) into expression (3) and taking into account that $c_i = \frac{N_i}{A_i}$ (A_i is the cross section of the ith material, which is crossed by the dislocations), we arrive at

$$\mu_i = -2\gamma_i[\ln(c_1^{1/2}b_i) + 1],$$
$$\gamma_i = \frac{G_i b_i^2 L_i}{8\pi(1-\nu_i)}(1-\nu_i\cos^2\varphi_i). \quad (5)$$

Furthermore, employing relationship (5), we obtain from equality (2)

$$\sigma_{12} - \sigma_{12}^{(0)} = \gamma_1\Gamma_1\ln\frac{c_1}{c_{1m}} + \gamma_2\Gamma_2\ln\frac{c_2}{c_{2m}}, \quad (6)$$

where constants c_{1m} and c_{2m} have the meaning of the minimum dislocation densities in the materials 1 and 2 for which Nabarro approximation (4) is still valid, and $\sigma_{12}^{(0)}$ is the corresponding surface tension of the interface. Since $c_i > c_{1m}$, it follows from expression (6) that the interface tension should increase with the dislocation density in the materials forming this interface. Taking into account that the deformation ability of a material is enhanced with the dislocation density [2], this result looks reasonable. Employing relation (6), we estimate the order of the quantity $\Delta\sigma_{12} \equiv \sigma_{12} - \sigma_{12}^{(0)}$. For example, for $G_i \sim 50$ GPa, $b_i \sim 2$ Å, $L_i \sim 1$ μm, $\nu_i \sim 0.3$, $\Gamma_i \sim 10^{10}$ 1/m^2, and $\frac{c_i}{c_{im}} \sim 10$–$10^3$, the value $\Delta\sigma_{12}$ reaches ~(0.1–1) J/m^2.

2. LOW DISLOCATION DENSITIES

Now let the dislocation density be so low that the mean distance d_i between dislocations is much larger than the distance to the interface between the materials. This case can be realized if the materials 1 and 2 are thin layers with the thicknesses $h_i < d_i$. The dislocation density usually varies from (10^6–10^7) 1/m^2 [i.e., $d_i \simeq$ (0.3–1) × 10^{-3} m] in perfect crystals up to (10^{15}–10^{16}) 1/m^2 [i.e., $d_i \simeq$ (1–3) × 10^{-8} m] in strongly distorted (hardened) metals [2].

For definiteness, we consider a plane-parallel three-layer system. This system lies in the scope of our interest, in particular, in connection with the modern structures prepared by means of microelectronic metallization. In such structures, a barrier layer (layer 2, e.g., W or Ta) is usually introduced in between the metal film (layer 1, Al or Cu) and the substrate (layer 3, Si).

We assume that the layers 1 and 2 are thin-film layers; i.e., their thicknesses h_i (i = 1, 2) satisfy the condition

$$h_i < d_i = c_i^{-1/2}. \quad (7)$$

Let the rectilinear dislocations in layers 1 and 2 be parallel to the plane of the interlayer interface 1–2 and to each other. Then we can assume that the set of dislocations in each of the layers approximately represents a one-dimensional chain parallel to the layer boundaries, and in this chain the mean distance between the dislocation lines is equal to d_i. We denote the distances to the 1–2 interface for the dislocation chains in the layers 1 and 2 as x_1 and x_2, respectively. Then the distance from the dislocation lines in layer 1 to the free surface of this layer is $h_1 - x_1$, and the distance from the dislocation lines in the layer 2 to the interfaces between the layers 2 and 3 is $h_2 - x_2$.

By virtue of conditions (7), x_1, $(h_1 - x_1) < d_1$, and x_2, $(h_2 - x_2) < d_2$. Then the energy E_1 of the dislocations in the layer 1 is determined by their interaction with both the interface 1–2 and the free surface, while the energy E_2 of the dislocations in the layer 2 is determined by the interaction with the 1–2 and 2–3 interfaces. Under these conditions, the energies E_i can be calculated by the method of image forces [1]. Substituting corresponding expressions from [9] into relations (3) and (2), we find the surface tension σ_{12} for the interface between the layers 1 and 2:

$$\sigma_{12} - \sigma_{12}^* = -\Gamma_1\frac{G_1 b_1^2}{4\pi} \times L_1\left[\frac{G_1 - G_2}{G_1 + G_2}\ln\frac{\alpha_1 x_1}{b_1} + \ln\left(\frac{h_1 - x_1}{b_1}\alpha_1\right)\right] \quad (8)$$
$$-\Gamma_2\frac{G_2 b_2^2}{4\pi}L_2\left[\frac{G_2 - G_1}{G_2 + G_1}\ln\frac{\alpha_2 x_2}{b_2} + \frac{G_2 - G_3}{G_2 + G_3}\ln\left(\frac{h_2 - x_2}{b_2}\alpha_1\right)\right].$$

Here we use the same notation as in (4); $\alpha_1 \simeq \alpha_2 \simeq 0.4$ are the coefficients determining the magnitude of the internal dislocation radius $r_{0i} = \frac{b_i}{\alpha_i}$. At the same time, the integration constant $\sigma_{12}^* = \sigma_{12}^{(0)} - \Gamma_1\mu_1^{(0)} - \Gamma_2\mu_2^{(0)}$ has the meaning of the difference between the magnitude of the interface tension for certain values of $x_1 = x_{10}$, $x_2 = x_{20}$ and the magnitude of the right-hand side of expression (8) with the substituted values x_{10} and x_{20}. Minimum values of x_1 and x_2 in expression (8) are equal to $\frac{b_1}{\alpha_1}$ and $\frac{b_2}{\alpha_2}$, respectively, and their maximum values are $h_1 - \frac{b_1}{\alpha_1}$ and $h_2 - \frac{b_2}{\alpha_2}$.

The analysis of expression (8) shows that $\sigma_{12} = \sigma_{12}(x_1, x_2)$ has a maximum for $x_1 = x_{1c}$ and $x_2 = x_{2c}$:

$$x_{1c} = \frac{P}{P-1}h_1,\ x_{2c} = \frac{P}{P+P'}h_2. \quad (9)$$

Here, $P = \frac{G_2 - G_1}{G_1 + G_2}$ and $P' = \frac{G_2 - G_3}{G_2 + G_3}$ in the case when the shear moduli for the layers satisfy the condition

$$G_2 < G_1, \quad G_2 < G_3. \quad (10a)$$

In the case when

$$G_2 > G_1, \quad G_2 > G_3, \quad (10b)$$

σ_{12} has a minimum for $x_2 = x_{2c}$. This minimum is determined by expression (9) and monotonically increases with x_1.

For example, in the case of the Cu–Ta–Si system, we have $G_1 \simeq 40$ GPa, $G_2 \simeq 70$ GPa, $G_3 \simeq 1$ GPa [10]; i.e., condition (10b) is fulfilled, and, consequently, dislocations in the Ta barrier layer make a minimum contribution into σ_{12}, provided that they are on average at a distance $x_{2c} \simeq 0.2h_2$ from the Cu–Ta interface.

We now evaluate the quantity $\Delta\sigma_{12} \equiv \sigma_{12} - \sigma_{12}^*$ for the same (as before) values of the G_1, G_2, and G_3 moduli. Thus, for $x_1 \sim 0.5h$, $x_2 \sim 0.5h_2$, $h_1 \sim 1000$ Å, $h_2 \sim 100$ Å, and the same values of the remaining parameters that were used in Section 1, we obtain $\Delta\sigma_{12} \sim 0.1$ J/m^2.

Thus, the estimates given show that, regulating the density of dislocations and their distribution in the adjacent layers, we can efficiently control the magnitude of the surface tension and adhesive properties of the interface between two different materials.

REFERENCES

1. J. P. Hirth and J. Lothe, *Theory of Dislocations* (McGraw-Hill, New York, 1967; Atomizdat, Moscow, 1972).
2. *Physical Metallurgy*, Ed. by R. W. Cahn (North-Holland, Amsterdam, 1965; Mir, Moscow, 1968), Vol. 3.
3. S. L. Lehoczky, J. Appl. Phys. **49**, 5479 (1978).
4. T. Foeke and D. van Heerden, in *Chemistry and Physics of Nanostructures and Related Nonequilibrium Materials* (TMS, Pittsburgh, 1997), pp. 193–199.
5. A. J. Kinloch, *Adhesion and Adhesives: Science and Technology* (Chapman and Hall, London, 1987; Mir, Moscow, 1997).
6. B. S. Bokshteĭn, N. V. Kopetskiĭ, and P. S. Shvindlerman, *Thermodynamics and Kinetics of Grain Boundaries in Metals* (Metallurgiya, Moscow, 1986).
7. *Physical Metallurgy*, Ed. by R. W. Cahn (North-Holland, Amsterdam, 1965; Mir, Moscow, 1968), Vol. 1.
8. L. D. Landau and E. M. Lifshitz, *Course of Theoretical Physics*, Vol. 5: *Statistical Physics* (Nauka, Moscow, 1976; Pergamon, Oxford, 1980), Part 1.
9. J. S. Kochler, Phys. Rev. B **2**, 547 (1970).
10. *Handbook of Physical Quantities*, Ed. by I. S. Grigoriev and E. Z. Meilikhov (Énergoizdat, Moscow, 1991; CRC Press, Boca Raton, 1997).

Translated by T. Galkina

Doklady Physics, Vol. 46, No. 12, 2001, pp. 856–859. Translated from Doklady Akademii Nauk, Vol. 381, No. 6, 2001, pp. 773–776.

TECHNICAL PHYSICS

Generation of Shock Waves by Spherical Bubble Clusters in a Liquid

V. K. Kedrinskiĭ*, Academician Yu. I. Shokin, V. A. Vshivkov**, G. I. Dudnikova**, and G. G. Lazareva****

Received August 3, 2001

The problem on active media [1, 2] capable of absorbing and amplifying an external disturbance and then reemitting it in the form of an acoustic pulse is one of the problems of the so-called acoustic laser (acoustic analogue of laser systems). As was shown in [3] by numerical analysis of one-dimensional cases, bubble systems, both passive and containing explosive gaseous mixtures, can be treated as active media. In such media, an excitation caused by interactions with shock waves can lead to significantly amplifying the wave field and generating an intense shock pulse.

Keeping in mind that experiments with so-called free systems could turn out to be most crucial, it is interesting to analyze the interaction of shock waves with bubble clusters. Wave processes in such free systems involve phenomena of different temporal and spatial scales and are accompanied by the generation of shock waves with amplitudes as high as tens of MPa. These phenomena are determined by a great number of parameters; therefore, it is difficult or even impossible to analyze their effects in the course of a certain physical experiment. From this standpoint, the necessity to numerically simulate various states inherent in such complex acoustic active systems, including features of wave process occurring in them, seems to be evident.

Employing a nonequilibrium two-phase mathematical model for a bubble liquid, we numerically simulated a plane steady-state shock wave interacting with a passive spherical cluster. We here consider certain unexpected effects found in the course of this analysis, which are caused by both a difference in the velocities of acoustic-wave propagation in the cluster and in surrounding liquid and the actual cluster shape.

* *Lavrent'ev Institute of Hydrodynamics, Siberian Division, Russian Academy of Sciences, pr. Akademika Lavrent'eva 15, Novosibirsk, 630090 Russia*

** *Institute of Computer Technologies, Siberian Division, Russian Academy of Sciences, pr. Akademika Lavrent'eva 6, Novosibirsk, 600090 Russia*

FORMULATION OF THE PROBLEM

Let a velocity jump be given at the moment $t = 0$ at the end of a cylindrical shock tube filled with water and having the radius r_{st}. The center of a spherical bubble cluster with the radius R_{cl} ($R_{cl} < r_{st}$) is situated on the tube central z-axis at a distance l_{cl} from the end. The radii of the bubbles and their volume concentration are R_0 and k_0, respectively. At a moment $t > 0$, the shock wave propagating along the positive direction of the z-axis encounters the bubble cluster, rounds it, and is refracted into it. It is worth noting that the equilibrium sound velocity c_e in the cluster significantly depends on the volume concentration k_0. For example, in the case of $k_0 = 0.01$, the velocity slightly exceeds 100 m/s, being lower by an order of magnitude than the velocity of wave propagation in the liquid.

SYSTEM OF EQUATIONS

The Iordanskiĭ–Kogarko–van Wijngaarden modified set of equations is used here as a governing system of equations for describing wave processes in the bubble medium [4]. This system involves the known mass and momentum conservation laws (written out for the cylindrical domain $[0, r_{st}] \times [0, L]$, where L is the tube length) for the averaged quantities, namely, pressure p, density ρ, and velocity u, and the following equations determining a macroscopic state of the medium:

the Rayleigh equation

$$\beta\frac{ds}{dt} + \frac{3}{2}s^2 = C_1\frac{T}{\beta^3} - \frac{C_2}{\beta} - C_3\frac{s}{\beta} - p,$$

the temperature equation

$$\frac{dT}{dt} = (\gamma - 1) \times \mathrm{Nu}\frac{\beta^3(1-T)}{T} - 3(\gamma - 1)\frac{Ts}{\beta},$$

and the equation of state for the fluid

$$p = 1 + \frac{\rho_l c_0^2}{n p_0}\left[\left(\frac{\rho}{1-k}\right)^n - 1\right].$$

1028-3358/01/4612-0856$21.00

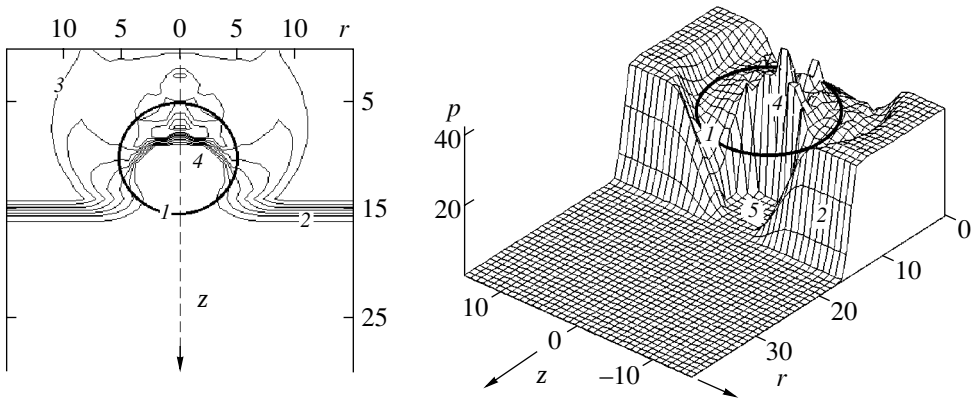

Fig. 1. Schematic diagram of a bubble cluster interacting with a shock wave and the distribution of pressure $p(r, z)$ at the time moment $t = 110$ μs: (*1*) cluster boundary, (*2*) front of an incident wave, (*3*) isobars, (*4*) shock-wave front in a cluster, and (*5*) unperturbed domain.

Here,

$$k = \frac{k_0}{1-k_0}\rho\beta^3, \quad \beta = \frac{R}{R_0}, \quad \frac{d\beta}{dt} = s,$$

$$\mathrm{Pe} = C_4(\gamma-1)\frac{\beta|s|}{|1-T|},$$

$$p = \frac{p_l}{p_0}, \quad t = \tau\frac{1}{R_0}\sqrt{\frac{p_0}{\rho_l}}, \quad \rho = \frac{\bar{\rho}}{\rho_l},$$

$\mathrm{Nu} = \sqrt{\mathrm{Pe}}$ if $\mathrm{Pe} > 100$, and $\mathrm{Nu} = 10$ if $\mathrm{Pe} \le 100$; and

$$C_1 = \frac{\rho_{g0}T_0B}{p_0M}, \quad C_2 = \frac{2\sigma}{R_0p_0},$$

$$C_3 = \frac{4\mu}{R_0\sqrt{p_0\rho_1}}, \quad C_4 = \frac{12R_0\sqrt{p_0/\rho_l}}{\nu},$$

where Pe and Nu are the Pecklet and Nusselt numbers, respectively.

SHOCK-WAVE FOCUSING BY A SPHERICAL CLUSTER

When an incident shock wave interacts with a bubble cluster, the excitation at different points of the cluster surface occurs with a retardation due to the velocity of shock-wave propagation being finite. The shock-wave velocity in a cluster is relatively low; the cluster shape thereby affects the wave propagation. Therefore, the shock wave formed in the cluster (as a result of the reemission of the refracted wave absorbed by the bubbles) strongly differs from that in the one-dimensional case. The picture of a bubble cluster interacting with a shock wave and the distribution of the relative pressure p (in units of the hydrostatic pressure $p_0 = 0.1$ MPa) over the space (r, z) are shown in Fig. 1 for the moment $t = 110$ μs. The calculation was performed for the incident-wave amplitude $p_{sh} = 3$ MPa, $k_0 = 0.01$, $R_0 = 0.01$ cm, $R_{cl} = 4.5$ cm, $l_{cl} = 10$ cm, $r_{st} = 15$ cm, and $L = 40$ cm. In the figures, all linear sizes are expressed in centimeters.

As is easily seen, the shock front *4* inside the cluster (*1* is the cluster boundary) is concave and the pressure gradient along the front is high. The latter fact is associated with the unsteady nature of the shock-wave formation process in the bubble medium. Moreover, at a fixed moment, different stages of this process turn out to be distributed over the shock front, which results in the origination of the above-mentioned gradient. At this stage, a rarefaction wave is formed inside the cluster and propagates outwards into the surrounding liquid. This wave arises due to the pressure drop beyond the refracted-wave front, which is caused by the wave absorption by the bubbles.

As follows from the calculation results [see Fig.1, $p(r, z)$], domain *5* of the bubble cluster, which is bounded by the curvilinear front of the wave generated by the bubbles, remains unperturbed in the vicinity of the far cluster boundary ($z \approx 10$–14.5 cm). This occurs despite of the fact that the incident wave front *2* has already rounded the cluster by the moment of 110 μs. The initial stage of the wave amplification becomes apparent at this moment. This is confirmed by Fig. 2. Indeed, the shock-wave focusing region in the cluster has essentially formed by the moment of 140 μs, and the pressure gradient along curvilinear front *4* in the bubble system is clearly seen.

Due to focusing, an intense wave with an amplitude p_{foc} as large as 30 MPa (see Fig. 3, $t = 160$ μs) is formed near the bubble cluster–liquid interface in the vicinity of the point $z \approx 13.5$ cm. As a result, the cluster emits shock wave *1* of the bore type, with a parabolic wave front (see Fig. 4, $t = 180$ μs). The pressure reaches its

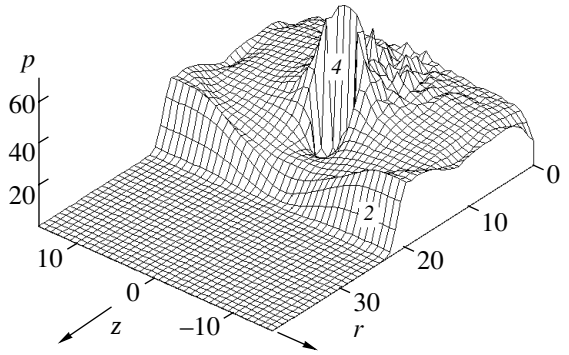

Fig. 2. Final stage of the shock-wave focusing in the bubble cluster at t = 140 μs: (*4*) curvilinear front with a pressure gradient.

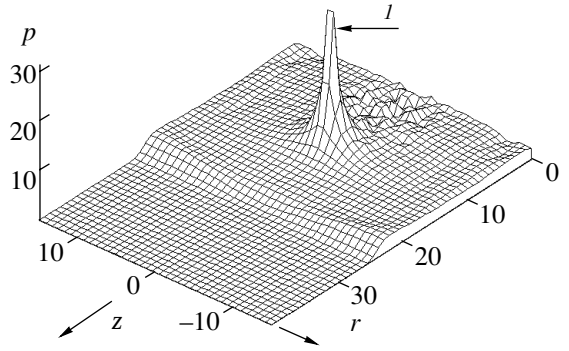

Fig. 3. Intense acoustic pulse (*1*) generated by the cluster at t = 160 μs.

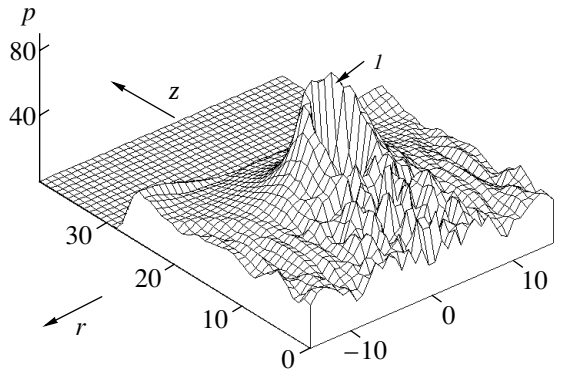

Fig. 4. Profile (*1*) of a shock wave emitted into the liquid by the bubble cluster at t = 180 μs.

maximum value at the axis of the parabola and drops fairly sharply along its branches.

It is necessary to emphasize that such focusing has unconventional features. Indeed, aside from the intense pressure gradient along the wave front, it is accompanied by the absorption and subsequent reemitting of the incident shock-wave energy by the gaseous bubbles. Thus, at each time step, a new wave originates in the cluster, with its front having a smaller radius of curvature. The stability of the wave-focusing process in the cluster was verified by introducing a specific disturbance having the shape of a liquid sphere with a radius r_{dr} of 0.5 to 1 cm. The sphere was placed inside the cluster, and its center lay on the z-axis at a distance $l_{dr} < l_{cl} - r_{dr}$ from the end. The calculation showed that the pressure-field disturbance caused by this sphere is weak and decreases rapidly. Therefore, it does not affect the final result.

As follows from the calculations, the pressure at the focal point depends on a number of parameters, namely, the volume concentration k_0 of the gaseous phase and the radii R_{cl} and R_b of the cluster and bubbles, respectively. These dependences can be approximated by the relationships

$$\frac{p_{foc}}{p_{sh}} \approx 1 + 1.56 \times 10^3 k_0 - 1.6 \times 10^4 k_0^2, \quad (1)$$

$$\frac{p_{foc}}{p_{sh}} \approx 1 + 2.6 R_{cl} + 0.11 R_{cl}^2, \quad (2)$$

$$\frac{p_{foc}}{p_{sh}} \approx 17.9 - 8.5 R_0 - 135.6 R_0^2. \quad (3)$$

All dependences (1)–(3) are obtained for p_{sh} = 3 MPa. In this case, we assumed in formulas (1), (2), and (3) that R_{cl} = 3 cm and R_0 = 0.1 cm, k_0 = 0.01 and R_0 = 0.2 cm, and k_0 = 0.01 and R_{cl} = 5 cm, respectively.

It is interesting that the ratio $\frac{p_{foc}}{p_{sh}}$ considered as a function of the incident shock wave amplitude p_{sh} has the maximum (in the vicinity of the point p_{sh} = 1 MPa), while the value of p_{foc} monotonically increases as

$$\frac{p_{foc}}{p_0} \approx 62\left(\frac{p_{sh}}{p_0}\right)^{0.21} - 30. \quad (4)$$

Dependences (1)–(4) are valid for the ranges

$$k_0 = 0\text{–}0.05, \quad R_{cl} = 1\text{–}5 \text{ cm},$$

$$R_0 = 0.05\text{–}0.3 \text{ cm, and } p_{sh} = 0.4\text{–}12 \text{ MPa}.$$

Analyzing the results obtained from the standpoint of principles of designing powerful pulsed acoustic sources, we can conclude that a passive spherical bubble cluster excited by a shock wave represents an active medium that can absorb and amplify an external disturbance and then reemit it in the form of an intense acoustic signal. The position of the focal region with respect to the cluster–liquid interface can be regulated by vary-

ing the volume concentration k_0 of the gaseous phase. Therefore, the emitted-wave absorption by the cluster in itself can be virtually excluded.

ACKNOWLEDGMENTS

This work was supported by the Russian Foundation for Basic Research, project no. 00-02-18004a.

REFERENCES

1. I. V. Volkov, S. T. Zavtrak, and I. S. Kuten, Phys. Rev. E **56**, 1097 (1997).
2. S. T. Zavtrak and I. V. Volkov, J. Acoust. Soc. Am. **102**, 204 (1997).
3. V. K. Kedrinskiĭ, V. A. Vshivkov, G. I. Dudnikova, and Yu. I. Shokin, Dokl. Akad. Nauk **361**, 41 (1998) [Dokl. Phys. **43**, 400 (1998)].
4. V. K. Kedrinskii, in *Fascination of Fluid Dynamics: A Symposium in Honour of Leen van Wijngaarden*, Ed. by A. Biesheuvel and G. F. van Heijst (Kluwer, Dordrecht, 1998), pp. 115–130, Reprint from Appl. Sci. Res. **58** (1/4) (1997–1998).

Translated by V. Chechin

Doklady Physics, Vol. 46, No. 12, 2001, pp. 860–863. Translated from Doklady Akademii Nauk, Vol. 381, No. 4, 2001, pp. 475–478.

ENERGETICS

Limiting Carnot Theorem for a Heat Engine Using Flow Energy

V. T. Volov

Presented by Academician A.I. Leont'ev January 23, 2001

Received January 24, 2001

There exists a wide class of heat engines that use flow energy (HEUFE) and do no mechanical work ($L_{\text{mech}} = 0$). The following systems belong to this class:

(i) chemical gas reactors of different types;

(ii) heat and mass gas exchangers (vortex tubes of different types, ejectors, mixers, gas acoustic devices, etc.);

(iii) gas energy devices (lasers and plasmatrons of different types, etc.).

The common property of this class of heat engines is that the energy of a gas flow is transformed into the potential energy of pressure (on the contrary, in rocket engines, for example, the total energy is transformed into kinetic energy). The higher the degree of the total flow energy transformation into the potential energy of pressure, the higher the efficiency of the device as a whole.

We now introduce the following notation:

$$\bar{k}_i = \frac{k_i}{k_1}, \quad \mu_{i(j)} = \frac{G_{i(j)}}{G_1}, \quad \Theta_i = \frac{T_i^*}{T_1^*},$$

$$\Theta_j = \frac{T^*_{\text{mix}\,j}}{T_1^*}, \quad \bar{C}_{P_{\text{mix}}} = \frac{C_{P_{\text{mix}}}}{C_{P_1}} = \frac{\sum_{j=1}^{n} \bar{C}_{P_j}\Theta_j\mu_j}{\sum_{j=1}^{n}\Theta_j\mu_j},$$

$$\bar{R}_{\text{mix}} = \frac{R_{\text{mix}}}{R_1} = \frac{\sum_{j=1}^{n} R_j\Theta_j\mu_j}{\sum_{j=1}^{n}\Theta_j\mu_j}, \quad R_{\text{mix}} = \frac{\sum_{j=1}^{n} R_j G_j}{\sum_{j=1}^{n} G_1},$$

$$\bar{W} = \frac{W}{C_{P_1} T_1^* G_1}, \quad k_1 = \frac{C_{P_1}}{C_{V_1}}, \quad \bar{R}_i = \frac{R_i}{R_1},$$

$$\bar{C}_{V_i} = \frac{C_{V_j}}{C_{V_1}}, \quad \bar{C}_{V_{\text{mix}}} = \frac{\sum_{j=1}^{n} \bar{C}_{V_j}\Theta_j\mu_j}{\sum_{j=1}^{n}\Theta_j\mu_j}.$$

where k_i, $i = 1, 2, \ldots, m$ is the adiabatic exponent; R_i, $i = 1, 2, \ldots, m$ is the gas constant related to the ith inlet of the working substance; R_{mix} is the gas constant of the mixture; T_i^*, $i = 1, 2, \ldots, m$ and $T^*_{\text{mix}\,j}$ are the total gas temperatures at the ith inlet and at the jth outlet, respectively; C_{P_i}, $i = 1, 2, \ldots, m$ and $C_{P_{\text{mix}}}$ are, respectively, the heat capacity (at constant pressure) of the gas at the ith inlet and the heat capacity (at constant pressure) of the mixture; G_i, $i = 1, 2, \ldots, m$ is the rate of the gas flow through the ith inlet; G_j, $j = 1, 2, \ldots, n$ is the rate of the gas flow through the jth outlet; $\lambda_{i(j)}$, $a_{\text{cri}(j)}$, and $V_{i(j)}$ are, respectively, the velocity coefficient, the critical velocity, and the gas velocity at the ith inlet and the jth outlet; W is the algebraic sum of the input heat powers for the HEUFE; and i_1^* and i_2^* are the enthalpies of the stopped flows at the inlet and outlet of the HEUFE.

Theorem. *The efficiency of a HEUFE cannot exceed a value*

$$\Delta N_{\max} = \frac{\sum_{i=1}^{m} \frac{k_1 - 1}{k_1}\mu_i\bar{R}_i\Theta_i\left(1 + \frac{\lambda_i^2}{k_i + 1}\right) + \bar{W}}{\sum_{i=1}^{m}\mu_i\bar{C}_{P_i}\Theta_i + \bar{W}} - \frac{k_1 - 1}{k_1}\frac{\bar{R}_{\text{mix}}}{\bar{C}_{P_{\text{mix}}}}.$$

Proof. The sum of the mechanical power and input heat power at all the inlets of a HEUFE is given by the expression [1]

$$N_{\text{in}} = \sum_{i=1}^{m}\left(\frac{P_i}{\rho_i} + \frac{v_i^2}{2}\right)G_i + W = \sum_{i=1}^{m} G_i R_i T_i^*$$

Samara Science Center, Department of Transport Problems, Russian Academy of Sciences, ul. Molodogvardeĭskaya 194, Samara, 443001 Russia

1028-3358/01/4612-0860$21.00 © 2001 MAIK "Nauka/Interperiodica"

$$\times\left[\left(1-\frac{k-1}{k+1}\lambda_i^2+\frac{k_i}{k_i+1}\lambda_i^2\right)\right]+W \quad (1)$$
$$=\sum_{i=1}^{m}G_iR_iT_i^*\left(1+\frac{\lambda_i^2}{k_i+1}\right)+W,$$

where P_i, ρ_i, and v_i are the static pressure, density, and velocity, respectively.

The total input power is determined by the formula

$$N_\Sigma=\sum_{i=1}^{m}G_ii_i^*+W=\sum_{i=1}^{m}C_{P_i}T_i^*G_i+W. \quad (2)$$

The total power of gas flows at all the outlets of the heat engine is

$$N_{\text{out}}=R_{\text{mix}}\sum_{j=1}^{n}T_j^*G_j\left(1+\frac{1}{k_j+1}\lambda_{\text{out}\,j}^2\right), \quad (3)$$

where $k_j=\dfrac{C_{P_j}}{C_{v_j}}$ is the adiabatic exponent at the jth outlet.

In the steady-state case of a heat engine doing no mechanical work ($L_{\text{mech}}=0$), the continuity and energy equations take the form

$$\sum_{i=1}^{m}G_i=\sum_{j=1}^{n}G_j,\ \sum_{i=1}^{m}C_{P_i}T_i^*G_i+W=C_{P_{\text{mix}}}\sum_{j=1}^{n}T_{\text{mix}\,j}^*G_{\text{mix}\,j}.$$

Rewriting these equations in a dimensionless form, we have

$$1+\sum_{i=2}^{m}\mu_i=\sum_{j=1}^{n}\mu_j,$$
$$1+\sum_{i=2}^{m}\bar{C}_{P_i}\Theta_i\mu_i+\bar{W}=\bar{C}_{P_{\text{mix}}}\sum_{j=1}^{n}\Theta_{\text{mix}}\mu_j. \quad (4)$$

To determine the relative fraction of the power lost or utilized in a HEUFE, we subtract Eq. (3) from Eq. (1) and divide the difference obtained by expression (2). As a result, we have

$$\Delta\bar{N}=\frac{N_{\text{in}}-N_{\text{out}}}{N_\Sigma}=\frac{k_1-1}{k_1}\frac{\sum_{i=1}^{m}\mu_i\bar{R}_i\Theta_i\left(1+\frac{\lambda_i^2}{k_j+1}\right)+\bar{W}\frac{k_1}{k_1-1}-\bar{R}_{\text{mix}}\sum_{j=1}^{n}\Theta_j\mu_j\left(1+\frac{\lambda_{\text{out}\,j}^2}{k_j+1}\right)}{\sum_{i=1}^{m}\bar{C}_{P_i}\Theta_i\mu_i+\bar{W}}. \quad (5)$$

Let us find the limit of expression (5) as $\lambda_{\text{out}\,j}\longrightarrow 0$ in the case of finite flow rates where $G>0$ (this corresponds to an infinitely large broadening of the diffuser). After transformations, Eq. (5) takes the form

$$\Delta\bar{N}_{\max}=\lim_{\lambda_{\text{out}\,j}\to 0}\Delta\bar{N}=\left(\frac{\sum_{i=1}^{m}\mu_i\bar{R}_i\Theta_i\left(1+\frac{\lambda_i^2}{k_i+1}\right)+\bar{W}\frac{k_1}{k_1-1}-\bar{R}_{\text{mix}}\sum_{j=1}^{n}\Theta_j\mu_j}{\sum_{i=1}^{m}\bar{C}_{P_i}\Theta_i\mu_i+\bar{W}}\right)\frac{k_1-1}{k_1}. \quad (6)$$

With regard to (4), Eq. (6) can be written out as

$$\Delta\bar{N}_{\max}=\lim_{\lambda_{\text{out}\,j}\to 0}\Delta\bar{N}=\frac{\sum_{i=1}^{m}\mu_i\bar{R}_i\Theta_i\left(1+\frac{\lambda_i^2}{k_i+1}\right)\frac{k_1-1}{k_1}+\bar{W}-\frac{\bar{R}_{\text{mix}}}{\bar{C}_{P_{\text{mix}}}}\left[\sum_{i=1}^{m}\bar{C}_{P_i}\Theta_i\mu_i+\bar{W}\right]\frac{k_1-1}{k_1}}{\sum_{i=1}^{m}\bar{C}_{P_i}\Theta_i\mu_i+\bar{W}}$$
$$=\frac{\sum_{i=1}^{m}\mu_i\bar{R}_i\Theta_i\left(1+\frac{\lambda_i^2}{k_i+1}\right)\frac{k_1-1}{k_1}+\bar{W}}{\sum_{i=1}^{m}\bar{C}_{P_i}\Theta_i\mu_i+\bar{W}}-\frac{\bar{R}_{\text{mix}}}{\bar{C}_{P_{\text{mix}}}}\frac{k_1-1}{k_1}. \quad (7)$$

Hence, the efficiency of a HEUFE has the form

$$\eta_{G>0} = \overline{W}_{\text{rel}}^{\text{tot}} \Delta \overline{N}_{\max}, \tag{8}$$

where $\overline{W}_{\text{rel}}^{\text{tot}} = \dfrac{W_{\text{tot}}}{\Delta N_{\max}}$ is the relative useful power obtained in the engine.

The maximum efficiency of a HEUFE is

$$\eta_{G>0}^{\max} = \Delta \overline{N}_{\max}. \tag{9}$$

Expression (7) represents the maximum value of the relative fraction of the total power (i.e., the sum of the flow power and input heat power) lost and (or) utilized in a HEUFE.

Since both the output gas velocities and heat loss are nonvanishing, the efficiency of an actual HEUFE is always lower than the limiting value (7):

$$\eta < \eta_{\max}^{\text{ideal}}.$$

The theorem is proved. Thus, we obtained an upper estimate for the efficiency of a HEUFE under $L_{\text{mech}} = 0$.

Corollary 1. *In a heat engine, the global maximum for the lost and* (*or*) *utilized sum of mechanical power of the compressible medium and input heat power is*

$$\lim_{\substack{\lambda_{\text{out}} \to 0 \\ \lambda_i \to \lambda_{\max}}} \Delta \overline{N} = \frac{\sum_{i=1}^{m} \mu_i \overline{R}_i \Theta_i \dfrac{k_i}{k_i - 1} \dfrac{k_1 - 1}{k_1} + \overline{W}}{\sum_{i=1}^{m} \overline{C}_{P_i} \Theta_i \mu_i + \overline{W}} - \frac{k_1 - 1}{k_1} \frac{\overline{R}_{\text{mix}}}{\overline{C}_{P_{\text{mix}}}}. \tag{10}$$

If the temperatures and flow rates for identical gases at the mth inlets are equal to each other, expression (8) takes the simple form

$$\Delta \overline{N}_{\max} = \frac{1}{k}, \quad k = \frac{C_P}{C_V}.$$

For example, if air is used as a working substance ($k = 1.4$), the absolute maximum of lost and utilized power in the engine is approximately equal to 70%. The remaining 30% of the mechanical power is spent for the medium transport.

For a HEUFE of continuous action, expression (7) will have the same value for identical gases at the mth inlets if the input heat power $\overline{W}$ is infinitely large:

$$\lim_{\overline{W} \to \infty} \Delta \overline{N}_{\max} = 1 - \frac{k-1}{k} = \frac{1}{k}.$$

In the case of a homogeneous gas mixture [one inlet ($i = 1$) and one outlet ($j = 1$)], expression (7) takes the form:

$$\Delta \overline{N}_{\max} = \frac{\dfrac{1}{k}\dfrac{k-1}{k+1}\lambda_1^2 + \dfrac{\overline{W}}{k}}{1 + \overline{W}}. \tag{11}$$

If the heat powers vanish ($\overline{W} = 0$), expression (11) is simplified to

$$\Delta \overline{N}_{\max} = \frac{1}{k}\frac{k-1}{k+1}\lambda_1^2. \tag{11a}$$

According to the energy equation, the flow stagnation temperature remains constant in this case ($T^* = \text{const}$). For an ideal adiabatic nozzle, the ratio of the expansion work to the total gas enthalpy is the Carnot efficiency:

$$\eta_{\text{Carnot}} = 1 - \frac{T_1}{T_1^*} = \frac{k-1}{k+1}\lambda_1^2.$$

Hence, taking into account formulas (8) and (11a), we find the relation between the efficiency of an ideal HEUFE ($\bar{L}_{\text{mech}} = 0$) and the Carnot efficiency:

$$\eta_{G>0}^{\text{ideal}} = \frac{1}{k}\eta_{\text{Carnot}}^{\text{ideal}}. \tag{12}$$

Corollary 2. The efficiency of an ideal adiabatic HEUFE ($\overline{W} = 0$; $\bar{L}_{\text{mech}} \neq 0$) cannot exceed the efficiency of the Carnot ideal heat engine:

$$\eta_{G>0} = \frac{i_1^* - i_2^*}{i_1^*} = 1 - \frac{T_2^*}{T_1^*}, \quad T_1 = T_1^*, \quad T_2^* = \frac{T_2}{1 - \dfrac{k-1}{k+1}\lambda_2^2}. \tag{13}$$

Allowing for only the first term in the expansion of expression (8) into the Taylor series, we have

$$\eta_{G>0} = 1 - \frac{T_2}{T_1\left(1 - \dfrac{k-1}{k+1}\lambda_2^2\right)} \approx 1 - \frac{T_2}{T_1} - \frac{k-1}{k+1}\lambda_2^2\frac{T_2}{T_1}.$$

Since the velocity of exhaust gases at the outlets is finite, even if maximum utilization of the mechanical energy of the gas flow takes place, the efficiency of the ideal HEUFE is lower than that of an ideal Carnot heat engine:

$$\eta_{G>0}^{\text{ideal}} = \eta_{\text{Carnot}} - \varepsilon,$$

where

$$\varepsilon = \frac{k-1}{k+1}\lambda_2^2\frac{T_2}{T_1} > 0, \text{ i.e. } \eta_{G>0}^{\text{ideal}} < \eta_{\text{Carnot}}^{\text{ideal}}.$$

The classification of heat engines according to the methods of transforming the total energy is shown in

Heat engine classification according to the methods of transforming the total energy of the working substance

Parameter	I	II	III
Flow rate of a gaseous working substance	$G = 0$	$G > 0$ ($G \longrightarrow G_{max}$)	$G > 0$ ($G \longrightarrow G_{max}$)
Output gas velocity	$v_{out} \approx 0$	$v_{out} > 0$ ($v_{out} \longrightarrow v_{max}$)	$v_{out} \longrightarrow 0$ ($S_{out} \longrightarrow \infty$)
Transformation of the gas-flow total energy	Total (internal) energy is transformed into mechanical work $E_{tot} = E_{int} \longleftrightarrow A_{mech}$	Total energy is transformed into kinetic energy $E_{tot} \longrightarrow E_{kin}$	Total energy is transformed into potential energy of pressure $E_{tot} \rightarrow E_{pot}$
Efficiency	$\eta_{Carnot}^{ideal} = 1 - \frac{T_2}{T_1}$ $\eta_{Stirling}$ etc.	$\eta = 1 - \left(\frac{P_a}{P_1}\right)^{\frac{n-1}{n}}$ $\lim_{P_1 \to \infty} \eta \longrightarrow \eta_{Carnot}^{ideal}$	(a) $L_{mech} = 0$ $\eta_{G>0}^{ideal} = \frac{1}{k}\eta_{Carnot}^{ideal}$ (b) $Q_{ext} = 0$, $L_{tech} \neq 0$ $\eta^{ideal} = \eta_{Carnot}^{ideal} - \varepsilon$
Cycle describing the heat engine	Carnot cycle Stirling cycle	Brayton cycle	HEUFE cycle

the table. In the heat engines described in column I, the total energy is transformed into mechanical energy, with the gas flow rate vanishing ($G = 0$) and the gas flow velocity being very low ($W \simeq 0$, static and quasi-static cases). This class of heat engines is characterized by a Carnot cycle and by Carnot efficiency. In the heat engines of column II (rocket engines, air jet engines, etc.), the total energy is transformed into kinetic energy. In this case, the output gas flow velocity tends towards its maximum value ($v_{out} \longrightarrow v_{max}$, $G > 0$). For such engines, the efficiency and cycle correspond to Carnot efficiency and the Brayton cycle, respectively.

The class of heat engines considered in this study is presented in column III. In this case, the total energy of the gas flow is transformed into the potential energy of pressure; i.e., $E_{tot} \longrightarrow E_{pres}$ ($G > 0$, the output gas velocity tends toward zero, $v_{out} \longrightarrow 0$). The efficiency of such devices doing no mechanical work ($L_{mech} = 0$) is less than that of an ideal Carnot heat engine by the factor k.

This fact indicates that the efficiency of the ideal heat engine under consideration depends on properties of the working substance $\left(\frac{C_P}{C_v} = k\right)$. On the contrary, the efficiency of an ideal Carnot heat engine is independent of properties of the working substance. This class of heat engines is described by a heat cycle, which is, in general, opposite to that in rocket engines and air jet engines. The latter involves gas compression in a compressor, flow expansion in a nozzle, the input or output of heat into a working chamber, expansion in a confuser, and compression in a diffuser.

ACKNOWLEDGMENTS

The author is grateful to G.N. Abramovich†, A.P. Merkulov† for their support of this study.

The author also is grateful to Yu.M. Dubinkin, Yu.L. Ratis, A.Ya. Cherkez, and V.G. Shakhov for their participation in discussions and valuable comments.

REFERENCES

1. G. N. Abramovich, *Applied Gas Dynamics* (Nauka, Moscow, 1983).

† Deceased.

Translated by Yu. Vishnyakov

Doklady Physics, Vol. 46, No. 12, 2001, pp. 864–868. Translated from Doklady Akademii Nauk, Vol. 381, No. 6, 2001, pp. 777–781.

ENERGETICS

An Effect of Thermodynamic-Parameter Pulsations on the Condensation–Relaxation Process in a Supersaturated Vapor

N. M. Kortsenshteĭn and E. V. Samuĭlov

Presented by Academician A.I. Leont'ev June 5, 2001

Received June 6, 2001

We consider the volume condensation of vapor from a vapor–gas mixture after a sudden formation of the supersaturated state. Thermodynamic parameters of the mixture are assumed to undergo perturbation with a small amplitude of pulsations with respect to average values. On the basis of numerical simulation, it was revealed that for a pulsation frequency exceeding a certain minimum value, the effect of the pulsations is determined only by amplitude and is independent of frequency and phase. For this frequency region, we found expressions determining the relative decrease in the condensation-relaxation time and the relative increase in the droplet-number density. The upper and lower boundaries for the field of application of the dependences found was determined with respect to the pulsation frequency.

1. Let the mixture of an unsaturated vapor and a noncondensing gas be in an adiabatically insulated cylinder with a mobile piston (the piston is fixed). A rapid displacement of the piston makes it possible for the gas to expand and to pass from a stable unsaturated state into a metastable supersaturated state. Then we fix the piston in a new position. In the supersaturated vapor, the relaxation to the equilibrium state takes place as in an arbitrary metastable system. In the case under consideration, this is condensation relaxation involving the processes of nucleation (formation of viable nuclei of a new phase) and growth of the droplets formed. The metastable state of the supersaturated vapor is characterized by a degree of supersaturation

$$s = \frac{p_v}{p_s(T)}, \quad (1)$$

where p_v is the partial vapor pressure and $p_s(T)$ is the saturation pressure above a flat liquid–vapor interface depending only on temperature. As a condensation–relaxation time τ_c, we imply an interval of time during which an initial degree of supersaturation s_0 caused by the vapor expansion decreases by a factor of e. For determining τ_c and other characteristics of the condensation–relaxation process, we used the kinetic equation for the droplet-size distribution function [1]:

$$\frac{\partial f}{\partial t} + \frac{\partial (f\dot{r})}{\partial r} = \frac{I}{\rho}\delta(r - r_{cr}). \quad (2)$$

To solve this equation, the moments method is used. Provided that the radius r of nucleating and growing droplets is much smaller than the mean free path λ for vapor molecules (this condition is assumed to be fulfilled), the moments method makes it possible to reduce equation (2) to the set of moment equations [1]

$$\frac{d\Omega_i}{dt} = i\dot{r}\Omega_{i-1} + \frac{I}{\rho}r_{cr}^i, \quad i = 0, 1, 2, 3, \quad (3)$$

where

$$\Omega_i = \int_{r_{cr}}^{\infty} r^i f(r)dr$$

is the distribution-function moment of the ith order. Here, $f(r)$ is the droplet-size distribution function normalized to the number of droplets per unit mass of the vapor–gas–droplet mixture, I is the nucleation rate determining the number of nuclei of the critical size r_{cr} formed per unit time and per unit volume, $\dot{r}$ is the droplet-growth rate, and ρ is the density of the vapor–gas–droplet mixture. The system of equations (3) supplemented by the equation of state and conservation laws for mass and energy composes a mathematical model of the condensation–relaxation process used in this study. Apart from the above relationship $r \ll \lambda$, we also assume that the following conditions are met:

$$\tau_c \gg \tau_g, \quad \tau_c \gg \tau_{lag},$$

AO Power Engineering Institute,
Leninskiĭ pr. 19, Moscow, 117927 Russia

1028-3358/01/4612-0864$21.00

where τ_g is the time of vapor expansion and τ_{lag} is the time lag in the nucleation theory determined as the time of establishing the equilibrium size distribution for new-phase nuclei. The former condition makes it possible to consider the process of the transition of vapor into the metastable state as reasonably fast and to omit processes accompanying the vapor expansion. The latter condition makes it possible to calculate the nucleation rate and the droplet-growth rate in a quasi-steady approximation. The model of the condensation–relaxation process based on the system of equations (3) makes it possible to determine the time dependence of such quantities as the droplet-number density $n_d = \rho\Omega_0$, their average radius $r_d = \frac{\Omega_1}{\Omega_0}$, the degree of condensation $\xi = \frac{4}{3}\frac{\pi\rho_l\Omega_3}{c_v^0}$ (ρ_l is the density of condensate, and c_v^0 is the vapor mass concentration at the initial time moment), and also pressure, temperature, the degree of supersaturation and, thus, the condensation–relaxation time. Analysis of our results for the mathematical simulation of the condensation–relaxation process has shown that, at the initial moment of time, the quantities τ_c and n_d are the power function of the nucleation rate:

$$\tau_c^0 \backsim I_0^{-1/4}, \quad n_c^0 \backsim I_0^{3/4}.$$

Similar dependences were obtained in [3] when considering the relaxation processes in glasses. In this study, for calculating the steady-state nucleation rate, we used the expression from the classical Zel'dovich–Frenkel' theory [2]. With allowance for this fact, we can write out the explicit expressions for τ_c and n_d as functions of the initial degree of supersaturation:

$$\tau_c \backsim \exp\left\{\frac{A}{[\ln s_0]^2}\right\}, \tag{4}$$

$$n_c \backsim \exp\left\{-\frac{3A}{[\ln s_0]^2}\right\}, \tag{5}$$

where A is the constant. As it must be, with approaching the stability region ($s_0 \longrightarrow 1$), the condensation-relaxation time tends to infinity, while the droplet-number density tends to zero.

2. The thermodynamic parameters of the system under consideration are assumed to undergo perturbations during the condensation relaxation. We consider perturbations of all the parameters to be related by the Poisson adiabatic equation. Therefore, we consider furthermore only the perturbations of temperature, nevertheless taking into account the perturbations of all thermodynamic parameters. We now analyze how these perturbations affect the condensation–relaxation process.

In the case of perturbations (pulsations with respect to an average value), the temperature can be represented in the form

$$T = \langle T\rangle(1 + \vartheta), \tag{6}$$

where $\langle T\rangle$ is the averaged temperature, T' is the pulsation component, and $\vartheta \equiv \frac{T'}{\langle T\rangle}$ is the relative pulsation. In this case, the degree of supersaturation according to (1) with allowance for the temperature dependence of the saturated-vapor pressure $p_s \backsim \exp\left(\frac{L}{[RT]}\right)$ and a smallness of pulsations ($\vartheta \ll 1$) can be transformed into the form

$$\ln s = \ln s(\langle T\rangle) - \vartheta\left(\frac{L}{R\langle T\rangle} - \frac{\gamma}{\gamma - 1}\right). \tag{7}$$

Here, $s(\langle T\rangle)$ is the degree of supersaturation at the averaged temperature, L is the evaporation heat, R is the universal gas constant, and γ is the adiabatic index. In our study, we consider perturbations of thermodynamic parameters in the form of harmonic pulsations

$$\vartheta = \vartheta_0 \sin(2\pi\nu t + \varphi_0). \tag{8}$$

Expressions (6)–(8) were used for the calculation of values entering into Eqs. (3). When simulating on the basis of Eqs. (3), we were able to clarify the effect of the initial degree of supersaturation s_0 and also the amplitude ϑ_0, the frequency ν, and the initial pulsation phase φ_0 on the condensation–relaxation process. The typical time dependences for the degree of supersaturation and for the droplet-number density are shown in Fig. 1. The data were obtained from the results of solving the set of equations (3) for the cesium–argon mixture (the volume ratio is 1 : 7) for $s_0 = 6$, $\vartheta_0 = 1\%$, $\nu = 100$ Hz, and $\varphi_0 = 0$. In the same figure, we show similar results obtained for the case of ignoring pulsations. As is seen, in the presence of pulsations, the condensation–relaxation time decreases, while the droplet-number density increases compared to the case without pulsations. It should be noted that the curve for the $n_d(t)$ dependence traces pulsations of the degree of supersaturation. This curve abruptly increases with the degree of supersaturation and attains a plateau with its decrease compared to the value at the averaged temperature. Similar calculations were carried out within a reasonably wide interval of variation of pulsation characteristics of the condensation process: $\vartheta_0 = 0.05$–5%, $\nu = 10^{-1}$–10^4 Hz, and $\varphi_0 = -\pi - \pi$. In this case, s_0 varied from 3 to 6. Such an interval of variation for all indi-

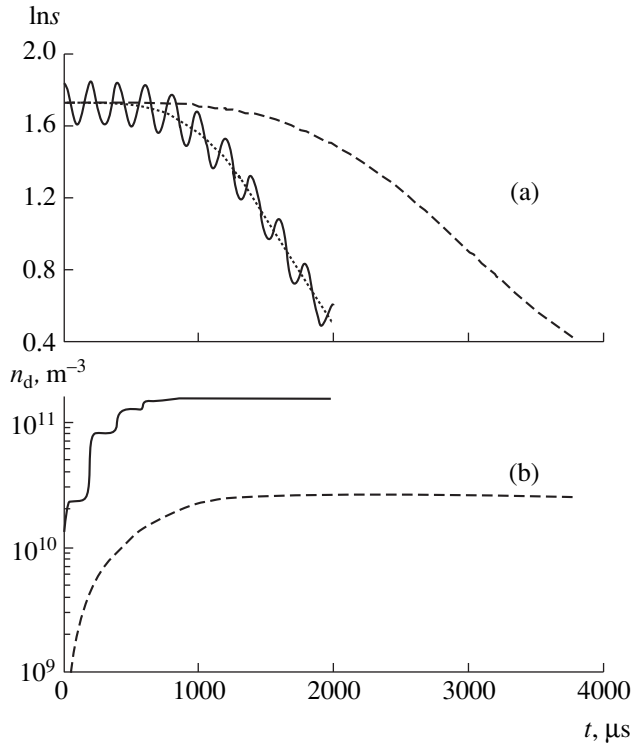

Fig. 1. (a) Degree of supersaturation and (b) droplet-number density as functions of time with (solid line) and without (dashed line) allowance for pulsations of thermodynamic parameters. The dotted line is the degree of supersaturation at the averaged temperature.

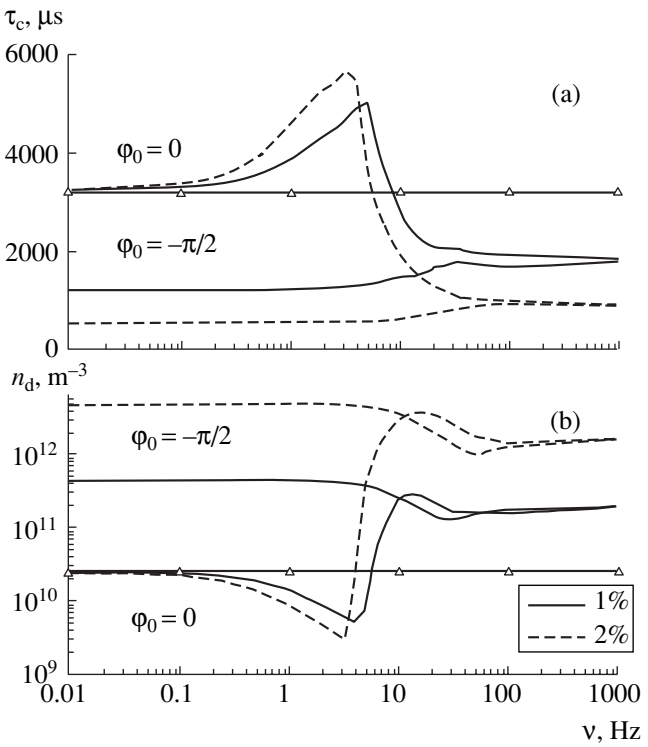

Fig. 2. (a) Condensation-relaxation time and (b) droplet-number density as functions of pulsation frequency for various pulsation amplitudes and phases. Triangles mark the data obtained without regard for pulsations.

cated quantities enabled us to envelop five decimal orders of variation in the condensation–relaxation time (10^{-4}–10 s) and 15 decimal orders of variation in the droplet-number density (10^{-1}–10^{14} m^{-3}). Certain results of calculations shown in Fig. 2 make it possible to draw further qualitative conclusions about the effect of pulsations on the condensation–relaxation process. It should be noted that for each value of the pulsation amplitude there exists such a minimum frequency ν_{min} above which the process under consideration is independent of both the frequency and the initial phase of pulsations. It can be seen that ν_{min} increases with ϑ_0. At the same time, according to the results of the calculations performed, the product $\nu_{min}\tau_c$ varies insignificantly (within the factor 2 to 4) for the entire spectrum of ϑ_0 and s_0 values. Consequently, ν_{min} can be determined from the relationship

$$\nu_{min} = \frac{4}{\tau_c}. \quad (9)$$

Taking into account that ν^{-1} is the pulsation period, in accordance with relation (9), the physical meaning of the quantity ν_{min} is the following: during the condensation–relaxation time, four or more pulsations are sufficient for the system to forget the initial phase of oscillations of thermodynamic parameters. From this standpoint, the resonance-like maxima of τ_c and minima of n_d, which are observed in Fig. 2 for $\nu \le \nu_{min}$, are likely associated with the coincidence of the pulsation period and the condensation–relaxation time. A weak dependence of τ_c and n_d on ν for even lower values of the frequency (Fig. 2) corresponds to the process of condensation relaxation for slowly varying (for the time τ_c) conditions. These are either elevated (for $\varphi_0 = -\pi/2$) or reduced (for $\varphi_0 = 0$) values of the degree of supersaturation compared to s_0, which manifests itself in the dependence of the quantities τ_c and n_d on φ_0.

3. Further investigation was focused in the region

$$\nu_{min} < \nu < \nu_{max} \quad (10)$$

in which the effect of pulsations on the condensation–relaxation process depends only on their amplitude and increases with its growth. The value of ν_{min} was determined according to relation (9). As an upper boundary of the frequency interval under consideration, it was natural to choose the value

$$\nu_{max} = \frac{1}{\tau_{lag}}. \quad (11)$$

We analyzed the results of simulating the condensation–relaxation process for various values of s_0 and ϑ_0. These results are shown in Fig. 3. The quantities τ_c and n_d are seen to be well described by the dependences of the form

$$\tau_c = A_\tau(\vartheta_0)\exp\left\{\frac{B_\tau(\vartheta_0)}{[\ln s_0]^2}\right\},$$

$$n_d = A_n(\vartheta_0)\exp\left\{-\frac{B_n(\vartheta_0)}{[\ln s_0]^2}\right\}.$$

The method of analyzing the calculation results involves the following. For each value of ϑ_0, we determined the values log$A$ and B. The values obtained were approximated by polynomials in powers of ϑ_0. The use of a second-order polynomial for ln$A$ and of a third-order polynomial for B enabled us to reproduce reasonably well the results of calculations (solid lines in Fig. 3). The terms of the zeroth order in the expansions obtained coincided with the values obtained previously in the simulations of the condensation–relaxation process without pulsations taken into account in expressions (4) and (5). This allowed us to obtain in a compact form the expressions determining the effect of thermodynamic-parameter pulsations on the condensation–relaxation process restricting the expansions by both the zero order for ln$A$ and the first order for B:

$$\frac{\tau_c^0}{\tau_c} = 1.06\exp\left\{\frac{2.15\vartheta_0}{[\ln s_0]^2}\right\}, \quad (12)$$

$$\frac{n_d}{n_d^0} = 0.88\exp\left\{\frac{6.5\vartheta_0}{[\ln s_0]^2}\right\}. \quad (13)$$

Here, the superscript 0 marks the quantities calculated from relationships (4) and (5) without allowance for pulsations. It is natural that the ratios $\frac{\tau_c^0}{\tau_c}$ and $\frac{n_d}{n_d^0}$ must be equal to 1 for $\vartheta_0 = 0$. In the expressions obtained, this passage to the limit is fulfilled only approximately, using simplified approximations for ln$A$ and B. The relationship

$$\frac{\tau_c^0}{\tau_c} = \left(\frac{n_d}{n_d^0}\right)^{1/3},$$

which follows from (12) and (13) as approximate, is satisfied to a high accuracy in the processing of the primary calculation data. As follows from the obtained expressions (12) and (13) and from the data shown in Fig. 3, the effect of pulsations on the condensation relaxation increases with the decrease in the degree of the vapor supersaturation. On the other hand, the dependence of final results for the condensation–relaxation process (τ_c, n_d) on the initial degree of supersaturation is weakened with the growth of the pulsation amplitude. The field of application of formulas (12)

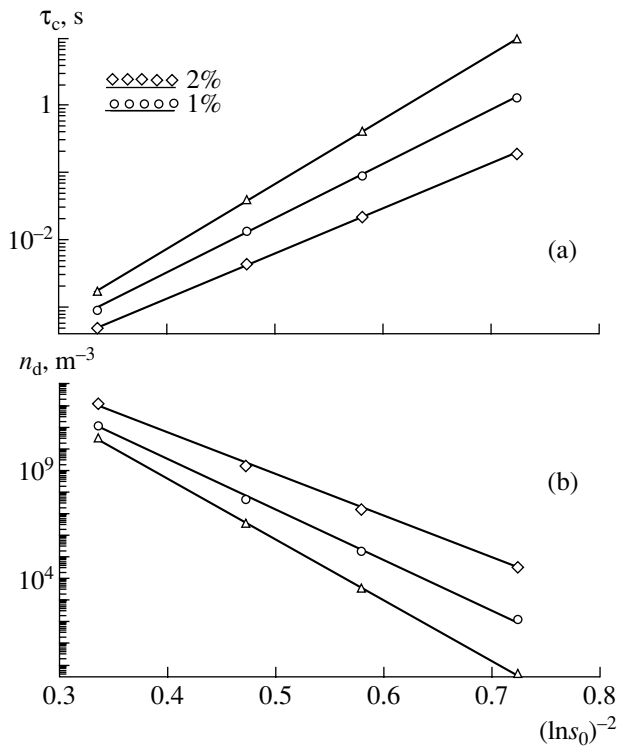

Fig. 3. (a) Condensation-relaxation time and (b) droplet-number density as functions of the initial degree of supersaturation for various pulsation amplitudes. Triangles mark the data obtained without regard for pulsations.

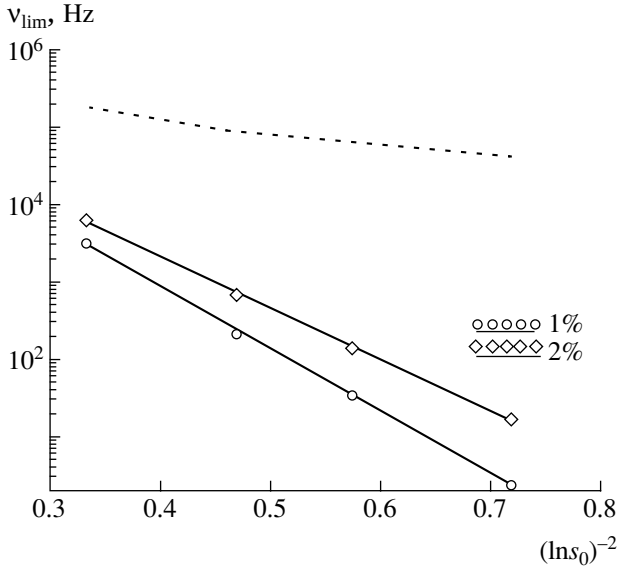

Fig. 4. Upper (dashed line) and lower (solid lines) ultimate frequencies as functions of the degree of supersaturation for various pulsation amplitudes.

and (13), which is determined by relations (9)–(11), extends with increasing initial degree of supersaturation and decreasing pulsation amplitude (Fig. 4). For the entire spectrum of the input calculation parameters under consideration, the variation interval at the lower boundary (ν_{min}) attained five orders of magnitude (from tenths of a hertz to tens of kilohertz. The frequencies corresponding to the upper boundary (ν_{max}) were found within one order of magnitude at the level of 100 kHz.

In conclusion, we should present the following arguments. Along with the effect of pulsations of medium parameters on the process of vapor condensation, an inverse effect is also possible. Both phenomena were investigated in detail by M.E. Deĭch with coworkers (see [4, 5] and relevant references).

REFERENCES

1. L. E. Sterin, *Foundations of Gas Dynamics for Two-Phase Flows in Nozzles* (Énergiya, Moscow, 1972).
2. D. Kashchiev, *Nucleation: Basic Theory with Applications* (Butterworth Heinemann, Oxford, 2000).
3. V. V. Slezov and Yu. Schmeltser, Fiz. Tverd. Tela (St. Petersburg) **39**, 2210 (1997) [Phys. Solid State **39**, 1971 (1997)].
4. M. E. Deĭch and G. A. Filippov, *Gas Dynamics of Two-Phase Media* (Énergoizdat, Moscow, 1981).
5. M. E. Deĭch, *Gas Dynamics of Turbomachine Grids* (Énergoatomizdat, Moscow, 1996).

Translated by V. Bukhanov

Doklady Physics, Vol. 46, No. 12, 2001, pp. 869–872. Translated from Doklady Akademii Nauk, Vol. 381, No. 4, 2001, pp. 479–483.

MECHANICS

Nonlocal Modulation Equations for Viscous-Fluid Flows in Layers and Spatially Localized Perturbations

A. Afendikov* and A. Mielke**

Presented by Academician V.P. Myasnikov May 17, 2001

INTRODUCTION

For a variety of hydrodynamic problems, it is physically reasonable to analyze them in unbounded two-dimensional (2D) and three-dimensional (3D) cylindrical domains [1–7]. However, the standard setting of the initial and boundary value problems in the form of Navier–Stokes equations is insufficiently determinate in this case. As additional conditions at infinity, the mean flux $\mathcal{F}$ or the mean gradient $\mathcal{P}$ of pressure in the directions of the cylinder generatrix can be proposed. As an example, we consider the 3D Poiseuille problem of a viscous incompressible flow between parallel plates. In solving this problem, the Davey–Hocking–Stewartson (DHS) modulation system [8] turns out to be the generalization of the one-dimensional complex Ginzburg–Landau equation that describes 2D problems of the Poiseuille flow near the stability threshold. We complement the DHS system by different sets of nonlocal conditions. Thereby, we are able to find correct constrains to the DHS system for problems with one unbounded variable. It turns out to be possible to set a problem for which there exist solutions localized over the variable transverse to the mainstream direction. These solutions are the principal terms in the expansions for the corresponding exact solutions to the system of Navier–Stokes equations.

1. MULTIPARAMETER EXPANSIONS

Starting from the 1960s, formal multiparameter asymptotic expansions were used by F. Busse, A. Newell, T. Stuart, W. Eckhaus, and others to derive modulation equations of the Ginzburg–Landau type. In [8], this approach was extended to problems of layered flows of viscous fluids, e.g., for the Poiseuille flow $V_{\mathrm{Pois}}(t, x, y) = (1 - y^2, 0, 0)^t$ between two parallel walls. In this case, the motion of a fluid occurs in the domain $\Omega = \mathbb{R}^2 \times (-1, 1)$ with the coordinates x_1, x_2, y, [where $(x_1, x_2) \in \mathbb{R}^2$], whereas the pressure gradient drives the entire system; i.e., $p(x, y) = -\frac{2}{\mathrm{R}}x_1$. Here, we use dimensionless variables. The velocity $v(t, x, y) \in \mathbb{R}^3$ has components v_1, v_2 and v_3 along the directions x_1, x_2 and y, which satisfy the problem

$$\left.\begin{aligned} \partial_t v + (v \cdot \nabla) v + \nabla p - \frac{1}{\mathrm{R}}\Delta v &= 0 \\ \operatorname{div} v &= 0 \end{aligned}\right\} \text{ in } \Omega \qquad (1)$$

$$\text{and } v = 0 \text{ on } \partial\Omega,$$

where p is pressure and R is the Reynolds number corresponding to a certain typical velocity. We now define

$$[\![f]\!] = \lim_{L \to \infty} \frac{1}{8L^2} \int_{-L}^{L}\int_{-L}^{L}\int_{-1}^{1} f(x_1, x_2, y)\,dx_1 dx_2 dy.$$

Then the basic steady-state one-dimensional flow is uniquely determined if, for example, we suppose that $[\![\partial_{x_1} p]\!] = -\frac{2}{\mathrm{R}}$ and $[\![v_2]\!] = 0$ (see [2]). These conditions correspond to the constant mean pressure gradient and the zero mean flux (in streamwise and spanwise directions with respect to the basic flow, respectively). We term this Poiseuille problem as $\mathcal{P}\mathcal{F}$. The next problem with $[\![v_1]\!] = \frac{4}{3}$ and $[\![v_2]\!] = 0$ deals with a fixed mean flux along each direction, and we call this problem $\mathcal{F}\mathcal{F}$. Below, for brevity, we use the notation $(1)_{\mathcal{P}\mathcal{F}}$ and $(1)_{\mathcal{F}\mathcal{F}}$. Our next goal is deriving adequate amplitude equations for these two different cases. Of course, two other cases with constant mean pressure gradients in both directions, i.e., $[\![\partial_{x_1} p]\!] = -\frac{2}{\mathrm{R}}$ and $[\![\partial_{x_2} p]\!] = 0$ or $[\![v_1]\!] = \frac{4}{3}$ and $[\![\partial_{x_2} p]\!] = 0$, can be analyzed in a similar way. We denote the last two problems as $\mathcal{P}\mathcal{P}$ and $\mathcal{F}\mathcal{P}$, respectively.

* *Keldysh Institute of Applied Mathematics, Russian Academy of Sciences, Miusskaya pl. 4, Moscow, 125047 Russia*
E-mail: andre@spp.keldysh.ru

** *Mathematical Institute A, Stuttgart University, Pfaffenwaldring 57, Stuttgart, Germany*
E-mail: mielke@mathematik.uni-stuttgart.de

1028-3358/01/4612-0869$21.00

We are interested in small perturbations of the basic Poiseuille flow, i.e., $u = v - V_{\text{Pois}}$. Since V_{Pois} is independent of $x \in \mathbb{R}^2$, the classical representation is

$$u(t, x, y) = e^{\lambda t + i\langle k, x\rangle}\Phi_k(y),$$

where $k = (\alpha, \beta)$ can be employed for linearizing problem (1) in the case of the Poiseuille flow. Using numerical information together with the Squire transformation (see, e.g., [2, 8]) shows that for $\alpha \in (\alpha_4, \alpha_1)$, where $\alpha_4 \approx 0.98787$ and $\alpha_1 \approx 1.0973$, the instability threshold $R = R_{cr}(\alpha)$ occurs for the wave vector $k = (\alpha, 0)$, which is parallel to the basic flow. The minimal critical Reynolds number is $R_0 \approx 5772.222$, and the corresponding wave vector is $k_0 = (\alpha_2, 0)^t$, where $\alpha_2 \approx 1.02055$. The expansion coefficients

$$\lambda(R - R_0, k - k_0) = i\alpha_2 c_0 + \lambda_{0,1}(R - R_0) - i\langle c_{\text{gr}}, k - k_0\rangle - \langle \Lambda(k - k_0), k - k_0\rangle + \text{h. o. t.}$$

can be found numerically: $c_0 \approx 0.2640$, $\lambda_{0,1} \approx (0.1682 + i0.8113) \times 10^{-5}$, $c_{\text{gr}} \approx (0.3831, 0)^t$, $\Lambda = \text{diag}(\Lambda_{11}, \Lambda_{22}) \approx \text{diag}(0.187 + i0.0275,\ 0.004663 + i0.08083)$. These values refine the results of [8]. The corresponding eigenfunction can be expressed in terms of the eigenfunction $\varphi\colon (-1, 1) \longrightarrow \mathbb{C}$ of the Orr–Sommerfeld equation as $\Phi_{k_0}(y) = \left(\frac{d}{dy}\varphi(y), 0, -i\alpha_2\varphi(y)\right)^t$ (see [2]).

In order to preserve the normalization suggested in [8], we assume that $R = R_0 + \rho\varepsilon^2$ with $\rho = \frac{1}{\text{Re}(\lambda_{0,1})}$ and denote $(\xi_1, \xi_2) = \varepsilon(x - c_{\text{gr}}t)$. Then the multiscale expansion near the stability threshold for the solutions to problem (1) takes the form

$$u(t, x, y) = \varepsilon A(\varepsilon^2 t, \xi)E(t, x)\Phi_{k_0}(y) + \text{c. c} + \text{h. o. t.},$$

$$p(t, x, y) = p_0(t) - \frac{2x_1}{R} + \varepsilon P(\varepsilon^2 t, \xi) + \text{h. o. t.},$$

where $E(t, x) = e^{i(\omega t + \langle k_0, x\rangle)}$. Equating to zero the corresponding coefficients ahead of $\varepsilon^j E^m$, we arrive at the DHS system

$$\begin{gathered}\partial_r A - \Lambda_{11}\partial_{\xi_1}^2 A - \Lambda_{22}\partial_{\xi_2}^2 A - \mu A - c_1|A|^2 A - c_2 A\partial_{\xi_1} P = 0,\\ \text{div}_\xi(\nabla_\xi P + \gamma(|A|^2, 0)^t) = 0,\\ \xi \in \mathbb{R}^2,\end{gathered} \tag{2}$$

where $\mu = \frac{\lambda_{0,1}}{\text{Re}\lambda_{0,1}}$, $c_1 \approx 29.69 - i143.7$, $c_2 \approx -28.03 + i642.4$, and $\gamma \approx 0.04525$. The second equation relates to the lowest-order term in the equation $\text{div}\, v = 0$. In this case, the mean flux is given by the expression

$$[\![(v_1, v_2)^t]\!] = \left(\frac{4}{3}, 0\right)^t - \frac{2}{3}\varepsilon^2 R_0[\![\nabla_\xi P + (\gamma|A|^2, 0)^t]\!] + \text{h. o. t.}$$

Hence, it follows that for modeling problems $(1)_{\mathcal{PF}}$ and $(1)_{\mathcal{FF}}$ we should complement system (2) by nonlocal conditions

$$\begin{aligned}\mathcal{PF}&\colon [\![P_{\xi_1}]\!] = 0 \text{ and } [\![P_{\xi_2}]\!] = 0;\\ \mathcal{FF}&\colon [\![|A|^2 + \gamma^{-1}P_{\xi_1}]\!] = 0 \text{ and } [\![P_{\xi_2}]\!] = 0.\end{aligned} \tag{3}$$

Analysis of problems $(1)_{\mathcal{PP}}$, $(1)_{\mathcal{FP}}$ leads to similar constraints.

In the absence of conditions (3), the system of modulation equations (2), which was first derived in [8] (see Eqs. 2.27, 2.28, and 2.34), cannot properly describe the mass flux and the pressure gradient of the fluid flow under consideration (cf. [2, Sect. 5]). The necessity of additional constraints was pointed out in [7]; however, there are some inconsistencies in the coefficients introduced there {see Eq. (6.35) of [7]}.

The appearance of the second equation for pressure (which has no time derivative) is typical of all flows of viscous incompressible fluids in problems with two unbounded directions. However, we now can return to the classical complex Ginzburg–Landau equation and reduce it to the case of a single unbounded variable, which corresponds to certain constraints for an appropriate subspace of solutions.

We consider problem $(1)_{\mathcal{PF}}$ and, first, search for the solutions independent of x_2, hence, for the solutions of the type of $(2)_{\mathcal{PF}}$, which are independent of ξ_2. Then, the second equation can be integrated so that $\partial_{\xi_1} P = -\gamma|A|^2 + \delta(t)$. From $(3)_{\mathcal{PF}}$, it follows that $\delta = \gamma[\![|A|^2]\!]$, and hence, the system of equations (2) is reduced to

$$\begin{aligned}\mathcal{PF}_{\xi_2\text{ – indep}}\ &\partial_\tau A - \Lambda_{11}\partial_{\xi_1}^2 A - \mu A\\ &- (c_1 - \gamma c_2)|A|^2 A - \gamma c_2[\![|A|^2]\!]A = 0\end{aligned} \tag{4}$$

with a nonlocal term (cf. [12]). Second, following [2] and [5], we may consider solutions to the set of equations (1), which are periodic in the downstream direction x_1 with a period close to E. This corresponds to searching for solutions to Eqs. (2) in the form $A(\tau, \xi) = e^{i\beta\xi_1}\tilde{A}(\tau, \xi_2)$ and $P(\tau, \xi) = \tilde{P}(\tau, \xi_2)$. Thus, we find

$$\begin{aligned}\mathcal{PF}_{\xi_1\text{ – per}}\ &\partial_\tau\tilde{A} - \Lambda_{22}\partial_{\xi_2}^2\tilde{A}\\ &- [\mu - \Lambda_{11}\beta^2]\tilde{A} - c_1|\tilde{A}|^2\tilde{A} = 0.\end{aligned} \tag{5}$$

For problem $(2)_{\mathcal{FF}}$, we may seek solutions independent of x_2, and hence, solutions to the system of equations (2), which are independent of ξ_2. Then, integrating the second equation yields $\partial_{\xi_1} P = -\gamma|A|^2 + \delta(t)$. It follows from Eqs. (3) that $\delta = 0$, and hence, system (2) is reduced to the equations

$$\mathcal{FF}_{\xi_2-\text{indep}}\ \partial_\tau A - \Lambda_{11}\partial_{\xi_1}^2 A - \mu A - (c_1 - \gamma c_2)|A|^2 A = 0. \tag{6}$$

We now consider the solutions to problem $(1)_{\mathcal{FF}}$, which are periodic in the downstream direction x_1 with a period close to E. This corresponds to the search for solutions of the form $A(\tau, \xi) = e^{i\beta\xi_1}\tilde{A}(\tau, \xi_2)$, $P(\tau, \xi) = \tilde{P}(\tau, \xi_2) + \delta(t)\xi_1$ to Eqs. (2) in which we have to admit variations of the downstream pressure gradient. In this case, we arrive at

$$\mathcal{FF}_{\xi_1-\text{per}}\ \partial_\tau\tilde{A} - \Lambda_{22}\partial_{\xi_2}^2\tilde{A} - [\mu - \Lambda_{11}\beta^2]\tilde{A} - c_1|\tilde{A}|^2\tilde{A} + \gamma c_2[\![|\tilde{A}|^2]\!]\tilde{A} = 0. \tag{7}$$

2. SINGLE-PULSE AND MULTIPULSE SOLUTIONS TO THE NAVIER–STOKES EQUATIONS IN THREE-DIMENSIONAL LAYERS

For problems (4)–(7) there exist pulse solutions of the form

$$A(\tau, \xi_j) = d_1 e^{i\nu\tau}[\cosh(\eta\xi_j)]^{d_2}$$

with $d_1, d_2 \in \mathbb{C}$, $\nu \in \mathbb{R}$, $\eta > 0$ and $\operatorname{Re} d_2 < 0$. We note that the nonlocal term with

$$[\![|A|^2]\!] = \lim_{L\to\infty}\frac{1}{2L}\int_{-L}^{L}|A(\xi_j)|^2 d\xi_j$$

vanishes for solutions decreasing at infinity.

There is a key difference concerning the interrelation between these modulation problems and the original Poiseuille problem. To prove the existence of such pulse solutions for the original problem, we need to use the reflection symmetry $\xi_j \mapsto -\xi_j$ that is inherent in problems (4) to (7). At the same time, problems $(1)_{\mathcal{PF}}$ and $(1)_{\mathcal{FF}}$ are invariant with respect to the reflection $x \mapsto (x_1, -x_2)$, but not with respect to the transformation $x \mapsto (-x_1, x_2)$. Therefore, we are only able to prove the existence of a pulse-type solution symmetric with respect to the reflection but not for the case of Eqs. (4) and (6) (cf. [5]). In order to transform the pulse solution to its stationary form, we introduce new parameters and write out the Ginzburg–Landau equation in the form

$$\partial_t A = (1 + i\kappa) \times [\partial_x^2 A - (1 + i\theta)^2 A + (1 + i\Omega)(2 + i\Omega)|A|^2 A]. \tag{8}$$

If θ and Ω are small, then this equation can be considered as a perturbation of either the real Ginzburg–Landau equation (if $\kappa \approx 0$) or the nonlinear Schrödinger equation (if $|\kappa| \gg 1$). As was first observed in [9] for $\theta = \Omega$, this equation has the explicit steady-state solution $H_\theta(x) = e^{i\gamma}[\cosh x]^{-(1+i\theta)}$. There are also more general steady-state pulse solutions to Eq. (8). In particular, in applications of the Ginzburg–Landau equation to laser optics, we are interested in the multipulse solutions, i.e., solutions in which $|A(\cdot)|^2$ has several well-distinguished maxima. Such solutions were found in [10] for the case $0 < |\Omega| \ll 1$ and $|\theta - \Omega| \ll |\Omega|$. These results were generalized and refined in [3, 4]. It was shown in [5] that, as applied to the Poiseuille problem, Ω lies between ~3.4 and ~22.74 for $\alpha \in (\alpha_4, \alpha_1)$. It is worth noting that, in problem (8), Ω is determined from the relation $\Omega^2 + 3M\Omega = 2$ with $M = \dfrac{\operatorname{Re}\left(\dfrac{c_1}{\Lambda_{22}}\right)}{\operatorname{Im}\left(\dfrac{c_1}{\Lambda_{22}}\right)}$.

We have no proof for the existence of solutions to the Navier–Stokes equations (1), which correspond to the Hocking–Stewartson pulses and are based on employing the DHS system and the multiparameter expansion. Instead of this, we use the Kirchgässner reduction (see [2, 5]). We fix the downstream periodicity $\dfrac{2\pi}{\alpha}$ and look for the solutions in the form of traveling waves

$$v(t, x_1, x_2, y) = \tilde{v}(x_1 - ct, x_2, y) = \tilde{v}\left(x_1 - ct + \frac{2\pi}{\alpha}, x_2, y\right). \tag{9}$$

The arising elliptic problem is reduced to four-dimensional reversible ordinary differential equations. In this case, we restrict our analysis to the wave-number interval $\alpha \in (\alpha_4, \alpha_1)$, since only the fact that the most unstable modes are caused by large-period spanwise perturbations is used in the reduction. The suitable replacement of the variables (cf. [2, 4]) leads to the equation

$$\frac{d^2 a}{d\zeta^2} - (1 + i\omega)^2 a + (1 + i\Omega)(2 + i\Omega)|a|^2 a + \eta^2 G_0\left(\omega, \Omega, \eta, a, \bar{a}, \frac{da}{d\zeta}, \frac{d\bar{a}}{d\zeta}\right) = 0,$$

where ω, Ω, and η are functions of the physical parameters R, c, and α. In particular, $\eta^2 = \mathbb{O}(|R - R_{crit}(\alpha)| + |c - c_{crit}(\alpha)|)$, whereas η is considered to be a small parameter. For $\eta = 0$ and $\omega = \Omega$, this equation has the single-pulse solution $H_\Omega(\zeta)$. Using methods of the theory of dynamical systems, we can prove the persistence of this single-pulse solution under variations of η for almost all ω. The exceptional values of ω give rise to an exceptional set $\mathcal{A} = \{a_1, a_2, \ldots\} \subset (\alpha_4, \alpha_1)$ for the Poiseuille problem, with $a_1 \approx 1.044$, $a_2 \approx 1.032$. Finally, we

arrive at the conclusion on the existence of single-pulse solutions to problems $(1)_{\mathcal{PF}}$ and $(1)_{\mathcal{FF}}$.

Statement 1. *For* $\alpha_* \in (\alpha_4, \alpha_1)\backslash\mathcal{A}$, *there exist the functions* $c^{(1)}(\cdot, \alpha_*)$: $(R_{crit}(\alpha_*) - \varepsilon, R_{crit}(\alpha_*)] \longrightarrow \mathbb{R}$ *and* $\varepsilon > 0$ *such that for an arbitrary* $R_* \in (R_{crit}(\alpha_*) - \varepsilon, R_{crit}(\alpha_*))$ *and* $c_* = c^{(1)}(R_*, \alpha_*)$, *problem* (1), (9) *with parameters* $R, c, \alpha) = (R_*, c_*, \alpha_*)$ *has the single-pulse solution* $\tilde{v}^{(1)} = V_{Pois} + \tilde{u}^{(1)}$, *where*

$$\tilde{u}^{(1)}(\xi, x_2, y) = \frac{\eta}{\rho}\mathrm{Re}([\cosh(\eta x_2)]^{-(1+i\Omega)}\Psi_0(\xi, y)) + \mathbb{O}(\eta^2 e^{-|\eta z|}),$$

with $\Psi_0(\xi, y) = e^{i\alpha\xi}(i\varphi'(y), 0, \alpha\varphi(y))^t$; $\xi = x - c_*t$, *and* $\eta = (\mu(R_{crit}(\alpha_*) - R_*))^{1/2}$. *Here,* μ, ρ, *and* Ω *are positive constants depending only on* α_*.

In the vicinity of the single-pulse solution, there are sequences of multipulse solutions.

Statement 2. α_*, R_*, $c_* = c^{(1)}(R_*, \alpha_*)$ *and* $\tilde{u}^{(1)}$ *be as in the preceding theorem. Then, for an arbitrary integer* $n \geq 2$ *and an arbitrarily small* $r > 0$, *there exists a parameter triplet* $(R^{(n)}, c^{(n)}, \alpha^{(n)})$ *with* $|(R_*, c_*, \alpha_*) - (R^{(n)}, c^{(n)}, \alpha^{(n)})| \leq r$ *such that, for* $(R, c, \alpha) = (R^{(n)}, c^{(n)}, \alpha^{(n)})$, *problem* (1), (9) *has the n-pulse solution* $\tilde{v}^{(n)} = V_{Pois} + \tilde{u}^{(n)}$. *This implies that, for* $k = 1, 2, \ldots, n$, *there exist* $z_k^{(n)} \in \mathbb{R}$ *and* $\beta_k^{(n)} \in S_\alpha = \mathbb{R}/(2\pi/\alpha)\mathbb{Z}$ *such that*

$$\sup\left\{\left\|\tilde{u}^{(n)}(\cdot x_2, \cdot) - \sum_{k=1}^{n}\tilde{u}^{(1)}(\cdot - \beta_k^{(n)}, x_2 - z_k^{(n)}, \cdot)\right\|_{H^2(S_\alpha \times [-1,1])} : x_2 \in \mathbb{R}\right\} \leq r.$$

The additive representation of the *n*-pulse solution is meaningful, since the shifts $|z_k^{(n)} - z_{k+1}^{(n)}|$ between the single pulse solutions tend to infinity as $r \longrightarrow 0$. Thereby, the *n*-pulse solution $\tilde{u}^{(n)}$ looks like *n* copies of the single-pulse solution $\tilde{u}^{(1)}$, which are shifted along the x_2 direction.

The stability of the pulse solutions to the Poiseuille problem is determined by the stability of the solution H_θ to the Ginzburg–Landau equation written out in the form of Eq. (8). As is clear, it can be stable only provided that the asymptotic state $A \equiv 0$ is stable as well. From the analysis of the continuous spectrum, we obtain the necessary stability condition, $-1 + 2\kappa\theta + \theta^2 \leq 0$ [11]. In addition, there also exist discrete eigenvalues. In particular, due to the translational and rotational invariance, we always obtain the double eigenvalue $\lambda = 0$.

In the general case, the discrete spectral component can be determined only numerically (see [1, 6].) The calculations performed in [l] confirm the fact that the single-pulse solutions to the Poiseuille problem are unstable for $\alpha \in (\alpha_4, \alpha_1)$ due to the existence of a real positive eigenvalue. We have no data on the behavior of the single-pulse solution branch for small R. However, if there exists a turning point for a certain R, then pulses with a finite amplitude can be stable. In this case, they may play an important role in the space–time chaotization of the 3D Poiseuille problem much lower than the classical instability threshold. From the results of [3, 4], it is possible to prove the existence of spatially chaotic (with respect to x_2) solutions (9) to problem (1). It would be interesting to study properties of attractors in problems (2), (3), in particular, to estimate the value of the ε-entropy per unit volume as was done in the case of Ginzburg–Landau equation (see, e.g., [11]).

ACKNOWLEDGMENTS

This work was supported by the Russian Foundation for Basic Research, project no. 00-01-00387, and by the INTAS, grant no. 899.

REFERENCES

1. A. Afendikov and T. Bridges, Proc. R. Soc. London, Ser. A **457**, 257 (2001).
2. A. Afendikov and A. Mielke, Arch. Ration. Mech. Anal. **129**, 101 (1995).
3. A. Afendikov and A. Mielke, J. Diff. Eqns. **159**, 370 (1999).
4. A. L. Afendikov and A. Mielke, Dokl. Akad. Nauk **369**, 153 (1999).
5. A. Afendikov and A. Mielke, Z. Angew. Math. Phys. **52**, 79 (2001).
6. W.-J. Beyn and J. Lorenz, Numer. Func. Anal. Optim. **20**, 201 (1999).
7. P. Bollerman, *On the Theory of Validity of Amplitude Equations*, PhD Thesis (Utrecht Univ., Utrecht, 1996).
8. A. Davey, L. M. Hocking, and K. Stewartson, J. Fluid Mech. **63**, 529 (1974).
9. L. M. Hocking and K. Stewartson, Proc. R. Soc. London, Ser. A **326**, 289 (1972).
10. T. Kapitula and S. Maier-Paape, Z. Angew. Math. Phys. **47**, 265 (1996).
11. A. Mielke, in *Handbook for Dynamical Systems* (Springer-Verlag, New York, 2000), Vol. 3, p. 532.
12. K. Stewartson and J. T. Stuart, J. Fluid Mech. **48**, 529 (1971).

Translated by A. Afendikov

Doklady Physics, Vol. 46, No. 12, 2001, pp. 873–875. Translated from Doklady Akademii Nauk, Vol. 381, No. 4, 2001, pp. 484–486.

MECHANICS

Dynamic Effects in Flowing-Down Layers of Magnetic Fluids in Unsteady Magnetic Fields

V. A. Buchin and G. A. Shaposhnikova

Presented by Academician S.S. Grigoryan July 20, 2001

Received July 23, 2001

The action of unsteady magnetic fields on thin layers of a viscous incompressible magnetic fluid flowing down along an inclined plane is studied. Transition processes between two steady-state flows of layers of the magnetic fluid, which correspond to various magnetic-field gradients, are investigated. These processes are shown to be accompanied by the initiation and motion of solitons.

We investigated the interaction between the layer perturbations introduced at a certain flow point and generated by harmonic disturbances of the magnetic-field gradient. The convective instability of the magnetic-fluid layer was shown to be suppressed by the intentionally selected oscillating magnetic-field gradient.

1. A SET OF EQUATIONS

To describe the flow of a thin layer of a viscous incompressible magnetic fluid along an inclined plane, we use the following set of equations:

$$\frac{\partial h}{\partial t} + \frac{\partial q}{\partial x} = 0, \tag{1}$$

$$\frac{\partial q}{\partial t} + 1.2\frac{\partial}{\partial x}\frac{q^2}{h} = gh\sin\alpha - \frac{3\nu q}{h^2} + h\frac{MG}{\rho}, \quad G = \frac{\partial H}{\partial x}. \tag{2}$$

Here t is time, x is the coordinate directed along the plane slope, h is the layer thickness, q is the volume fluid velocity, ρ is the density, ν is the kinematic viscosity, g is the gravitational acceleration, α is the plane slope angle, M is the magnetization of the magnetic fluid, H is the magnetic-field intensity, and G is the component of the magnetic-field gradient along the x-axis.

The set of equations (1), (2) is obtained by averaging over the layer thickness the continuity equations and equations of motion for a viscous incompressible magnetic fluid, with allowance for boundary conditions on both the free fluid surface and the rigid wall (inclined plane) [1]. When deriving the set of equations, we assume that $M \ll H$ and ignore in equation (2) the contribution of the surface tension.

We introduce the following dimensionless variables and parameters: h_c, u_c, and t_c, which are the characteristic values for the layer thickness, volume flow, and time, while L is the characteristic layer length:

$$t^* = \frac{t}{t_c}, \quad x^* = \frac{x}{L}, \quad q^* = \frac{q}{q_c},$$

$$h^* = \frac{h}{h_c}, \quad q_c = \frac{g\sin\alpha h_c^3}{3\nu},$$

$$t_c = \frac{h_c L}{q_c}, \quad \beta = \frac{9\nu^2 L}{g\sin\alpha h_c^4}, \quad \gamma = \frac{MG}{\rho g\sin\alpha}.$$

Furthermore, the asterisk in the superscript is omitted.

It is easy to see that, in the case of a constant component of the magnetic-field gradient G, the set of equations (1), (2) has the steady-state solution

$$h = (1+\gamma)^{-1/3}, \quad q = 1. \tag{3}$$

The steady-state thickness of the magnetic-fluid layer depends on the value of the magnetic-field-gradient component G. When the components of the magnetic field and the gravity field are aligned in the same direction, the thickness of the steady magnetic-fluid layer is smaller in the presence of the magnetic-field gradient than in its absence. In the case of opposite directions of the components of the magnetic field and gravity field ($\gamma < 0$), the thickness of the steady-state magnetic-fluid-layer is larger in the presence of the magnetic-field gradient than in its absence.

2. TRANSITION PROCESSES IN THE PRESENCE OF A MAGNETIC-FIELD GRADIENT

Imposing the magnetic-field gradient across the layer flowing down along the inclined plane leads to transforming the flowing-down layer from one steady state to another. Without the magnetic-field gradient

Institute of Mechanics, Moscow State University, Michurinskiĭ pr. 1, Moscow, 117192 Russia

1028-3358/01/4612-0873$21.00

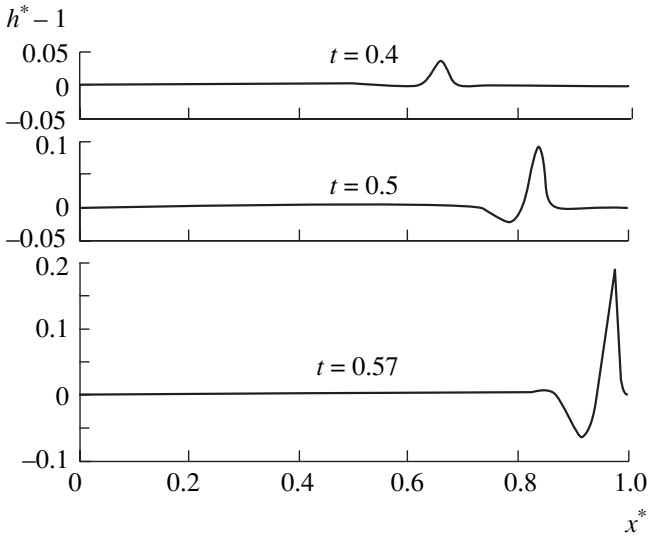

Fig. 1. Variation $h^* - 1$ of the layer thickness as a function of the x^* coordinate; $\beta = 10$; $\gamma = -0.01$.

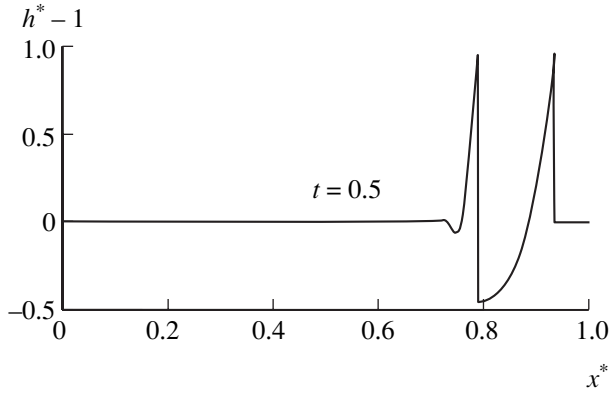

Fig. 2. Variation $h^* - 1$ of the layer thickness as a function of the x^* coordinate; $\beta = 20$; $\gamma = -0.01$.

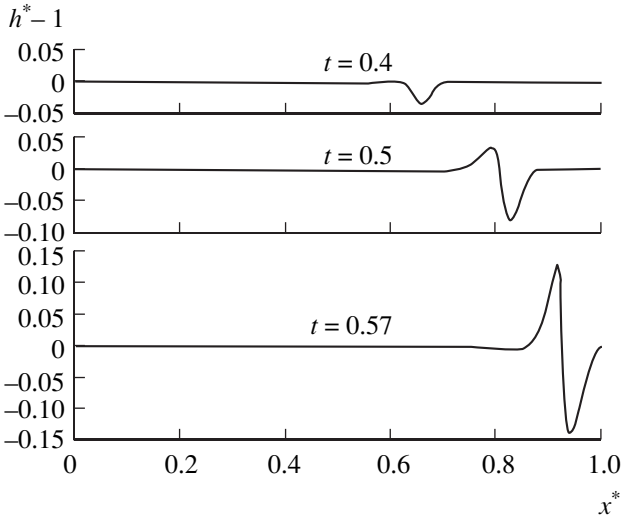

Fig. 3. Variation $h^* - 1$ of the layer thickness as a function of the x^* coordinate; $\beta = 10$; $\gamma = 0.01$.

($\gamma = 0$), the set of equations (1), (2) has the steady-state solution

$$h = 1, \quad q = 1. \tag{4}$$

We investigate the transition process between two steady-state flows of a magnetic-fluid layer, which corresponds to the cases of a flow with and without a constant magnetic-field gradient, whereas the volume flow is conserved.

We use the boundary conditions for $x = 0$:

$$h = 1, \quad q = 1, \tag{5}$$

and the initial conditions for $t = 0$:

$$h = 1, \quad q = 1. \tag{6}$$

In this paper, we always consider reasonably large plane slopes such that both characteristics of hyperbolic set (1), (2) are directed downstream.

The set of equations and boundary conditions (1), (2), (5), and (6) were solved numerically with the help of an IBM PC and using the Godunov method.

The results of numerical calculation for the flow reconstructed from one steady state (without magnetic field) to another (with a constant magnetic-field gradient) are shown in Figs. 1–3. We plotted the dimensionless coordinate $x^* = \frac{x}{L}$ for the abscissa and the dimensionless layer-thickness variation $h^* - 1$ for the ordinate.

In Fig. 1, we show the calculation results for the values of parameters $\gamma = -0.01$ and $\beta = 10$ at the time moments $t^* = 0.4, 0.5, 0.57$. For $t^* = 0.77$, the solution is saturated and attains a steady-state value. In the case indicated ($\beta \gg 1$), the steady-state layer thickness h is constant in the presence of the magnetic-field gradient. This thickness is determined by formula (3) everywhere except in the neighborhood of the point $x = 0$. Since $\gamma < 0$, the steady thickness of the magnetic-fluid layer is larger in the presence of the gradient than without it.

In Fig. 2, we show the calculation results for the values of parameters $\gamma = -0.01$ and $\beta = 20$ at the time moment $t^* = 0.5$. The larger value of the quantity β corresponds to the larger value of the layer length L.

It is seen that the passage from a certain steady state of the flow to another steady state is accompanied by the initiation of a solitary hump (soliton), whose height exceeds the thickness difference in the initial and final steady states by orders of magnitude. As the soliton propagates, a wave trough is formed beyond it; furthermore, the second soliton appears. As a result, a packet of solitons propagates along the layer surface, the number of solitons in the packet increasing downstream with x.

In Fig. 3, we present the calculation results for the values of the parameters $\gamma = 0.01$ and $\beta = 10$ at the time moments $t^* = 0.4, 0.5, 0.57$. In this case ($\gamma > 0$), a trough appears first; a hump, i.e., a soliton appears second. The steady-state layer thickness is smaller in the

presence of the magnetic-field gradient than without it. In this case, for reasonable lengths of the layer, a packet of solitons is also formed.

In order that no strong perturbations were initiated in the layer by the magnetic-field gradient, it must vary reasonably slowly.

3. SUPPRESSION OF HARMONIC PERTURBATIONS BY AN OSCILLATING MAGNETIC-FIELD GRADIENT

We consider the problem of developing harmonic perturbations introduced at $x = 0$ into the layer of a viscous magnetic fluid flowing down along an inclined plane. As was noted above, we consider reasonably large plane slopes such that both characteristics of hyperbolic set (1), (2) are directed downstream, and all perturbations introduced at the point $x = 0$ drift downstream. It is easy to show that perturbations introduced into the flow increase with x; i.e., steady-state flows (3) and (4) are unstable with respect to small perturbations. Steady flows are also unstable with respect to small perturbations of the magnetic-field gradient, which are given in the form

$$\gamma = \gamma_0 + \delta\exp\{i\omega t\}. \quad (7)$$

The investigation of interactions between the harmonic perturbations introduced into the layer at $x = 0$ and those given by formula (7) showed that for certain values of the parameters $\mathrm{Re}\,\delta$ and $\mathrm{Im}\,\delta$ the suppression of perturbations of both the layer thickness and volume flow is possible. In the case when the perturbations introduced in the layer are given by the expressions

$$x = 0, \quad h_0 = h_{0c}\cos(\omega t) - h_{0s}\sin(\omega t),$$

$$q = q_{0c}\cos(\omega t) - q_{0s}\sin(\omega t),$$

the magnetic-field gradient suppressing these perturbations is determined by the formulas (assuming $\gamma_0 = 0$)

$$\gamma = \gamma_c\cos(\omega t) - \gamma_s\sin(\omega t),$$

$$\gamma_c = q_{0c} - \frac{\omega q_{0s}}{\beta} + \frac{\omega(h_{0s}a - h_{0c}b)}{\beta(r_1^2 + r_2^2)},$$

$$\gamma_s = q_{0s} + \frac{\omega q_{0c}}{\beta} + \frac{\omega(h_{0s}a + h_{0c}b)}{\beta(r_1^2 + r_2^2)},$$

$$a = \frac{25}{16}\beta^2 - \frac{\omega^2}{6}, \quad b = \frac{5}{3}\beta\omega,$$

$$r_1 = -\frac{5}{4}\beta - \mathrm{Re}\sqrt{D}, \quad r_2 = -\omega - \mathrm{Im}\sqrt{D},$$

$$D = -\frac{1}{6}\omega^2 + \frac{5}{3}\beta i\omega + \frac{25}{16}\beta^2.$$

ACKNOWLEDGMENTS

This work was supported by the Russian Foundation for Basic Research, project no. 99-01-01155.

REFERENCES

1. V. A. Buchin and G. A. Shaposhnikova, J. Magn. Magn. Mater. **201**, 343 (1999).

Translated by V. Bukhanov

Doklady Physics, Vol. 46, No. 12, 2001, pp. 876–880. Translated from Doklady Akademii Nauk, Vol. 381, No. 4, 2001, pp. 487–491.

MECHANICS

A Nonlinear Game Problem on Reorientating an Asymmetric Solid by Means of Relay-Controlled Bounded Moments

V. I. Vorotnikov

Presented by Academician V.V. Rumyantsev July 2, 2001

Received July 2, 2001

A nonlinear game problem on reorientating an asymmetric solid under uncontrolled disturbances is considered. We develop a method of solving this problem which is based on the *equivalent linearization* of nonlinear conflict-controlled systems [1–5] and on the methods of the linear theory of games [6]. In contrast to papers [1–5], in which realizations of controls force moments were described by piecewise continuous functions with five switchings, we consider here the reorientation by means of piecewise constant controls, with only one switching for each control.

Estimates for the tolerance range of the disturbances are found depending on the restrictions imposed on both the control and the initial position of the body. Within these estimates, a constructive scheme for derivation of the position controls of the indicated type is given, and the upper bound of the warranted reorientation time is found.

1. FORMULATION OF THE PROBLEM

We consider the Euler equations of motion

$$A_1\dot{x}_1 = (A_2 - A_3)x_2x_3 + u_1 + v_1 \quad (123), \qquad (1.1)$$

which describe angular motion of a solid with respect to its center of mass. (Only one of the three equations is written out; two others are obtained by the cyclic permutation of the subscripts: $1 \longrightarrow 2 \longrightarrow 3$.)

Here, x_i and u_i are the angular velocity components and the control moment components along the principal central axes of inertia, respectively, and A_i are the principal central moments of inertia. The moments v_i specify external forces and uncontrolled disturbances. Hereafter, $i = 1, 2$, and 3, and summation over subscript i is extended from 1 to 3. By $\mathbf{x}$, $\mathbf{u}$, and $\mathbf{v}$, we denote the vectors composed by x_i, u_i, and v_i, respectively.

Nizhniĭ Tagil Institute of Ural State Technical University, ul. Krasnogvardeĭskaya 59, Nizhniĭ Tagil, 622006 Russia

Together with (1.1), we consider the kinematic equations describing the body orientation in the Rodrigue–Hamilton variables:

$$\begin{aligned} 2\dot{\lambda}_0 &= -\sum(x_i\lambda_i), \\ 2\dot{\lambda}_1 &= x_1\lambda_0 + x_3\lambda_2 - x_2\lambda_3 \quad (123). \end{aligned} \qquad (1.2)$$

The variables λ_0 and λ_i composing a quaternion $\boldsymbol{\lambda}$ are interrelated by the equality

$$\lambda_0^2 + \sum\lambda_i^2 = 1. \qquad (1.3)$$

We choose the controls $u_i \in K$ to belong to a class K of functions $\mathbf{u} = \mathbf{u}(\mathbf{x}, \boldsymbol{\lambda}, \mathbf{x}^0, \boldsymbol{\lambda}^0)$ whose realizations $u_i[t]$ are piecewise constant functions with one switching for each i. Here, $\mathbf{x}^0$ and $\boldsymbol{\lambda}^0$ are initial values of $\mathbf{x}$ and $\boldsymbol{\lambda}$, respectively. The controls $u_i \in K$ satisfy the constraints

$$|u_i| \le \alpha_i = \text{const} > 0, \qquad (1.4)$$

corresponding to three pairs of drivers fixed with respect to the body axes [7]. We point out the dependence of the controls on the initial values $\mathbf{x}^0$ and $\boldsymbol{\lambda}^0$, because the form of the controls used below is dependent on these values.

The disturbances $v_i \in K_1$ can be realized as arbitrary piecewise continuous functions $v_i[t]$ satisfying the restrictions

$$|v_i| \le \beta_i = \text{const} > 0. \qquad (1.5)$$

In this case, we assume that any probability characteristics of the disturbance realizations satisfying inequalities (1.5) are unknown.

Problem 1. The problem is to find the controls $u_i \in K$ under arbitrary disturbances $v_i \in K_1$ such that the body makes the transition from an initial state $\boldsymbol{\lambda}(t_0) = \boldsymbol{\lambda}^0$ to a given state $\boldsymbol{\lambda}(t_1) = \boldsymbol{\lambda}^1$ during a finite time. Both the states are assumed to be states of rest; i.e., $\mathbf{x}(t_0) = \mathbf{x}^0 = \mathbf{x}(t_1) = \mathbf{x}^1 = \mathbf{0}$. The time moment $t_1 > t_0$ is not fixed.

1028-3358/01/4612-0876$21.00

Without loss of generality, we assume that $\boldsymbol{\lambda}^1 = (1, 0, 0, 0)$ and that $\lambda_0^0 > 0$, because the quaternions $\boldsymbol{\lambda}$ and $-\boldsymbol{\lambda}$ correspond to one and the same angular position of the body.

2. METHOD OF SOLVING PROBLEM 1

Following [2–4], we differentiate the equations for $\dot{\lambda}_i$ in system (1.2) with respect to time and substitute expressions (1.1) for $\dot{x}_i$. As a result, we obtain the equalities

$$\ddot{\lambda}_1 = f_1(\boldsymbol{\lambda}, \mathbf{u}) + \varphi_1(\boldsymbol{\lambda}, \mathbf{v}, \mathbf{x}),$$

$$f_1 = \frac{1}{2}(\lambda_0 u_1 A_1^{-1} + \lambda_2 u_3 A_3^{-1} - \lambda_3 u_2 A_2^{-1}),$$

$$\varphi_1 = \frac{1}{2}[\lambda_0(v_1 + M_1)A_1^{-1} + \lambda_2(v_3 + M_3)A_3^{-1} \quad (2.1)$$

$$-\lambda_3(v_2 + M_2)A_2^{-1}] - \frac{1}{4}\lambda_1 \sum x_i^2,$$

$$M_1 = (A_2 - A_3)x_2 x_3 \quad (123).$$

In [2–4], the quantities f_i and φ_i are treated as auxiliary controls and disturbances, respectively. In such an approach, the realizations of the original controls u_i are piecewise continuous functions with five switchings. Based on the method of equivalent linearization, we find a solution to Problem 1 in the class of piecewise constant (relay) controls u_i with one switching for each i. To do this, we present Eqs. (2.1) in the form

$$\ddot{\lambda}_i = f_i^*(\mathbf{u}) + \varphi_i^*(\boldsymbol{\lambda}, \mathbf{u}, \mathbf{v}, \mathbf{x}), \quad (2.2)$$

where

$$f_i^* = \frac{1}{2}u_i A_i^{-1},$$

$$\varphi_1^* = \frac{1}{2}[(\lambda_0 - 1)u_1 A_1^{-1}$$

$$+ \lambda_2 u_3 A_3^{-1} - \lambda_3 u_2 A_2^{-1}] + \varphi_1 \quad (123).$$

We treat the quantities f_i^* and φ_i^* as auxiliary controls u_i^* and disturbances v_i^*, respectively. As a result, expressions (2.2) can be considered as a conflict-controlled system described by the equations

$$\ddot{\lambda}_i = u_i^* + v_i^*. \quad (2.3)$$

In this case, the original controls u_i have the form

$$u_i = 2A_i u_i^*. \quad (2.4)$$

On the basis of corresponding game problems for the linear system (2.3), we will construct a solution to the original nonlinear Problem 1. In order to estimate the auxiliary disturbances v_i^*, we use the method of prescribing and subsequently verifying their levels on the set S of the states of linear system (2.3) [2].

We now solve the problem on the fastest transition (under arbitrary tolerable disturbances v_i^*) of system (2.3) to the position

$$\lambda_i = \dot{\lambda}_i = 0. \quad (2.5)$$

We considered this problem as a differential game. For the problem to be solvable, tolerable values of u_i^* must exceed those of v_i^*. The corresponding constraints are taken as

$$|u_i^*| \le \alpha_i^*, \quad |v_i^*| \le \beta_i^* = \rho_i \alpha_i^*, \quad 0 < \rho_i < 1.$$

For fixed α_i^* and β_i^*, such that $\alpha_i^* > \beta_i^*$, this game problem for system (2.3) is reduced to the problem of optimum operation speed for the system

$$\ddot{\lambda}_i = (1 - \rho_i)u_i^*, \quad |u_i^*| \le \alpha_i^*. \quad (2.6)$$

The boundary conditions coincide with those imposed on system (2.3). System (2.6) is obtained from (2.3) if $v_i^* = -\rho_i u_i^*$. This case corresponds to the worst values of v_i^*, i.e., to the optimum controls from the standpoint of an enemy.

The solution to the operation-speed problem for system (2.6) takes the form [8]

$$u_i^*(\lambda_i, \dot{\lambda}_i) = \begin{cases} \alpha_i^* \operatorname{sgn}\psi_i(\lambda_i, \dot{\lambda}_i), & \psi_i \neq 0 \\ \alpha_i^* \operatorname{sgn}\lambda_i = -\alpha_i^* \operatorname{sgn}\dot{\lambda}_i, & \psi_i = 0. \end{cases} \quad (2.7)$$

Here, $\psi_i = -\dot{\lambda}_i - [2\lambda_i^*(1 - \rho_i)]^{-1}\lambda_i|\lambda_i|$ are the switching functions.

By virtue of the equality $\dot{\lambda}_i^0 = \dot{\lambda}_i^1 = 0$ (which follows from the equalities $\mathbf{x}^0 = \mathbf{x}^1 = \mathbf{0}$), the quantity

$$\tau = \max(\tau_i) \text{ with } \tau_i = 2\{|\lambda_i^0|[\alpha_i^*(1 - \rho_i)]^{-1}\}^{1/2} \quad (2.8)$$

specifies the minimum warranted control time in the linear game problem for system (2.3) and, therefore, the warranted reorientation time in Problem 1.

Algorithm 1 of solving Problem 1 involves the following steps [2–4]:

(1°) Prescription of β_i^* and trial choice of $\tau = \tau_i$; according to (2.8), this predetermines values of α_i^* and ρ_i entering into (2.7).

(2°) Verifying the fulfillment of the inequalities $|v_i^*| \le \beta_i^*$ and constraints (1.4) on the set S of the states of the system described by (2.3) and (2.7).

A specific realization of this algorithm is given in Section 4.

3. ESTIMATION OF THE TOLERANCE RANGE OF UNCONTROLLED DISTURBANCES

We now find a sufficient condition to be imposed on α_i, β_i, and $\boldsymbol{\lambda}^0$ in order for Problem 1 to be solved by the method proposed. To do this, we introduce the notation $\Gamma = \min(\Gamma_i)$, where $\Gamma_i = \alpha_i A_i^{-1}$, and prove the following theorem.

Theorem 1. *Let the tolerance range of the disturbances v_i be estimated by the inequality*

$$\left[\sum(\beta_i A_i^{-1})^2\right]^{1/2} < (1 - \sqrt{3}\lambda_*)\Gamma,$$
$$\lambda_* = \frac{1}{2}\sqrt{2(1-\lambda_0^0) - \min(\lambda_i^0)^2}. \tag{3.1}$$

Then the controls given by Eqs. (2.4) *and* (2.7) *and satisfying restriction* (1.4) *are solutions to Problem* 1.

Proof of the theorem consists of three stages.

(1) The components u_i satisfy the inequalities

$$|u_i| = 2A_i|u_i^*| \le 2A_i\alpha_i^*. \tag{3.2}$$

(2) We now estimate the components v_i^*. Using the inequalities $|x_1x_2| \le \frac{1}{2}\sum x_i^2$ (123), the Cauchy–Bunyakowsky inequality, and relationships (1.3), we obtain the following inequalities for v_i^* given by Eqs. (2.2):

$$|v_1^*| \le \beta^* + \frac{1}{2}\left\{\left[(\lambda_0 - 1)^2 + \lambda_2^2 + \lambda_3^2\right]\left[\sum(u_i^*)^2\right]\right\}^{1/2}$$
$$+ \frac{1}{4}|\lambda_0 r_1 + \lambda_2 r_3 - \lambda_3 r_2 - \lambda_1|\sum x_i^2$$
$$\le \beta^* + \lambda_*\left[\sum(\alpha_i^*)^2\right]^{1/2} + \frac{1}{4}L\sum x_i^2, \tag{3.3}$$

$$\beta^* = \frac{1}{2}[(\beta_i A_i^{-1})^2]^{1/2}, \quad L = \left(1 + \sum r_i^2\right)^{1/2},$$
$$r_1 = (A_1 - A_3)(A_2)^{-1} \quad (123).$$

To estimate $\sum x_i^2$, we solve the equations for $\dot\lambda_i$ entering into (1.2), considering them as algebraic equations with respect to x_i. As a result, we obtain the equalities

$$x_1 = 2\lambda_0^{-1}[(\lambda_0^2 + \lambda_1^2)\dot\lambda_1 + (\lambda_1\lambda_2 + \lambda_0\lambda_3)\dot\lambda_2$$
$$+ (\lambda_1\lambda_3 - \lambda_0\lambda_2)\dot\lambda_3] \quad (123). \tag{3.4}$$

Relationship $\lambda_0^2 \ge (\lambda_0^0)^2$ is valid on the set S [1–4]. Therefore, by virtue of (3.4), we arrive at the following estimates:

$$\frac{1}{4}\sum x_i^2 = \lambda_0^{-2}\left[\sum(\lambda_i\dot\lambda_i)\right]^2$$
$$+ \sum\dot\lambda_i^2 \le \lambda_0^{-2}\left(\sum\lambda_i^2\right)\sum\dot\lambda_i^2 + \sum\dot\lambda_i^2$$
$$= \left[\lambda_0^{-2}\left(\sum\lambda_i^2\right) + 1\right]\sum\dot\lambda_i^2 = \lambda_0^{-2}\sum\dot\lambda_i^2 \le (\lambda_0^0)^{-2}\sum\dot\lambda_i^2.$$

On the set S, the quantities $\dot\lambda_i^2$ satisfy the inequalities [2, 3]

$$\dot\lambda_i^2 \le (\dot\lambda_i^+)^2 = |\lambda_i^0|(\alpha_i^*)^{-1}[(\alpha_i^*)^2 - (\beta_i^*)^2].$$

As a result,

$$|v_i^*| \le \varphi,$$
$$\varphi = \beta^* + \lambda_*\left[\sum(\alpha_i^*)^2\right]^{1/2} \tag{3.5}$$
$$+ (\lambda_0^0)^{-2}L\sum\{|\lambda_i^0|(\alpha_i^*)^{-1}[(\alpha_i^*)^2 - (\beta_i^*)^2]\}.$$

(3) Finally, we use estimates (3.2) and (3.5) in order to prove the theorem. We first prove that, if conditions (3.1) are satisfied, then there exist the numbers α_i^* and β_i^* such that (a) $\alpha_i^* > \beta_i^*$ and (b) the inequalities (confirming the levels β_i^* prescribed for the auxiliary disturbances v_i^*)

$$|v_i^*| \le \beta_i^* \tag{3.6}$$

are valid on the set S, with inequalities (1.4) also satisfied.

According to (3.1), we take

$$\beta^* = \frac{1}{2}(1 - \sqrt{3}\lambda_*)\Gamma - \varepsilon,$$
$$\alpha_i^* = \alpha^* = \frac{1}{2}\Gamma, \quad \beta_i^* = \frac{1}{2}\Gamma - \varepsilon_1, \tag{3.7}$$

where $\varepsilon > \varepsilon_1 > 0$ are infinitesimal numbers.

In this case, $\alpha_i^* > \beta_i^*$ for infinitesimal fixed $\varepsilon > 0$. Therefore, the auxiliary game problem for linear system (2.3) is solvable [6].

We now prove that, for a sufficiently small $\varepsilon > 0$, inequalities (3.6) are valid on the set S. Indeed, in this case, the difference between the quantity φ given by (3.5) and the value $\varphi = \frac{1}{2}\Gamma$ is arbitrary small. Therefore, with regard to (3.7), we have $|v_i^*| \le \beta_i^*$ on the set S.

We also prove that restrictions (1.4) are valid on the set S for a sufficiently small $\varepsilon > 0$. Indeed, according to (3.2), (3.7), and the inequality $\Gamma \le \Gamma_i$, we have

$$|u_i| \le 2A_i\alpha_i^* = A_i\Gamma \le A_i\Gamma_i = \alpha_i.$$

Thus, if conditions (3.1) are satisfied on the set S, choosing a sufficiently small $\varepsilon > 0$, we can find that (*1*) the prescribed levels v_i^* are verified and (*2*) the controls given by (2.4) and (2.7) meet restrictions (1.4). The theorem is proved.

Discussion of Theorem 1. 1°. Condition (3.1) is sufficient because it is obtained by using reinforcing inequalities. For sufficiently large (although finite) values of τ, the controls given by (2.4) and (2.7) are solutions to Problem 1 provided that condition (3.1) is met. If this condition is satisfied with a "reserve," then algorithm *1* of solving Problem 1 (see Section 2) can be used. In Section 4, this algorithm will be defined more exactly.

2°. Inequality (3.1) is not an absolute estimate for the possibility of reorientating the body under disturbances, because it is directly related to the controls having form (2.4), which was proposed above in order to solve Problem 1. Such an expression is one of the possible forms given by the equalities

$$u_i = 2A_j u_j^*, \tag{3.8}$$

in which the subscripts i and j are not necessarily coincident, varying from 1 to 3. With due regard for this remark and the assumption $\lambda^1 = (1, 0, 0, 0)$ made above, we can take $\lambda_0^0 \ge \frac{1}{2}$ in formula (3.1). Otherwise, it is necessary to pass from controls (2.4) to one of the possible forms given by (3.8); in this case, an estimate similar to (3.1) also holds.

3°. Inequality (3.1) makes sense for $\frac{\sqrt{3}}{3} - \lambda_* > 0$. Without loss of generality, we can take $\lambda_0^0 \ge \frac{1}{2}$; therefore, this inequality can always be considered as valid. In the limiting case of formula (2.4) with $\lambda_0^0 = \frac{1}{2}$, we should take $\min(\lambda_i^0)^2 = \frac{1}{4}$, bearing in mind the possible passage to one of the forms given by (3.8). In this limiting case, $1 - \sqrt{3}\,\lambda_* = \frac{1}{4}$. In another limiting case of $\lambda_0^0 \longrightarrow 1$, we have $\left[\sum(\beta_i A_i^{-1})^2\right]^{1/2} < \Gamma$.

4°. The realizations of the controls given by Eqs. (2.4) and (2.7) are piecewise constant functions, each having one switching (so-called "bang-bang" control). In this case, each of the fixed drivers realizing such controls operates in an acceleration–deceleration mode. It should be pointed out that the control moments u_i have no synchronous switchings, except for the worst values of v_i^*.

5°. The approach proposed, following the idea of decomposition of nonlinear controlled systems [9], is based on the method [10] of studying nonlinear problems on the partial stabilization of a motion (i.e., with respect to a part of its variables) [10–12]. The topic of this article is related to control problems on an aircraft flight subjected to disturbances (for example, gusts, etc.) [13–15].

4. SPECIFIC REALIZATION OF THE ALGORITHM OF SOLVING PROBLEM 1

Let condition (3.1) be satisfied with a reserve, i.e.,

$$\left[\sum(\beta_i A_i^{-1})^2\right]^{1/2} < (1 - \sqrt{3}\lambda_*)\Gamma - \Delta, \tag{4.1}$$

where $\Delta > 0$ is a certain given number.

Algorithm 2 of solving Problem 1 involves the following steps:

1°. According to (3.7), we take $\alpha_i^* = \alpha^*$; therefore, inequalities (1.4) are satisfied.

2°. We prescribe a trial value of $\tau = \tau_i$. By virtue of (2.8), this predetermines values of β_i^*.

3°. Inequalities $|v_i^*| \le \beta_i^*$ are verified with the use of estimates (3.5). If these inequalities are not satisfied (or satisfied with a reserve), the value of τ must be increased (or decreased).

The following theorem defines the direct upper estimate of the quantity τ.

Theorem 2. *Let equality* (4.1) *be valid. Then,*

$$\tau \le \tau^* = 2\lambda^*(2\Delta^{-1})^{1/2},$$
$$\lambda^* = \{\max|\lambda_i^0| + 2L[(\lambda_0^0)^{-2} - 1]\}^{1/2}. \tag{4.2}$$

5. EXAMPLE

Let us consider the reorientation of a solid (spacecraft), provided that its angular position given by $\mathbf{x}^0 = \mathbf{0}$ and $\lambda^0 = (0.701, 0.353, 0.434, 0.432)$ is changed to that given by $\mathbf{x}^1 = \mathbf{0}$ and $\boldsymbol{\lambda}^1 = (1, 0, 0, 0)$. The body's moments of inertia are $A_1 = 4 \times 10^4$, $A_2 = 8 \times 10^4$, and $A_3 = 5 \times 10^4$ kg m^2.

We assume that $\alpha_i = 800$ N m. In this case, $\lambda_* = 0.3440$, $\Gamma = 0.01$ s^2, and estimate (3.1) takes the form

$$\left[\sum(\beta_i A_i^{-1})^2\right]^{1/2} < 40.42 \times 10^{-4} \text{ s}.$$

If, for example, $\beta_1 = \beta_3 = 0$, then $\beta_2 = 323.36$ N m. Assuming that the reserve $\Delta = 5 \times 10^{-4}$ N m, we take, in

accordance with (3.7),

$$\alpha_1^* = \alpha^* = 5 \times 10^{-3}\ \mathrm{s}^{-2}. \quad (5.1)$$

Using Algorithm 2 described above, we find that the time taken for the reorientation of the body by means of the controls described by Eqs. (2.4), (2.7), and (5.1) is $\tau = 235.06$ s. In this case, constraints (1.4) are satisfied.

For comparison, direct estimate (4.2) yields $\tau^* = 237.19$ s.

ACKNOWLEDGMENTS

This work was supported in part by the Russian Foundation for Basic Research, project no. 99-01-00965, and by the Ministry of Education.

REFERENCES

1. V. I. Vorotnikov, Prikl. Mat. Mekh. **58** (3), 82 (1994).
2. V. I. Vorotnikov, Dokl. Akad. Nauk **343**, 630 (1995) [Phys. Dokl. **40**, 146 (1995)].
3. V. I. Vorotnikov, *Partial Stability and Control* (Birkhauser, Boston, 1998).
4. V. I. Vorotnikov, Dokl. Akad. Nauk **373**, 194 (2000) [Dokl. Phys. **45**, 345 (2000)].
5. V. I. Vorotnikov and V. V. Rumyantsev, *Stability and Control over a Part of Coordinates of Phase Vector for Dynamic Systems: Theory, Methods, and Application* (Nauchnyĭ Mir, Moscow, 2001).
6. N. N. Krasovskiĭ, *Game Problems for Counter-Motions* (Nauka, Moscow, 1970).
7. M. Athans and P. L. Falb, *Optimal Control* (McGraw-Hill, New York, 1966).
8. L. S. Pontryagin, V. G. Boltyanskil, R. V. Gamkrelidze, and E. F. Mishchenko, *Mathematical Theory of Optimal Processes* (Nauka, Moscow, 1983; Gordon and Breach, New York, 1986).
9. F. L. Chernous'ko, Izv. Akad. Nauk, Tekh. Kibern., No. 1, 209 (1993).
10. V. I. Vorotnikov, *Stability of Dynamic Systems with Respect to a Part of Variables* (Nauka, Moscow, 1991).
11. V. V. Rumyantsev and A. S. Oziraner, *Stability and Stabilization of Motion with Respect to a Part of Variables* (Nauka, Moscow, 1987).
12. A. L. Fradkov, I. V. Miroshnik, and V. O. Nikiforov, *Nonlinear and Adaptive Control of Complex Systems* (Kluwer, Dordrecht, 1999).
13. A. Miele, T. Wang, and W. W. Melvin, J. Optim. Theory Appl. **49** (1), 1 (1986).
14. G. Leitmann and S. Pandey, J. Optim. Theory Appl. **70** (1), 25 (1991).
15. N. D. Botkin, M. A. Zarkh, V. M. Keĭn, *et al.*, Izv. Akad. Nauk, Tekh. Kibern., No. 1, 68 (1993).

Translated by V. Chechin

Doklady Physics, Vol. 46, No. 12, 2001, pp. 881–884. Translated from Doklady Akademii Nauk, Vol. 381, No. 4, 2001, pp. 492–495.

MECHANICS

On Equivalence of Ideal and Fictitious Porous Media

N. M. Dmitriev and V. M. Maksimov

Presented by Academician S.S. Grigoryan June 16, 2001

Received June 29, 2001

To describe filtration characteristics of porous media, mathematical models are employed in which actual porous media are represented as systems of capillaries, cracks, packings of spheres, etc. [1–3]. Among the most popular theoretical schemes allowing one to calculate the filtration characteristics of a medium are the representations of the void space in porous media as a set of parallel capillaries (ideal porous medium) or as a packing of spheres with a fixed diameter (fictitious porous medium). Apparently these models specify two types of porous media with different linear scales characterizing the void space, namely, sphere diameter D and capillary diameter d. At the same time, to solve various problems of underground hydromechanics, such as the determination of the saturation jump, the Reynolds number, etc., the concept of effective capillary diameter is used [4, 5]. That is why, for the model of a fictitious porous medium, the problem of determination of the effective capillary diameter or, more generally, the ideal porous medium with equivalent filtration characteristics arises. The solution establishing the equivalence of such media, which was proposed earlier and is widely used now, as well as the Kozeny relationship between the diameters of a sphere and capillary [6, 7], does not take into account the structure of the volume occupied by pores. The analysis of the filtration characteristics performed both for ideal and fictitious media demonstrates certain ambiguity in determination of the equivalent capillary diameter. At the same time, the Kozeny relationship involves the structure factors [8], and the equivalence of ideal and fictitious media can be established not only through the equality of porosity and permeability but of the Carman numbers and structure factors as well. However, the increase in the number of fitting parameters in the relationships establishing the equivalence of such media leads to anisotropy of characteristics when we convert the fictitious medium to an ideal one.

In the present paper, we demonstrate that the structure factors characterizing the shape of grains and the cross-sectional porosity are not the constant and universal characteristics of a medium. In the case of two-parameter models of the ideal medium, the value of relative cross-sectional porosity coincides with the dimension of space occupied by pores, whereas the structure factor related to the grain shape is equal to two. We find the relationships and conditions under which the ideal and fictitious media can be treated as equivalent with respect to a certain set of parameters. These results make more clear the axiomatics of hydromechanics of underground flows and allow, in particular, for a more adequate interpretation and comparison of experimental data for the systems modeling ideal and fictitious porous media.

1. AMBIGUITY AND GENERALIZATIONS OF EQUIVALENCE FOR IDEAL AND FICTITIOUS POROUS MEDIA

The simplest capillary model of the ideal porous medium is represented as a three-dimensional periodic array formed by three mutually perpendicular systems of capillaries [9]. In general case, each system of capillaries can have its own value of diameter d_α and packing period a_α, $\alpha = 1, 2, 3$, and it can model both isotropic and anisotropic porous media. The specified periodic structure with fixed dimensions allows one to easily calculate the parameters characterizing the geometry and filtration characteristics of the model system [8]. For an ideal porous medium, permeability k_α along the principal direction of the permeability tensor, which coincides with the direction of the αth pipe system, porosity m, cross-sectional porosity s_α, defined as the ratio of the flow section at the unit cell face to the total area of this face, and specific pore-surface area Σ per unit volume are equal, respectively, to

$$k_\alpha = \frac{\pi d_\alpha^4}{128 a_\beta a_\gamma}, \quad m = \frac{\pi d_i^2 \alpha_i}{a_1 a_2 a_3},$$
$$s_\alpha = \frac{\pi d_\alpha^2}{4 a_\beta a_\gamma}, \quad \Sigma = \frac{\pi d_i a_i}{a_1 a_2 a_3}. \tag{1}$$

Gubkin State Academy of Oil and Gas, Leninskiĭ pr. 65, Moscow, 117917 Russia
Institute of Oil and Gas Problems, Russian Academy of Sciences, ul. Gubkina 3, Moscow, 117296 Russia

1028-3358/01/4612-0881$21.00

In relationships (1) and further on, Greek letters in the subscripts denote the number of the channel system; repeating Latin subscripts imply summation, whereas there is no summation over Greek subscripts. Greek subscripts form the cyclic permutation of numbers 1, 2, and 3.

Relationships (1) provide an opportunity not only to calculate material parameters of the medium, but also to determine the relationships between them. For example, it is possible to derive the generalized Kozeny–Carman formula, $k_\alpha = \frac{m^3}{c_\alpha \Sigma^2}$, where $c_\alpha = f_\alpha \varphi_\alpha$ is the product of structure factors f_α and φ_α characterizing the shape and cross-sectional porosity. The latter factor is defined as the ratio of bulk porosity and cross-sectional porosity, $\varphi_\alpha = \frac{m}{s_\alpha}$. For the ideal isotropic medium, the structure factors are determined by formulas [8]

$$f_\alpha = 2\frac{(1 + d_{\alpha\beta}^2 + d_{\alpha\gamma}^2)^2}{(1 + d_{\alpha\beta}^3 + d_{\alpha\gamma}^3)^2},$$
$$\varphi_\alpha = \frac{m}{s_\alpha} = 1 + d_{\alpha\beta}^2 + d_{\alpha\gamma}^2, \quad (2)$$

where $d_{\alpha\beta} = \frac{d_\alpha}{d_\beta}$. Note that in the Kozeny–Carman theory c_α is represented in the form of the product of the factor characterizing the shape of grains and the factor squared related to the sinuosity of channels. In the generalized formula, we have a factor characterizing the cross-sectional porosity rather than the sinuosity factor squared.

Now let us determine the filtrational and capacitive parameters for the fictitious porous medium. We assume that all packings have isotropic filtration characteristics. For most close packings of spheres, the porosity ranges from 0.259 to 0.476 [1]. As the void area in the definition of the cross-sectional porosity, we can take the cross section for the fluid flow in the narrowest place of the channel formed by pores. Then the above range for theoretical porosity corresponds to the theoretical cross-sectional porosity in the $0.0931 \le s \le 0.2146$ range. The porosity and the cross-sectional porosity are independent of the sphere diameter and are related to each other. The following expressions were proposed to approximate the dependence of s on m [1, 10]

$$s = 0.61m^{1.4}, \quad s = 0.56m - 0.052. \quad (3)$$

The specific surface area and permeability are determined by the relationships

$$\Sigma = \frac{6(1-m)}{D}, \quad k = \frac{m^3}{c\Sigma^2}. \quad (4)$$

The Carman number c was initially assumed to be the same for all isotropic media and equal to five. However, further studies revealed that c is not a universal constant: for porosity ranging from 0.34 to 0.459, it takes on values within the 4.5–5.1 range (experiment [6]), or for porosity ranging from 0.4 to 0.6, it changes from 4.54 to 7.22 (calculations [11]). Hence, if we take $c = f\varphi$ and the factor of cross-sectional porosity

$$\varphi = 1.64m^{-0.4} \quad (5)$$

[the latter expression follows from the first relationship in (3)], then we can also assume that f and consequently c can be represented in the form similar to (5). Thus, using the experimental data for c, we can approximate the Carman number and the grain shape factor by the following expressions

$$c = 7.3m^{0.45}, \quad f = 4.45m^{0.85}. \quad (6)$$

To determine the equivalent (effective) capillary diameter in the fictitious porous medium, we shall transform the formulas for permeability. In the formula, for the fictitious medium, we substitute the expression for the specific surface area, whereas for the ideal medium, we express the cross-sectional porosity in terms of the bulk porosity and the cross-sectional porosity factor

$$k = \frac{m^3 D^2}{36c(1-m)^2}, \quad k_\alpha = \frac{d_\alpha^2}{32}\frac{m}{\varphi_\alpha}.$$

Then we assume that the values of permeability and porosity in the ideal and fictitious media are equal, equate the expressions written above, and thus find

$$d_\alpha = \frac{2}{3}\frac{\sqrt{2\varphi_\alpha}}{\sqrt{c}}\frac{m}{1-m}D. \quad (7)$$

Expression (7) is the generalized Kozeny formula, which establishes the relation between the diameters of capillary and sphere in ideal and fictitious media with the same permeability and porosity. At $2\varphi_\alpha = c$, expression (7) transforms to the usual Kozeny formula. This fact is not accidental. In the framework of the Kozeny–Carman theory, both the grain shape factor and the Carman number are assumed to have a universal value equal to two. Therefore, $2\varphi_\alpha$ is interpreted as the Carman number, and equality $2\varphi_\alpha = c$ is assumed to be met in (7) identically for all isotropic media. However, relationship (2) implies that the grain-shape factor is not a constant. Furthermore, even if we do not assume the universality of the Carman number, relationships (6) lead to the two-parameter fictitious medium, whereas the model of ideal isotropic medium can have two, three, and four parameters. In fact, all filtrational and capacitive characteristics of the fictitious medium are determined by specifying two parameters (for example, m and D), while the ideal medium is determined in a general case by six parameters (for example, d_i and a_i,

$i = 1, 2, 3$). However, the isotropy condition imposes two constraints $k_1 = k_2 = k_3$, and the ideal isotropic medium is described, in general, by four parameters. Then, if we demand the equality of diameters for two capillary systems, we get the three-parameter model of the ideal isotropic medium. If, in addition, all diameters and periods are taken to be equal, we have the two-parameter model. The two-parameter model can be not only three-dimensional isotropic, but also ultimately anisotropic two-dimensional and even one-dimensional. For the two-dimensional ultimately anisotropic model, the diameter of one capillary system should be put equal to zero, and for the one-dimensional system we have zero diameters for two capillary systems. Therefore, to establish the equivalence between ideal and fictitious media and to determine the relation between the diameter of capillaries and spheres, we must analyze all aforementioned versions.

Expression (7) takes the following form after substituting into it the first relationship from (6)

$$d_\alpha = \frac{0.35\sqrt{\varphi_\alpha}m^{0.775}}{1-m}D. \quad (8)$$

As follows from (1) and (2), the values of structural coefficient φ_α for two-dimensional models are equal to 1, 2, and 3 for one-dimensional, ultimately anisotropic two-dimensional, and three-dimensional isotropic models of an ideal porous medium, respectively. Note that the cross-sectional porosity factor can be interpreted as the ratio of characteristic scales involved in the surface and bulk averaging. Then, for two-parameter models of the ideal porous medium, it follows from the data under discussion that such a ratio depends on the dimension of void space and is equal to it. For all versions of two-parameter models, the value of the grain shape factor is equal to two. Substituting the listed values of φ_α into relationship (8), we obtain the corresponding formulas relating the diameters of capillaries and spheres. However, for two-parameter models of an ideal porous medium, the values of the Carman number do not coincide with its values for fictitious media. Thus, the equivalence between the ideal and fictitious media in the two-parameter models is possible only with respect to the porosity and permeability, while the values of their specific surface area and the Carman number will not coincide.

For the three-parameter model of the ideal medium, the equivalence relationships between the ideal and fictitious media can be established by putting k, m, and c to be equal. In this case, the equivalent media will also have equal specific surface areas, but the isotropic ideal medium equivalent with respect to the permeability will have other diameters of capillaries. Similarly, for the four-parameter model of the ideal medium, we can choose not only k and m but also the values of structure factors φ and f to be equal to those for the fictitious medium. However, equalities $\varphi = \varphi_\alpha$ and $f = f_\alpha$ can be met only for a single capillary system; two other systems will have different values of φ_α, f_α, and capillary diameters. Thus, for a three- and four-parameter model of ideal isotropic medium, we can make permeability, porosity, and specific surface area (the Carman number) to be equal to those in the fictitious medium, but the values of the capillary diameters will be different in equivalent ideal media. The difference in the capillary diameters leads to a contradiction. In fact, all filtrational characteristics of the fictitious medium are considered *a priori* as isotropic, whereas in equivalent ideal media the evaluated parameters can depend on the chosen direction.

2. METHODOLOGICAL CONSEQUENCES OF THE PRESENTED GENERALIZATIONS

To illustrate the previous discussion, we consider formulas for the Reynolds number and the capillary pressure jump. In the derivation of relationships for the filtrational Reynolds number, one uses the hydraulic formula $\mathrm{Re} = \frac{vd\rho}{\mu}$, where v is the average velocity, d is the pipe diameter (characteristic linear dimension), and ρ and μ are the fluid density and viscosity, respectively. In the case of filtrational Reynolds number, the average velocity is replaced by the filtration rate $w = sv$ and the characteristic linear dimension is taken to be equal to the sphere diameter for fictitious media and to the capillary diameter for ideal media. As a result, we find the following relationships

$$\mathrm{Re}_\alpha = \frac{wd_\alpha\rho}{\mu s_\alpha}, \quad \mathrm{Re} = \frac{wD\rho}{\mu s}. \quad (9)$$

If we substitute the cross-sectional porosity expressed in terms of bulk porosity and the capillary diameter expressed in terms of filtrational characteristics, we obtain the formulas

$$\mathrm{Re}_\alpha = \frac{\sqrt{32k}\varphi_\alpha^{1.5}w\rho}{m^{1.5}\mu}, \quad \mathrm{Re} = \frac{wD\rho}{\mu(0.56m - 0.052)}. \quad (10)$$

Thus, for the equivalent ideal medium, we have three different formulas corresponding to the isotropic Reynolds number in the fictitious medium. A similar situation also takes place for the formula determining the capillary pressure jump p_k, which is based on the Laplace formula and its generalization for the capillary model

$$p_k = \alpha\cos\theta\sqrt{\frac{8\varphi_\alpha m}{k}}J,$$

where α is the interphase tension coefficient, θ is the static edge wetting angle, J is the dimensionless Leverette saturation function, and the expression under square root determines the reciprocal to the capillary radius. Therefore it seems natural to consider the equivalence between the fictitious medium and the two-parameter ideal medium. Then the generalized Kozeny

formula is obtained by the substitution $\varphi_\alpha = 3$ into (7), and the ratio of specific surface areas Σ_i and Σ_f of ideal and fictitious media will be $\frac{\Sigma_i}{\Sigma_f} = 1.1\, m^{0.225}$.

The presented results make more exact the axiomatics of hydromechanics of underground flows and its applications to the ecological problems concerning the contamination of soils and underground water.

ACKNOWLEDGMENTS

The authors are grateful to Academician S.S. Grigoryan for his interest to this work and for helpful discussions.

This work was supported by the Russian Foundation for Basic Research, project no. 00-01-00609.

REFERENCES

1. L. S. Leĭbenzon, *Motion of Natural Liquids and Gases in Porous Medium* (Gostoptekhizdat, Moscow, 1947).
2. L. I. Kheĭfets and A. V. Neĭmark, *Multiple-Phase Processes in Porous Media* (Khimiya, Moscow, 1982).
3. A. E. Scheidegger, *The Physics of Flow through Porous Media* (Univ. Toronto Press, Toronto, 1974).
4. K. S. Basniev, I. N. Kochina, and V. M. Maksimov, *Underground Hydromechanics* (Nedra, Moscow, 1993).
5. P. C. Carman, *Flow of Gases through Porous Media* (Butterworths, London, 1956).
6. E. S. Romm, *Structural Models for Pore Space of Rocks* (Nedra, Leningrad, 1985).
7. S. V. Belov, *Foamed Metals in Mechanical Engineering* (Mashinostroenie, Moscow, 1981).
8. N. M. Dmitriev, Izv. Akad. Nauk, Mekh. Zhidk. Gaza, No. 4, 96 (1996).
9. D. Turcotte and G. Schubert, *Geodynamics: Applications of Continuum Physics to Geological Problems* (Wiley, New York, 1982).
10. S. S. Kutateladze, *Heat Transfer and Hydrodynamic Resistance: Reference Book* (Énergoatomizdat, Moscow, 1990).
11. J. Happel and H. Brenner, *Low Reynolds Number Hydrodynamics with Special Applications to Particulate Media* (Prentice-Hall, Englewood Cliffs, 1965).

Translated by K. Kugel

Doklady Physics, Vol. 46, No. 12, 2001, pp. 885–887. Translated from Doklady Akademii Nauk, Vol. 381, No. 4, 2001, pp. 496–498.

MECHANICS

On Sliding an Obtuse Wedge along the Boundary of a Perfectly Plastic Half-Space

R. I. Nepershin

Presented by Academician A.Yu. Ishlinskiĭ July 30, 2001

Received August 9, 2001

The self-similar solution to the unsteady problem on indentation of a wedge into a plastic half-space is well known [1]. In this study, we have solved the steady problem of a plane plastic flow for the case of sliding an obtuse wedge along the boundary of a perfectly plastic half-space. For the same geometry, the similar problem of gliding a two-dimensional plate over the surface of ideal liquid is presented in [2].

The slip-line field (satisfying the boundary conditions for stresses) for an obtuse wedge sliding with a velocity $V = 1$ over the half-space boundary in the x-direction is shown in Fig. 1. The problem parameters are the following: a tilt angle φ between the forward wedge side and the half-space boundary and the value of the contact friction μ, the latter being varied within the range

$$0 \le \mu \le \frac{1}{2}. \tag{1}$$

Here, the extension–compression yield point is taken as a characteristic stress. While sliding a plastic material downwards along the wedge boundary in the domain *OAD*, we have an acute angle γ at the point *O*. This angle is determined by the contact friction (1):

$$\gamma = \frac{1}{2}\arccos 2\mu. \tag{2}$$

If the inequality

$$\varphi \le \gamma \tag{3}$$

is fulfilled, we can construct a field of slip lines in which the domain *ABC* of the uniform stressed state (where the boundary *AB* is free of external stresses) touches the horizontal half-space boundary at a point *B*, and the two domains *ABC* and *OAD* of the uniform stressed state are connected by a centered fan of the slip lines with a singular point *A*.

Moscow State Academy of Instrumentation Engineering and Informatics,
ul. Stromynka 20, Moscow, 107846 Russia

The angle ψ of the centered fan satisfies the relationship

$$\psi = \frac{\pi}{4} + \gamma - \varphi - \theta, \tag{4}$$

where the tilt angle θ between the boundary *AB* and the half-space boundary is determined from the triangle *OAB*:

$$\sin\theta = \frac{\sin\varphi}{\sqrt{2}\sin\gamma}. \tag{5}$$

The thickness h of the plastic layer penetrating into the half-space is

$$h = l(\sin\gamma - \sin\varphi). \tag{6}$$

Using the value $\sigma = -\frac{1}{2}$ in the domain *ABC*, we find the mean stress in the domain *OAD* from the Hencky equation for α slip lines. Next, we obtain the normal pressure acting on the wedge

$$-\sigma_n = \psi + \frac{1}{2}(1 + \sin 2\gamma). \tag{7}$$

The vertical and horizontal forces acting on the wedge from the plastic domain are

$$\begin{aligned} N &= -l(\mu\sin\varphi + \sigma_n\cos\varphi), \\ F &= l(\mu\cos\varphi - \sigma_n\sin\varphi). \end{aligned} \tag{8}$$

Under condition (3), the bearing capacity of the rigid

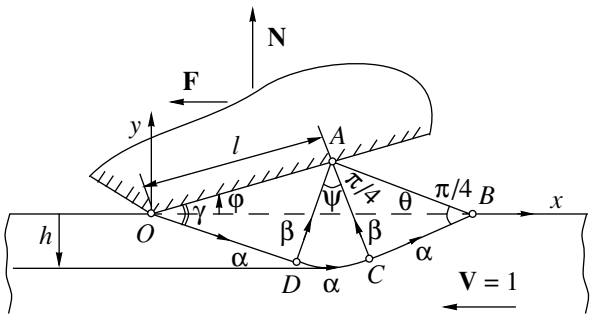

Fig. 1.

1028-3358/01/4612-0885$21.00

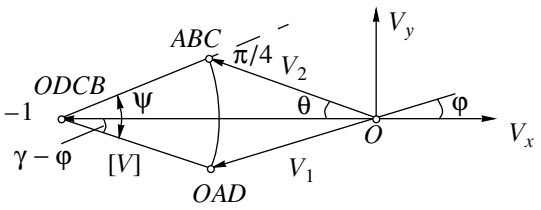

Fig. 2.

domain of the half-space with the apex at the point *O* is exactly fulfilled, with the exception only of the limiting case $\varphi = 0$ and $\mu = 0$ $\left(\gamma = \frac{\pi}{4}\right)$. This corresponds to a plane Prandtl stamp that slides along the half-space. In this case, the field of slip lines is asymmetric and the rigid domain on the left from the point *O* is loaded to provide the plastic state.

The hodograph of the plastic-flow velocity in the V_xV_y-plane is shown in Fig. 2. (V_x and V_y are the Cartesian coordinates in the plane of the velocity hodograph.) The hodograph was obtained by superimposing the velocity $V = –1$ (i.e., the reverse sliding velocity of the stamp) on the system. In this case, the stamp is proved to be immovable, and if the velocity vector in the domain *ABC* and the direction of the boundary *AB* in the physical plane are coincided (Fig. 1), the plastic flow is steady.

The value of the velocity discontinuity [*V*], which arises at the point *O* along the rigid-plastic boundary *ODCB*, and the sliding velocity V_1 of the domain *OAD* along the wedge boundary can be found from the bottom triangle of the hodograph, provided that the tilt angles φ and $\gamma – \varphi$ of the boundaries *OA* and *OD* in the physical plane are known,

$$[V] = \frac{\sin\varphi}{\cos\varphi\sin(\gamma-\varphi) + \sin\varphi\cos(\gamma-\varphi)}, \quad (9)$$

$$V_1 = [V]\frac{\sin(\gamma-\varphi)}{\sin\varphi}. \quad (10)$$

Along the boundary *ODCB*, the velocity discontinuity remains constant (Fig. 1). In the hodograph, it is mapped by a circular arc with the central angle ψ thereby determining the top triangle of the velocity hodograph and the velocity V_2 of the domain *ABC*:

$$V_2 = \frac{1-[V]\cos(\pi/4-\theta)}{\cos\theta}. \quad (11)$$

The exterior angle of the top triangle between the direction of the velocity discontinuity and the vector $\mathbf{V}_2$ equals $\frac{\pi}{4}$, since the angle between the slip line *CB* and the boundary *AB* does not vary while mapping the physical plane onto the plane of the velocity hodograph. From the relationship $\psi + \varphi – \gamma + \theta = \frac{\pi}{4}$ and Eq. (4), it follows that the tilt angle θ of the boundary *AB* in the physical plane coincides with both the tilt angle θ of its velocity vector in the hodograph plane and the plastic flow being stationary while sliding the wedge along the half-space boundary.

We find the velocity of the plastic flow in the domain *ABC* from the velocity hodograph and Eq. (4), the value of the velocity being dependent on the polar angle $0 \le \lambda \le \psi$ with the center at the point *A*:

$$V_x = \frac{[V]}{\sqrt{2}}[\cos(\theta+\lambda) + \sin(\theta+\lambda)] - 1, \quad (12)$$

$$V_y = \frac{[V]}{\sqrt{2}}[\cos(\theta+\lambda) - \sin(\theta+\lambda)]. \quad (13)$$

At $\lambda = 0$ and $\lambda = \psi$, Eqs. (12) and (13) yield projections of the velocity vectors $\mathbf{V}_2$ and $\mathbf{V}_1$, respectively.

In the domains *ABC* and *AOD*, the streamlines are the straight lines parallel to the boundaries *AB* and *OA*, respectively. In the domain *ADC*, they can be found by numerically integrating the differential equation $\frac{dy}{dx} = \frac{V_y}{V_x}$, in which the velocities are given by Eqs. (12) and (13). Due to the velocity discontinuity [*V*] on the rigid-plastic boundary, there appears a shear-strain discontinuity [γ], which is equal to the ratio of [*V*] to the normal velocity component. Using (4), (9), and (10), we derive at the intersection points of streamlines with the boundaries *BC* and *OD*

$$[\gamma]_{BC} = \frac{\sqrt{2}[V]}{\cos\theta - \sin\theta}, \quad (14)$$

$$[\gamma]_{OD} = \frac{\sin\varphi}{\sin\gamma\sin(\gamma-\varphi)}. \quad (15)$$

On the boundary *DC*, a discontinuity in the shear strain also occurs:

$$[\gamma]_{DC} = \frac{[V]}{\sin\xi}, \quad 0 < \xi < \frac{\pi}{4} - \theta, \quad (16)$$

where ξ is the tilt angle of the α slip line with respect to the *x*-axis.

Adding to the discontinuities [γ] continuous increments of strains along streamlines in the domain *ACD*, we obtain the strain distribution across the plastic-layer thickness *h* beyond the wedge. This distribution rises from the half-space boundary toward the bulk and tends to infinity at $y = –h$ as $\xi \longrightarrow 0$ in Eq. (16). If the wedge has a finite rounding radius at the point *O*, the velocity discontinuity along the rigid-plastic domain *ODCB* is replaced by a continuous change in the velocities in the vicinity of this boundary. In this case, the distribution of strains is continuous and finite. In numerically solving

the problem, it is possible to analyze the effect of the curvilinear shape of the boundary *OA* and the contact friction (1) on the distribution of plastic strains in the surface layer of thickness *h*, which is an urgent problem in the technology of the plastic surface deformation of materials.

The equality $\varphi = \gamma$ in (3) shows a limiting case of steady wedge sliding for which, as follows from Eqs. (4)–(6) and (9)–(12), $\psi = 0$, $\theta = \frac{\pi}{4}$, $h = 0$, $[V] = 1$, and $V_1 = V_2 = 0$. In front of the wedge, there appears a plastic scab of the material that slides together with the wedge along the boundary, and the velocity field is degenerated into a simple shear along the boundary with the velocity discontinuity $[V] = 1$, the plastic deformation not penetrating into the material. The equality $\varphi = \gamma$ also shows the maximum values of the tilt angle for the wedge surface *OA* for which a steady plastic flow arises. In particular, for the maximum contact friction $\mu = \frac{1}{2}$ and $\varphi = \gamma = 0$, we arrive at the case of sliding an absolutely rough plane stamp for which the plastic domain is degenerated into a shear line and the domain *ABC* is degenerated into the point *A*.

The problem under consideration is also of interest as a mechanical model of sliding friction, namely, the interaction between a solid microroughness and a soft plastic material. Here, a ratio of the forces *F* and *N* can be treated as a local coefficient *f* of the sliding friction

$$f = \frac{\mu\cos\varphi - \sigma_n\sin\varphi}{-\mu\sin\varphi - \sigma_n\cos\varphi}, \tag{17}$$

where $-\sigma_n$ is the normal pressure exerted on the wedge (7). As is seen from Eq. (17), the friction coefficient depends on the parameters φ and μ and is independent of the normal reaction *N* of the bearing surface until the contact length *l* between the wedge and the plastic domain attains a certain critical value for a given microroughness. In the case of an ideally smooth microroughness ($\mu = 0$), expression (17) takes the form

$$f = \tan\varphi \tag{18}$$

and the tilt angle of the wedge is interpreted as the sliding-friction angle.

REFERENCES

1. R. Hill, *The Mathematical Theory of Plasticity* (Clarendon, Oxford, 1985).
2. L. I. Sedov, *Mechanics of Continuous Medium* (Nauka, Moscow, 1973), Vol. 2.

Translated by Yu. Vishnyakov

Doklady Physics, Vol. 46, No. 12, 2001, pp. 888–889. Translated from Doklady Akademii Nauk, Vol. 381, No. 5, 2001, pp. 614–615.

MECHANICS

A New Integrable Case on *so*(4)

A. V. Borisov, I. S. Mamaev**, and V. V. Sokolov***

Presented by Academician Ya.G. Sinaĭ July 26, 2001

Received August 22, 2001

Recently, Sokolov considered a new case of integrability for Kirchhoff equations with an additional integral of the fourth degree [1]. In the present study, we propose the most natural form for this integral and also generalize it to the form of the Poisson-bracket bundle

$$\{M_i, M_j\} = \varepsilon_{ijk}M_k,$$
$$\{M_i, \gamma_j\} = \varepsilon_{ijk}\gamma_k, \quad \{\gamma_i, \gamma_j\} = x\varepsilon_{ijk}M_k, \tag{1}$$

where x is an arbitrary parameter. For this bundle, we consider a system of equations with the quadratic Hamiltonian

$$H = \frac{1}{2}(\mathbf{A}M, M) + (\mathbf{B}M, \gamma) + \frac{1}{2}(\mathbf{C}\gamma, \gamma).$$

Here the matrix $\mathbf{A}$ can always be chosen diagonal: $\mathbf{A} = \mathrm{diag}(a_1, a_2, a_3)$. The matrix $\mathbf{C} = \|c_{ij}\|$ is a symmetric matrix, and the matrix $\mathbf{B} = \|b_{ij}\|$, generally speaking, is arbitrary. The Casimir functions for the bundle are

$$F_1 = x(M, M) + (\gamma, \gamma), \quad F_2 = (M, \gamma). \tag{2}$$

For $x = 0$, the corresponding dynamic system of equations coincides with the classical Kirchhoff equations. In the case $x = 1$, this system coincides with the Poincaré equations on *so*(4), which describe the motion of a body with cavities filled with a vortex incompressible fluid. Moreover, the Poincaré equations describe the motion of a four-dimensional gyroscope. It turns out that in the case when the Hamiltonian taken from [1] is written out in the form

$$H = \frac{1}{2}(M_1^2 + M_2^2 + 2M_3^2)$$
$$+ M_3(\alpha\gamma_1 + \beta\gamma_2) - \frac{1}{2}(\alpha^2 + \beta^2)\gamma_3^2, \tag{3}$$

where α and β are arbitrary constants, this Hamiltonian has an additional integral

$$F = k_1, k_2,$$
$$k_1 = M_3,$$
$$k_2 = M_3(M_1^2 + M_2^2 + M_3^2 + x(\beta M_1 - \alpha M_2)^2)$$
$$+ 2(\alpha M_1 + \beta M_2)(M_1\gamma_1 + M_2\gamma_2)$$
$$+ 2M_3^2(\alpha\gamma_1 + \beta\gamma_2) + M_3(\alpha\gamma_1 + \beta\gamma_2)^2$$
$$- (\alpha^2 + \beta^2)(2M_1\gamma_1 + 2M_2\gamma_2 + M_3\gamma_3)\gamma_3 \tag{4}$$

on the bundle of Poisson brackets. To obtain the integral given in [1] for the case of $x = 0$ [that corresponds to the $e(3)$ algebra], it is necessary to perform the linear transformation of the form $\gamma = \gamma$, namely,

$$\overline{M}_1 = M_1 + \frac{1}{3}\alpha\gamma_3,$$
$$\overline{M}_2 = M_2 + \frac{1}{3}\beta\gamma_3, \quad \overline{M}_3 = M_3 - \frac{1}{3}\alpha\gamma_1 - \frac{1}{3}\beta\gamma_2,$$

which conserves the $e(3)$ structure. In the new variables, Hamiltonian (3) has the form

$$H = \frac{1}{2}(\overline{M}_1^2 + \overline{M}_2^2 + 2\overline{M}_3^2) + \bar{\alpha}(\overline{M}_3\gamma_1 + \overline{M}_1\gamma_3)$$
$$+ \bar{\beta}(\overline{M}_3\gamma_2 + \overline{M}_2\gamma_3) - 2(\bar{\alpha}^2 + \bar{\beta}^2)\gamma_3^2 + 2(\bar{\beta}\gamma_1 - \bar{\alpha}\gamma_2)^2,$$
$$\bar{\alpha} = \frac{1}{3}\alpha_1, \quad \bar{\beta} = \frac{1}{3}\beta.$$

This form is identical to the formula derived in [1] with the accuracy to the Casimir function. It is easy to verify that the following equalities are valid for the functions k_1 and k_2:

$$\dot{k}_1 = -2(\beta\gamma_1 - \alpha\gamma_2)k_1, \quad \dot{k}_2 = 2(\beta\gamma_1 - \alpha\gamma_2)k_2; \tag{5}$$

i.e., $k_1 = 0$ and $k_2 = 0$ are invariant relationships. It should be noted that if, in the Lagrange and Hess cases, the linear relations of the type $k_1 = M_3 = 0$ exist for the Euler–Poisson equations, then no cubic invariant relations apparently arose in dynamics of solids until now. We dwell in brief on the explicit calculation of the Kovalevskaya exponents. It is easy to verify that the dynamical system with Hamiltonian (3) and Poisson brack-

* *Landau Institute for Theoretical Physics, Russian Academy of Sciences, ul. Kosygina 2, Moscow, 117940 Russia*

** *Science Publishing Center "Regular and Chaotic Dynamics," ul. Universitetskaya 1, Izhevsk, 426034 Russia*

ets (1) has exactly two one-parameter families of solutions in the form

$$M_i = X_i t^{-1}, \quad \gamma_i = Y_i t^{-1}.$$

The former is given by the formulas

$$X_3 = Y_3 = 0, \quad Y_1^2 + Y_2^2 = 0,$$
$$2\alpha Y_2 - 2\beta Y_1 = 1, \quad X_1 = 2X_2(\alpha Y_1 + \beta Y_2).$$

For the latter family of solutions, we have

$$X_1 = \alpha Y_3, \quad X_2 = \beta Y_3, \quad X_3 = -\alpha Y_1 - \beta Y_2,$$
$$(1 + x(\alpha^2 + \beta^2))(Y_1^2 + Y_2^2 + Y_3^2) = \frac{x}{4},$$
$$2\alpha Y_2 - 2\beta Y_1 = -1.$$

For both families, the Kovalevskaya exponents are given by the formula {–1, 0, 1, 2, 2, 2} that agrees well with the test confirming the absence of other singularities in the complex time plane except poles (the Kovalevskaya method). As to the above case, the possibility of both multidimensional generalizations and an addition of linear, in particular, gyroscopic terms remains unclear. For them, no topological analysis was carried out and no explicit solution was obtained. Until now, no Lax pair was found, and the cases were studied using neither qualitative nor computer methods. Apparently, this will be realized in the nearest future.

HISTORICAL COMMENT

The integral of the fourth degree for the Kirchhoff equations [on *e*(3)] was found by Chaplygin under an additional condition $(M, \gamma) = 0$ [2]. On *so*(4), the corresponding (particular) family was determined by Bogoyavlenskiĭ [3]. A case of the general integrability of *so*(4) with an integral of the fourth degree was analyzed by Adler and van Moerbeke [4]. The *L–A* pair for this case was constructed by Reyman and Semenov-Tian-Shansky [5]. Case (3) on the Poisson bracket bundle is likely reduced to none of these cases and seems to be substantially new. First of all, this is associated with the nature of the additional integral, which is a product of two invariant relations. We also note that, for the Kovalevskaya and Bogoyavlenskiĭ cases [2, 3], the additional integral can be represented in the form $F = k_1^2 + k_2^2$, where k_1 and k_2 are quadratic functions, their common level defining a certain invariant manifold. For the Kovalevskaya case, such a manifold corresponds to the Delauney solution. The conditions for the existence of algebraic integrals in the case of Kirchhoff equations was studied by Liouville, who has published in [6] certain necessary conditions for the case of the off-diagonal matrix **B**. He has also promised to present in subsequent studies the corresponding integrals of a degree higher than the second one. However, these publications have not appeared. In recent investigations of the algebraic integrability, it was assumed beforehand that all the matrices **A**, **B**, and **C** are diagonal matrices [7]. In [8, 9], the matrix **A** was assumed to be determined by the inertia matrix **I** of an actual solid ($\mathbf{A} = \mathbf{I}^{-1}$), whereas all the moments of inertia are different. Only in this case do there exist unstable periodic solutions (permanent rotations) and their separatrices playing the key role in the relevant proofs.

ACKNOWLEDGMENTS

One of the authors of this study (V.V. Sokolov) was supported by the Russian Foundation for Basic Research, project no. 99-01-00294 and by the INTAS, grant no. 1782.

REFERENCES

1. V. V. Sokolov, Teor. Mat. Fiz. **129** (1), 31 (2001).
2. S. A. Chaplygin, in *New Particular Solution to Problems of Rotation of Heavy Solid around a Fixed Point*, in *Collection of Papers* (Gostekhteorizdat, Moscow, 1948), Vol. 1, pp. 125–132.
3. O. I. Bogoyavlenskiĭ, *Tip-Over Solitons, Nonlinear Integrable Equations* (Nauka, Moscow, 1991).
4. M. Adler and P. van Moerbeke, Adv. Math., Suppl. Stud. **9**, 81 (1986).
5. A. G. Reyman and M. A. Semenov-Tian-Shansky, Commun. Math. Phys. **105**, 461 (1986).
6. R. Liouville, C. R. Acad. Sci., Ser. 2, 874 (1896).
7. S. T. Sadetov, Vestn. Mosk. Univ., Ser. Mat., Mekh., No. 3, 56 (1990).
8. V. V. Kozlov and D. A. Onishchenko, Dokl. Akad. Nauk SSSR **266**, 1298 (1982).
9. A. V. Borisov, Reg. Chaot. Dyn. **1** (2), 61 (1996).

Translated by V. Bukhanov

Doklady Physics, Vol. 46, No. 12, 2001, pp. 890–896. Translated from Doklady Akademii Nauk, Vol. 381, No. 5, 2001, pp. 616–622.

MECHANICS

On Characteristic Relations for Stresses and Displacement Velocities: A Case of the Spatial Problem for a Perfectly Plastic Body Satisfying the Condition of Full Plasticity

D. D. Ivlev*, Academician A. Yu. Ishlinskiĭ, and R. I. Nepershin*****

Received August 9, 2001

In this paper, we derive characteristic relations for stresses and displacement velocities. These relations correspond to hyperbolic equations inherent in the spatial problem of the perfect-plasticity theory. The equations are applied to an isotropic incompressible body that satisfies the condition of full plasticity [1, 2]. We show as well that relations concerning the plane and axisymmetric problems represent ultimate cases of the spatial problem. We also consider other problems associated with pressure being exerted by smooth plane dies of triangular, rectangular, and elliptic shapes onto a perfectly plastic half-space.

1. The tensile–compressive yield stress of a material is considered as a characteristic stress. Then the full-plasticity condition in the space of principal stresses takes the form

$$\sigma_1 = \sigma_2, \quad \sigma_3 = \sigma_1 \pm 1. \tag{1.1}$$

Under condition (1.1), the spatial problem of perfect-plasticity theory is statically determinate and hyperbolic. Its characteristic cone, whose axis coincides with the direction of the principal stress σ_3, is tangential to slip surfaces inclined with respect to the direction of σ_3 at angles $\pm\frac{\pi}{4}$ [1].

In the Cartesian $\{x, y, z\}$ coordinate system, let the direction of σ_3 be given by the unit vector $\mathbf{n}$ with the components

$$n_1 = \sin\theta\cos\psi, \quad n_2 = \sin\theta\sin\psi, \quad n_3 = \cos\theta. \tag{1.2}$$

Here, the angles θ and ψ are formed by the z-axis and the vector $\mathbf{n}$ and by the x-axis and the projection of the vector $\mathbf{n}$ onto the plane $\{x, y\}$, respectively. The stress-tensor components satisfying condition (1.1) are expressed as

$$\sigma_x = \sigma \mp \frac{1}{3} \pm n_1^2, \quad \sigma_y = \sigma \mp \frac{1}{3} \pm n_2^2, \quad \sigma_z = \sigma \mp \frac{1}{3} \pm n_3^2, \tag{1.3}$$

$$\tau_{xy} = \pm n_1 n_2, \quad \tau_{yz} = \pm n_2 n_3, \quad \tau_{zx} = \pm n_3 n_1, \tag{1.4}$$

where σ is the average stress. The unit vectors $\mathbf{m}$ and $\mathbf{l}$, which specify the directions of the principal stresses σ_1 and σ_2, respectively, satisfy the relations

$$\mathbf{m}\cdot\mathbf{l} = 0, \quad \mathbf{m}\cdot\mathbf{n} = 0, \quad \mathbf{l}\cdot\mathbf{n} = 0, \quad \mathbf{m} = \mathbf{l}\times\mathbf{n}, \quad \mathbf{l} = \mathbf{n}\times\mathbf{m}. \tag{1.5}$$

We now consider a curvilinear orthogonal coordinate system $\{\alpha, \beta, \gamma\}$ with the unit direction vectors $\boldsymbol{\alpha}$ and $\boldsymbol{\beta}$ along the slip lines of the first and second families. The direction of the algebraically largest principal stress lies between these lines. The direction vector of the coordinate line γ, which is orthogonal to these lines, coincides with the vector $\mathbf{l}$. The vectors $\boldsymbol{\alpha}$ and $\boldsymbol{\beta}$ satisfy the relations

$$\boldsymbol{\alpha}\cdot\mathbf{n} = \frac{\sqrt{2}}{2}, \quad \boldsymbol{\alpha}\cdot\mathbf{m} = \frac{\sqrt{2}}{2}, \quad \boldsymbol{\alpha}\cdot\mathbf{l} = 0, \tag{1.6}$$

$$\boldsymbol{\beta}\cdot\mathbf{n} = \pm\frac{\sqrt{2}}{2}, \quad \boldsymbol{\beta}\cdot\mathbf{m} = \mp\frac{\sqrt{2}}{2}, \quad \boldsymbol{\beta}\cdot\mathbf{l} = 0. \tag{1.7}$$

If the vectors $\mathbf{n}$ and $\mathbf{m}$ are known, then Eqs. (1.5)–(1.7) determine the coordinate system $\{\alpha, \beta, \gamma\}$. Under full-plasticity condition (1.1), the stress tensor is deter-

* *Chuvash State Pedagogical University, ul. Karla Marksa 38, Cheboksary, 428000 Russia*
** *Institute for Problems in Mechanics, Russian Academy of Sciences, pr. Vernadskogo 101, Moscow, 117526 Russia*
*** *Moscow State Academy of Instrumentation Engineering and Informatics, ul. Stromynka 20, Moscow, 107846 Russia*

1028-3358/01/4612-0890$21.00

mined in this coordinate system by the symmetric matrix

$$\sigma_{ij} = \begin{bmatrix} \sigma \pm \frac{1}{6} & \frac{1}{2} & 0 \\ \frac{1}{2} & \sigma \pm \frac{1}{6} & 0 \\ 0 & 0 & \sigma \mp \frac{1}{3} \end{bmatrix}. \quad (1.8)$$

Taking the rotation angles for tangents to the α-, β-, and γ-lines as curvilinear coordinates, we obtain differentials for arcs of these coordinate lines, the differentials being related to their radii of curvature R_α, R_β, and R_γ by the formulas

$$dS_\alpha = R_\alpha d\alpha, \quad dS_\beta = R_\beta d\beta, \quad dS_\gamma = R_\gamma d\gamma. \quad (1.9)$$

From this, it follows that the curvature radii of the coordinate lines under consideration represent their Lamé parameters. In the {α, β, γ} coordinate system, the differential equilibrium equations written out in terms of stress tensor (1.8) take the form

$$\frac{\partial \sigma}{\partial S_\alpha} + \frac{\partial \ln R_\alpha}{\partial S_\beta} + \frac{1}{2}\left(\pm\frac{\partial \ln R_\gamma}{\partial S_\alpha} + \frac{\partial \ln R_\gamma}{\partial S_\beta}\right) = 0, \quad (1.10)$$

$$\frac{\partial \sigma}{\partial S_\beta} + \frac{\partial \ln R_\beta}{\partial S_\alpha} + \frac{1}{2}\left(\pm\frac{\partial \ln R_\gamma}{\partial S_\beta} + \frac{\partial \ln R_\gamma}{\partial S_\alpha}\right) = 0, \quad (1.11)$$

$$\frac{\partial}{\partial S_\gamma}\left(\sigma \mp \frac{1}{2}(\ln R_\alpha + \ln R_\beta)\right) = 0. \quad (1.12)$$

Since the coordinate lines α, β, and γ are orthogonal, the principal normals to them lie in the planes tangent to the surfaces γ = const, α = const, and β = const. Therefore, being calculated along the α-, β-, and γ-lines in a small vicinity of the point under consideration, differentials for the radii of curvature of the coordinate lines can be represented by the expressions that, in the tangent planes, have the form (Fig. 1)

$$\begin{aligned} (dR_\gamma)_\alpha &= dS_\alpha \cos\varphi_\alpha, \\ (dR_\gamma)_\beta &= -dS_\beta \sin\varphi_\alpha \text{ for } \gamma = \text{const}; \end{aligned} \quad (1.13)$$

$$\begin{aligned} (dR_\alpha)_\beta &= dS_\beta \cos\varphi_\beta, \\ (dR_\alpha)_\gamma &= -dS_\gamma \sin\varphi_\beta \text{ for } \alpha = \text{const}; \end{aligned} \quad (1.14)$$

$$\begin{aligned} (dR_\beta)_\gamma &= dS_\gamma \cos\varphi_\gamma, \\ (dR_\beta)_\alpha &= -dS_\alpha \sin\varphi_\gamma \text{ for } \beta = \text{const}. \end{aligned} \quad (1.15)$$

Here, φ_α, φ_β, and φ_γ correspond to the angles between negative directions of the principal normals to the γ-, α-, and β-lines and the tangents to the α-, β-, and γ-lines, respectively. Substituting expressions (1.13)–(1.15) into equilibrium equations (1.10)–(1.12), we arrive at the following differential relationships:

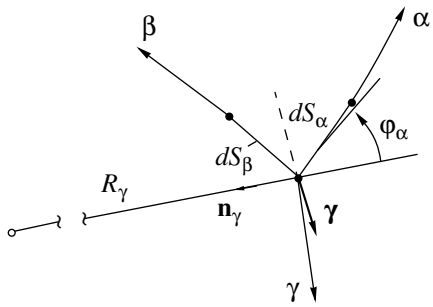

Fig. 1. Slip lines α, β and the direction of the principal normal $\mathbf{n}_\gamma$ in the plane tangential to the surface γ = const.

$$\begin{aligned} &d\sigma + d\alpha\cos\varphi_\beta \\ &= \frac{dS_\alpha}{2R_\gamma}(\mp\cos\varphi_\alpha + \sin\varphi_\alpha) \text{ along } \alpha, \end{aligned} \quad (1.16)$$

$$\begin{aligned} &d\sigma - d\beta\sin\varphi_\gamma \\ &= \frac{dS_\beta}{2R_\gamma}(\pm\sin\varphi_\alpha - \cos\varphi_\alpha) \text{ along } \beta, \end{aligned} \quad (1.17)$$

$$d\sigma = \pm\frac{dS_\gamma}{2}\left(\frac{\cos\varphi_\gamma}{R_\beta} - \frac{\sin\varphi_\beta}{R_\alpha}\right) \text{ along } \gamma, \quad (1.18)$$

which are valid along the α-, β-, and γ-lines. If the surface γ = const is flat, then $\varphi_\beta = \pi$ and $\varphi_\gamma = -\frac{\pi}{2}$. In this case, σ = const along the surface γ. If, in a small vicinity of the point under consideration, the surface γ = const is close to the tangential plane, then $\varphi_\beta = \pi + d\varphi_\beta$ and $\varphi_\gamma = -\frac{\pi}{2} - d\varphi_\gamma$. In this case, as a result of using expressions (1.9), relationship (1.18) takes the form

$$d\sigma = \mp\frac{dS_\gamma}{2}\left(\frac{d\alpha d\varphi_\beta}{dS_\alpha} + \frac{d\beta d\varphi_\gamma}{dS_\beta}\right) \text{ along } \gamma. \quad (1.19)$$

At small rotation angles of the tangents to the α- and β-lines, the right-hand side of equation (1.19), which contains products of small quantities, is close to zero. Therefore, $\sigma \approx \text{const}$ along γ, $\cos\varphi_\beta \approx -1$, $\sin\varphi_\gamma \approx -1$, and $d\alpha \approx d\beta \approx d\varphi_\alpha$. Using the notation $\varphi_\alpha = \varphi$, relations (1.16) and (1.17) take the form

$$d\sigma - d\varphi = \frac{dS_\alpha}{2R_\gamma}(\mp\cos\varphi + \sin\varphi) \text{ along } \alpha, \quad (1.20)$$

$$d\sigma + d\varphi = \frac{dS_\beta}{2R_\gamma}(\pm\sin\varphi - \cos\varphi) \text{ along } \beta. \quad (1.21)$$

In the case of $\frac{1}{R_\gamma} = 0$, these relations turn into Hencky's equations for the plane strain. If all the planes $\gamma = \text{const}$ pass through the z-axis, then expressions (1.20)–(1.21) coincide with those for stresses corresponding to the axisymmetric strain [3]. Thus, if smooth surfaces $\gamma = \text{const}$ satisfying the boundary conditions of the problem are known, then spatial slip surfaces can be found by integration of equations (1.6), (1.7) for the characteristic curves and characteristic relations (1.20), (1.21) on the surface $\gamma = \text{const}$ by methods similar to those used when solving the plane and axisymmetric problems of perfect plasticity [1, 3, 4].

2. After the slip surfaces have been determined, we can find the field of the displacement velocities u, v, w from the incompressibility and isotropy conditions [2]. We consider the local $\{\alpha, \beta, \gamma\}$ coordinate system in which the angles θ and ψ, which determine the direction of the stresses σ_3, are counted off from γ and α. In this coordinate system, direction cosines (1.2) have the form

$$n_1 = \frac{\sqrt{2}}{2}, \quad n_2 = \pm\frac{\sqrt{2}}{2}, \quad n_3 = 0 \tag{2.1}$$

and the conditions of incompressibility and isotropy are

$$\varepsilon_\alpha + \varepsilon_\beta + \varepsilon_\gamma = 0, \tag{2.2}$$

$$\begin{aligned}&\varepsilon_\alpha + \varepsilon_{\alpha\beta}\frac{n_2}{n_1} + \varepsilon_{\alpha\gamma}\frac{n_3}{n_1}\\ &= \varepsilon_{\alpha\beta}\frac{n_1}{n_2} + \varepsilon_\beta + \varepsilon_{\beta\gamma}\frac{n_3}{n_2} = \varepsilon_{\alpha\gamma}\frac{n_1}{n_3} + \varepsilon_{\beta\gamma}\frac{n_2}{n_3} + \varepsilon_\gamma.\end{aligned} \tag{2.3}$$

Here, $\boldsymbol{\varepsilon}$ is the strain-rate tensor. Both the left-hand relation of isotropy (2.3) and formulas (2.1) yield the equality $\varepsilon_\alpha = \varepsilon_\beta$, while the incompressibility condition (2.2) leads to the following two relations:

$$\varepsilon_\alpha = -\frac{1}{2}\varepsilon_\gamma, \tag{2.4}$$

$$\varepsilon_\beta = -\frac{1}{2}\varepsilon_\gamma. \tag{2.5}$$

The right-hand relation of isotropy (2.3) shows that the directions of the principal strain rate ε_γ and of the principal stress σ_2 coincide with each other. This condition yields two following equalities:

$$\varepsilon_{\alpha\gamma} = \varepsilon_{\beta\gamma} = 0. \tag{2.6}$$

Let the velocity components along α, β, and γ be denoted as V_α, V_β, and V_γ. Equalities (2.6) can be satisfied, provided that

$$\begin{aligned}V_\alpha &= V_\alpha(\alpha, \beta),\\ V_\beta &= V_\beta(\alpha, \beta), \quad V_\gamma = V_\gamma(\gamma).\end{aligned} \tag{2.7}$$

The third equality in (2.7) shows that the velocity V_γ is constant on the surfaces $\gamma = \text{const}$. When, from the kinematic boundary conditions imposed onto the spatial plastic flow, it follows that $V_\gamma = 0$, the field of displacement velocities is determined by the components V_α and V_β, which lie on the surfaces $\gamma = \text{const}$. Then the displacement-velocity components u, v, and w are found by projecting V_α and V_β onto the x-, y-, and z-axes of the Cartesian coordinate system.

In the case of $V_\gamma = 0$, the strain rates along α, β, and γ are determined by the expressions

$$\varepsilon_\alpha = \frac{\partial V_\alpha}{\partial S_\alpha} + V_\beta\frac{\partial \ln R_\alpha}{\partial S_\beta}, \tag{2.8}$$

$$\varepsilon_\beta = \frac{\partial V_\beta}{\partial S_\beta} + V_\alpha\frac{\partial \ln R_\beta}{\partial S_\alpha}, \tag{2.9}$$

$$\varepsilon_\gamma = V_\alpha\frac{\partial \ln R_\gamma}{\partial S_\alpha} + V_\beta\frac{\partial \ln R_\gamma}{\partial S_\beta}. \tag{2.10}$$

In these expressions, we replace differentials for the radii of curvature by relations (1.13)–(1.15) and make use of the equalities $\cos\varphi_\beta \approx -1$, $\sin\varphi_\gamma \approx -1$, and $d\alpha \approx d\beta \approx d\varphi_\alpha$ for smooth surfaces $\gamma = \text{const}$. Then, using the notation $\varphi_\alpha = \varphi$, we find from equations (2.4) and (2.5) the following differential relations for the velocities V_α and V_β along the directions α and β:

$$dV_\alpha - V_\beta d\varphi = -\frac{dS_\alpha}{2R_\gamma}(V_\alpha\cos\varphi - V_\beta\sin\varphi), \tag{2.11}$$

$$dV_\beta + V_\alpha d\varphi = -\frac{dS_\beta}{2R_\gamma}(V_\alpha\cos\varphi - V_\beta\sin\varphi). \tag{2.12}$$

These relations coincide with the known expressions for axisymmetric strain [5] and, as $R_\gamma \longrightarrow 0$, turn into the formulas

$$dV_\alpha - 2V_\beta d\varphi = 0, \tag{2.13}$$

$$dV_\beta + 2V_\alpha d\varphi = 0. \tag{2.14}$$

For the plane strain $\left(\frac{1}{R_\gamma} = 0\right)$, relations (2.11) and (2.12) turn into Geiringer's equations.

In the case of plastic flow, combined fields of stresses and displacement velocities must satisfy the condition of nonnegativity of the dissipative function. In the space of principal stresses and strain rates, this condition has the form

$$D = \sigma_1\varepsilon_1 + \sigma_2\varepsilon_2 + \sigma_3\varepsilon_3 \geq 0$$

and, under the condition of full plasticity (1) and with allowance for incompressibility of the material, leads to the inequality

$$\pm\varepsilon_3 \geq 0, \tag{2.15}$$

where the signs $\pm$ correspond to condition (1.1).

3. We now consider problems of pressure being exerted by flat dies with smooth bases of different shapes onto the perfectly plastic half-space.

Figure 2 shows a die with the base in the form of an equilateral triangle. The length and midpoint of its A_3–A_1 side are taken as a characteristic size and the origin of the coordinates $\{x, y, z\}$, respectively. The plane $z = 0$ represents the boundary of the half-space $z \le 0$. The problem has three symmetry planes parallel to the z-axis and passing through both vertices of the triangle and its center C. Therefore, it is sufficient to consider the die element situated in the region OA_1C.

The die is indented into the half-space along the negative direction of the z-axis with the velocity $w_0 = -1$. The material is assumed to be slipping along the surface of its contact with the die. Along the normal to the boundary OA_1, at $z = 0$ and $x \ge 0$, the half-space boundary is compressed to the plastic state and is free from external normal and tangential stresses. The condition of full plasticity (1.1) yields

$$\sigma_x = \sigma_3 = -1, \quad \sigma_z = \sigma_1 = \sigma_y = \sigma_2 = 0, \qquad \sigma = -\frac{1}{3}, \quad z = 0, \quad x \ge 0. \tag{3.1}$$

Since the boundary OA_1 is rectilinear and coincides with the direction of σ_2, $\frac{1}{R_\gamma} = 0$ for the planes $y = \gamma =$ const, which are normal to this boundary. In these planes, within the distance d between the boundary OA_1 and the symmetry plane CA_1, the flow is planar and plastic. It also satisfies relations (1.20) and (1.21) for stresses and (2.11) and (2.12) for velocities, as well as the boundary conditions of the problem. When the angles that specify the direction of σ_3 vary from $\theta = \frac{\pi}{2}$, $\psi = 0$ at the half-space free boundary to $\theta = \pi$, $\psi = 0$ at the die boundary, the angle φ varies from $+\frac{\pi}{4}$ to $-\frac{\pi}{4}$. Since, in the case of the plane strain with rectilinear boundaries, the slip lines α are straight, the normal pressure on the die is constant. It is determined from boundary condition (3.1) for σ, relation (1.20), and the third equation of (1.3) and can be represented in the form

$$-\sigma_z = 1 + \frac{\pi}{2}. \tag{3.2}$$

The planes $\gamma =$ const are symmetric with respect to the symmetry lines OA_1, OA_2, and OA_3 of the die. Therefore, the velocity components normal to these lines are equal to zero and represent flow-boundary lines. Despite the change in the directions of the stresses σ_1 and σ_2 while passing through the flow-boundary lines, the contact stresses are continuous in these lines by virtue of the condition $\sigma_1 = \sigma_2$. The size

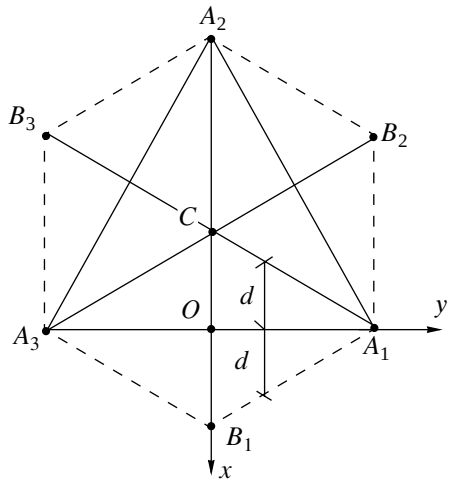

Fig. 2. Triangular die and boundaries of the plastic region (dashed line) in the half-space surface $z = 0$.

d of the plastic region arising ahead of the die boundary can be calculated as

$$d = \frac{1/2 - y}{\sqrt{3}}, \quad 0 \le y \le \frac{1}{2}. \tag{3.3}$$

The size d has a maximum value at the midpoints of the triangle sides and decreases to zero at the angles, as is shown in Fig. 2 by dashed lines. If a zone formed under the die is rigid, then, similar to the Prandtl solution when the strain is planar, the pressure (3.2) does not vary but the size d increases twice.

When the vertical projection of the die being indented represents a rectangle, boundary conditions (3.1) hold ahead of its edges at the half-space boundary free from external stresses. Depending on kinematic boundary conditions specified at the surface of die contact with the half-space, a planar plastic flow having the field of slip lines and arising in the plane sections $y =$ const and $x =$ const, which are normal to the die edges, is characterized by either the Prandtl or Hill velocity field. The pressure exerted on the die is constant and is determined by formula (3.2). Both the symmetry line $x = 0$ and bisectors of the right angles between the orthogonal die edges represent flow-boundary lines characterized by continuous variation of stresses and velocities. If the plastic material slips along the surface of the smooth die, the boundary of the plastic region on the surface of the half-space ahead of the die edges is determined by the expressions

$$d = 1 \text{ at } 0 \le y \le L - 1, \qquad d = L - y \text{ at } L - 1 \le y \le L, \tag{3.4}$$

$$d = y - L \text{ at } L \le y \le L + 1. \tag{3.5}$$

Here, expressions (3.4) correspond to the long die edge with the half-length $L \ge 1$, while (3.5) conforms to the short edge orthogonal to the long one and having the

length considered as a characteristic size of the die. While impressing a smooth flat die having an elliptic contour, we take as a characteristic dimension the length of its minor semiaxis directed along the *x*-axis. The length of the major semiaxis *b* directed along the *y*-axis represents the problem parameter. The essential distinction of an elliptic die from those considered before is the continuous variation of the curvature of its boundary. The parametric equation of the elliptic boundary in the first quadrant of the plane $\{x, y\}$ has the form

$$x_0 = \cos\xi, \quad y_0 = b\sin\xi, \quad 0 \le \xi \le \frac{\pi}{2}. \tag{3.6}$$

The inclination angle ψ of the normal with respect to the *x*-axis and the radius of curvature *R* at the point x_0, y_0 are determined by the expressions

$$\tan\psi = \frac{\tan\xi}{b}, \quad R = \frac{1}{b}(\sin^2\xi + b^2\cos^2\xi)^{3/2}. \tag{3.7}$$

At the free boundary of the half-space, i.e., ahead of the die boundary along the direction of the outward normal, the boundary conditions (3.1) are valid in the planes $\psi = \text{const}$, where the directions of the principal stresses σ_3, σ_1, and σ_2 are given by the angles $\theta = \frac{\pi}{2}, \psi$; $\theta = 0, \psi$; and $\theta = \frac{\pi}{2}, \psi - \frac{\pi}{2}$, respectively. The condition $V_\gamma = 0$, which corresponds to kinematic conditions in the symmetry planes $\psi = 0$ and $\psi = \frac{\pi}{2}$, is assumed to be valid in the planes $\psi = \text{const}$ passing through the points x_0, y_0 parallel to the *z*-axis. Therefore, differential relations (1.20), (1.21) for stresses and (2.11), (2.12) for velocities hold in these planes. In these relations,

$$\varphi = \frac{3}{4}\pi - \theta, \quad R_\gamma = x_1 + R, \tag{3.8}$$

and x_1 represents the coordinate counted off from the point x_0, y_0 along the direction of the outward normal to the die boundary.

Since the problem is statically determinate, we initially calculate the field of slip lines, which forms in the plane $\psi = \text{const}$, by numerically integrating [3, 4] equations (1.20) and (1.21) under the conditions $\varphi = \frac{\pi}{4}$ and $\sigma = -\frac{1}{3}$ (at the free half-space boundary) and $\varphi = -\frac{\pi}{4}$ (at the die boundary). This field contains the degenerate slip line α at the point $x_1 = 0$ of the die edge. The integration is performed until the symmetry axis $x = 0$ situated at the distance *d* from the point x_0, y_0 is reached, where

$$d = \frac{1}{b}\sqrt{\sin^2\xi + b^2\cos^2\xi}. \tag{3.9}$$

We consider the distance *h* between the boundary of the plastic region and the point x_0, y_0 of the half-space surface as an unknown problem parameter that must satisfy the equation

$$x_1(h) + d = 0 \text{ at the point } O_1. \tag{3.10}$$

An algorithm for numerically constructing the field of the slip lines determines the left-hand side of equation (3.10) as a continuous function of *h*. The solution to this equation with the relative accuracy of 10^{-4} is reached after two or three iterations performed by Newton's method. Figure 3a shows an example of the slip-line field calculated at $b = 2$ in the section $\psi = 0.423$ and the distribution of the normal pressure $-\sigma_z$. The pressure increases from its minimum value $1 + \frac{\pi}{2}$ occurring at the point x_0, y_0 to its maximum value being reached in the symmetry line $x_1 = -d$. When the parameter ψ varies from zero to $\frac{\pi}{2}$, the pressures exerted to the die increase to their maxima reached at $\psi = \frac{\pi}{2}$, where the strain is axisymmetric with the center of curvature situated at the ellipse focus at $d = R = \frac{1}{b}$. The average pressure *q* exerted to the die is calculated by integrating the pressure distributions over the sections $\psi = \text{const}$ so that

$$q = \frac{4}{\pi b}\int_0^{\pi/2}\int_{-d}^{0}(-\sigma_z)(R + x_1)dx_1 d\psi. \tag{3.11}$$

Being equal to $q = 2.717$ at $b = 2$, the average pressure *q* decreases with increasing *b* and approaches $1 + \frac{\pi}{2}$. For a circular die ($b = 1$), the maximum value is $q = 2.846$ [3].

In the cross sections $\psi = \text{const}$, the field of the displacement velocities V_α, V_β is calculated by using the condition of the continuity of the velocities $w_0 = -1$ and V_β, which are normal to the die and to the O_1DCB rigid-plastic boundary (Fig. 3a), respectively. If $d < R$, the velocity discontinuity $[V_\alpha]$ varying in its magnitude arises along the O_1DCB boundary. It is calculated by integrating equation (2.11) with the initial condition

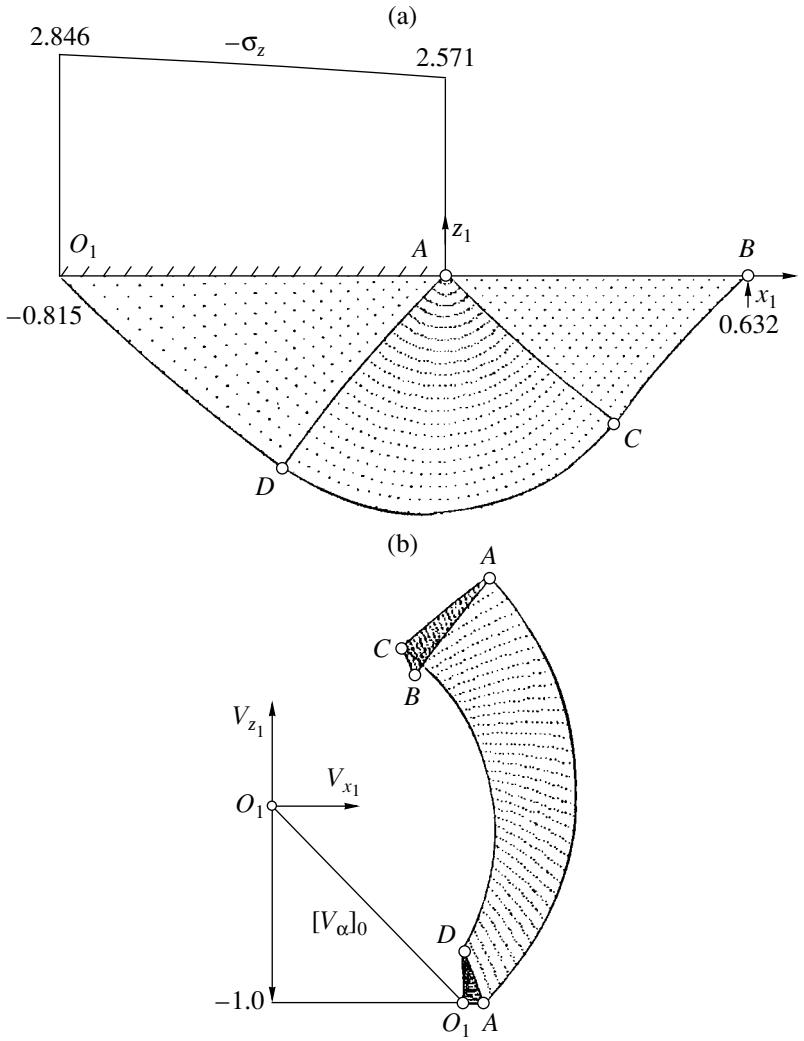

Fig. 3. (a) Slip-line field and (b) velocity hodograph in the cross section $\psi = 0.423$ along the normal to the ellipse edge for $b = 2$.

$[V_\alpha] = \sqrt{2}$, which is specified at the point O_1 and is determined by the formulas

$$[V_\alpha] = \sqrt{\frac{2(R-d)}{R+x_1}}, \quad V_\beta = 0 \text{ at } O_1DCB; \quad (3.12)$$

$$V_\alpha - V_\beta = \sqrt{2} \text{ at } O_1A. \quad (3.13)$$

At $\psi = \frac{\pi}{2}$ and $R = d$ at the ellipse focus, we have an axisymmetric flow with the velocities continuous along O_1DCB. Then $V_\alpha = V_\beta = 0$, and the velocity field has a pole-type singularity in a small vicinity of the point O_1 [5].

The velocity field is calculated by numerically integrating equations (2.11) and (2.12) while solving the mixed boundary value problem with either the boundary conditions (3.12), (3.13) or the condition of a continuous velocity along O_1DCB at $\psi = \frac{\pi}{2}$. The velocity field shown in Fig. 3b as a hodograph in the plane $\{V_{x_1}, V_{z_1}\}$ corresponds to the field of slip lines presented in Fig. 3a. In contrast to the hodograph corresponding to the plane strain in the triangular Cauchy regions, the velocity fields occurring both under the elliptic die and near the free half-space boundary are nonuniform. In the region of the centered fan of slip lines, the velocities depend on both polar variables having the center at the die edge. As a result of comparison of the corresponding regions formed by nodal points in the field of the slip lines and in the velocity hodograph, we can see that the strain rate ε_3 is negative along the direction of the stress σ_3 and inequality (2.15) controlling the nonnegativity of the dissipation D holds.

Upon calculating the fields of both stresses and displacement velocities in the plane $\psi = \text{const}$, we can find the stress tensor as a function of the coordinates $\{x, y, z\}$.

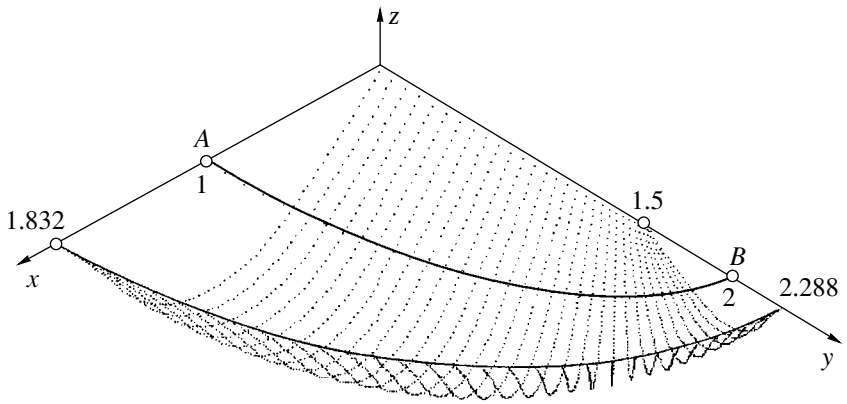

Fig. 4. Isometric projection of the rigid-plastic boundary for the smooth elliptic die with $b = 2$.

This calculation is performed by formulas (1.2)–(1.4) with the use of the expression $\theta = \frac{3}{4}\pi - \varphi$ and the equations

$$x = x_0 + x_1\cos\psi, \quad y = y_0 + x_1\sin\psi, \quad z = z_1, \tag{3.14}$$

which relate the coordinates x, y, z to the coordinates x_1, z_1 in the plane $\psi = \text{const}$, where x_0, y_0 are the coordinates of the die boundary [see (3.6)]. The displacement velocities u, v, w in the coordinates $\{x, y, z\}$ are determined by the formulas

$$\begin{aligned} u &= (V_\alpha\cos\varphi - V_\beta\sin\varphi)\cos\psi, \\ v &= (V_\alpha\cos\varphi - V_\beta\sin\varphi)\sin\psi, \\ w &= V_\alpha\sin\varphi + V_\beta\cos\varphi. \end{aligned} \tag{3.15}$$

Figure 4 shows the isometric projection of the spatial slip surface (i.e., the rigid-plastic boundary) and the die boundary AB for $b = 2$. With increasing the parameter b, the plastic region decreases while approaching the symmetry plane $\psi = \frac{\pi}{2}$. At the same time, in the section with the smallest curvature $\psi = 0$, the plastic region increases (so that the value of the parameter h approaches 1). This corresponds to the plane strain and is accompanied by the appropriate variation in the stress and velocity fields.

REFERENCES

1. D. D. Ivlev, *Theory of Ideal Plasticity* (Nauka, Moscow, 1966).
2. D. D. Ivlev and A. Yu. Ishlinskiĭ, Dokl. Akad. Nauk **368**, 333 (1999) [Dokl. Phys. **44**, 642 (1999)].
3. A. Yu. Ishlinskiĭ, Prikl. Mat. Mekh. **8**, 314 (1944).
4. B. A. Druyanov and R. I. Nepershin, *Theory of Technological Plasticity* (Mashinostroenie, Moscow, 1990).
5. R. T. Shield, Proc. R. Soc. London, Ser. A **233** (1193), 267 (1955).

Translated by Yu. Verevochkin

Doklady Physics, Vol. 46, No. 12, 2001, pp. 897–899. Translated from Doklady Akademii Nauk, Vol. 381, No. 5, 2001, pp. 623–625.

MECHANICS

Kinetic Description of Nanoparticle Diffusion in Rarefied Gas

V. Ya. Rudyak and S. L. Krasnolutski

Presented by Academician A.K. Rebrov July 23, 2001

Received August 7, 2001

Usually the Einstein–Langevin theory is used to describe the diffusion of disperse particles in liquids and dense gases. This theory suggests the following expression for the diffusivity:

$$D_E = \frac{kT}{\gamma_s}, \quad \gamma_s = 6\pi\eta R, \tag{1}$$

where η and T are the viscosity of the carrier medium and its temperature, and R is the characteristic radius of a Brownian particle.

In order to extend the application region of formula (1) and adapt it for describing the diffusion of disperse particles in a rarefied gas, the Cunningham–Millikan experimental correlation is usually used:

$$D = \frac{kT}{\gamma_k}, \quad \gamma_k = 6\pi\eta R\left(1 + A\frac{l}{R} + Q\frac{l}{R}e^{-bR/l}\right)^{-1}. \tag{2}$$

The constants entering into expression (2) are found in the Millikan experiments [1] and are $A = 0.864$, $Q = 0.29$, and $b = 1.25$. Here, l is the mean free path for molecules of the carrier gas.

Correlation (2) is widely used in various applications. For example, it is employed in studies of the diffusion of aerosol particles and determination of their size distribution (see, e.g., [2]). At the same time, in the Millikan experiments the constants entering into formula (2) were found in a very narrow temperature range (from 19 to 24°C). Since the diffusion noticeably depends on carrier-gas temperature, the application of the above constants outside the indicated temperature range can lead to quantitatively and qualitatively wrong results.

In this paper, for studying the nanoparticle diffusion (sizes of these particles usually attain from tens to hundreds of angstroms), we use the kinetic theory of gases. The comparison of diffusion coefficients calculated by this method and experimental data has shown that correlation (2) is indeed applicable in a very narrow temperature range. Outside of this range, the calculation predicts an incorrect dependence for the diffusion coefficient as a function of the disperse-particle radius, as well as of temperature.

In [3–5], it was shown that, in the general case, the dynamics of even a rarefied gas suspension is described by a system of kinetic equations that contain many-particle collision integrals. However, for describing rarefied ultradisperse (and, in certain cases, also finely dispersed) gas suspensions, we are able to use the system of Boltzmann kinetic equations. This is the class that covers gas suspensions and aerosols whose disperse components are nanoparticles. In a one-fluid approximation, the state of gas suspensions is described by unified mean-mass macroscopic variables. As a result of solving the Boltzmann equation, we arrive at the Navier–Stokes equations, the transport coefficients in them being determined by well-known formulas. In particular, we have for the diffusivity [6]

$$D = \frac{3}{16}\frac{\sqrt{2\pi\mu kT}}{n\mu\pi R^2\Omega_{ij}^{(1,1)*}(T^*, \sigma_{ij}/R)}. \tag{3}$$

Here, $\mu = \dfrac{mM}{m+M}$; m and M are, respectively, the molecular mass of the carrier gas and the disperse-particle mass; $T^* = \dfrac{T}{\varepsilon_{ij}}$; $\Omega_{ij}^{(l,m)*}$ are the so-called Ω integrals [6]; and ε_{ij} and σ_{ij} are the parameters of a potential describing the interaction of carrier-gas molecules with atoms (molecules) of a disperse particle.

The key matter in the application of formula (3) for the description of the nanoparticle diffusion is the need to know their potential for interaction with molecules of the carrier gas. This potential was constructed in our studies [7, 8]. In the course of the construction, a disperse particle was considered as a set of atoms (molecules), and the interaction potential for a carrier-gas molecule with a particle was determined as a sum of potentials of the given molecule for interactions with all atoms of the particle. Such models turned out to be adequate in various aerospace applications in certain tech-

Novosibirsk State University of Architecture and Civil Engineering, PO Box 258, Novosibirsk, 630008 Russia

1028-3358/01/4612-0897$21.00

nological fields, e.g., microelectronics and nuclear-reactor and thermonuclear-fusion materials science. If a solid particle has the radius R, and the potential for interaction of its atoms (molecules) with a carrier-gas molecule is described by the Lennard-Jones potential

$$\Phi_{ij} = 4\varepsilon_{ij}\left[\left(\frac{\sigma_{ij}}{r}\right)^{12} - \left(\frac{\sigma_{ij}}{r}\right)^{6}\right], \quad (4)$$

then the potential for interaction of a carrier-gas molecule with a disperse particle has the form [7, 8]

$$\Phi(r) = \Phi_9(r) - \Phi_3(r), \quad (5)$$

$$\Phi_9(r) = C_9\left\{\left[\frac{1}{(r-R)^9} - \frac{1}{(r+R)^9}\right] - \frac{9}{8r}\left[\frac{1}{(r-R)^8} - \frac{1}{(r+R)^8}\right]\right\},$$

$$\Phi_3(r) = C_3\left\{\left[\frac{1}{(r-R)^3} - \frac{1}{(r+R)^3}\right] - \frac{3}{2r}\left[\frac{1}{(r-R)^2} - \frac{1}{(r+R)^2}\right]\right\}.$$

Here, $C_9 = \dfrac{4\pi\varepsilon_{ij}\sigma_{ij}^{12}}{45V}$, $C_3 = \dfrac{2\pi\varepsilon_{ij}\sigma_{ij}^{6}}{3V}$, and V is the effective volume per one molecule of the disperse particle. Thus, potential (5) depends on the parameters ε_{ij} and σ_{ij} of the pair potential for the interaction of carrier-gas molecules with a disperse particle and on the particle size. In the case of sufficiently large particles with a typical size exceeding 10^{-5} cm, it is possible instead of formula (5) to use the much simpler potential for interaction of molecules with a rigid surface [9], namely,

$$\Phi(r) = \frac{C_9}{r^9} - \frac{C_3}{r^3}.$$

Thus, for determining the diffusivity of nanoparticles (3), it is necessary to calculate Ω integrals for potential (5). This requires, in turn, knowing the constants of the pair potential (4) for interaction of a carrier-gas molecule with a nanoparticle atom (molecule). To do this, we employed the simplest combination relations

$$\sigma_{ij} = \sqrt{\sigma_{ii}\sigma_{jj}}, \quad \varepsilon_{ij} = \sqrt{\varepsilon_{ii}\varepsilon_{jj}},$$

$$\sigma_{ij} = \frac{\sigma_{ii} + \sigma_{jj}}{2}, \quad \varepsilon_{ij}\sigma_{ij}^6 = \sqrt{\varepsilon_{ii}\varepsilon_{jj}}\sigma_{ii}^3\sigma_{jj}^3.$$

We have developed a specific code for calculating Ω integrals with potential (5) and have tested it using data for mixtures of rarefied gases, which were borrowed from available publications. The calculation accuracy was proven to be sufficiently high.

The dependence of values of Ω integrals (and, as a consequence, transport coefficients) on parameters of the intermolecular interaction potential in a rarefied gas is extremely strong. Therefore, it is first of all necessary to estimate the effect of employing certain combination relations in calculating Ω integrals. However, numerous calculations performed have shown that, in contrast to a rarefied gas, the Ω integrals for potential (5) weakly depend on both different combination relations and rather contradictory data concerning parameters of intermolecular potentials. The spread of values for Ω integrals in any case was no higher than 0.5%. The weak dependence of Ω integrals on parameters of intermolecular potentials for molecules of the carrier gas and of a disperse particle is explained by the fact that potential (5) was obtained by averaging over the large number of atoms in a dispersed particle. This weak sensitivity of the nanoparticle transport coefficients with respect to parameters of the intermolecular potential for system molecules is extremely important, since experimental data for these parameters often turn out to be unreliable.

The most important feature of the dispersed-particle diffusivity is its dependence on the particle radius. In the case of sufficiently large particles, when $R \gg l$, this dependence is described by formula (1). The diffusivity of a particle is inversely proportional to its radius. In our formulas (3), (5), this dependence turns out to be much more complicated, because the value of the Ω integral is also a function of the dispersed-particle radius. For a certain fixed temperature, this dependence is well approximated by the relation

$$\Omega_{ij}^{(1,1)*} \sim 1 + \frac{a_1}{\sqrt{R}} + \frac{a_2}{R}.$$

Here, a_i are certain constants depending on temperature. For radii of disperse particles $R > 5 \times 10^{-6}$ cm, Ω integrals virtually cease to vary with the particle radius, and their values tend to unity. Figure 1 illustrates the diffusivity of nanoparticles as a function of the particle radius at a fixed temperature (T = 288 K). Here, as an example, we considered the diffusion of condensation nuclei in air at atmospheric pressure. The continuous curve corresponds to the dependence calculated according to formulas (3), (5). The dashed curve demonstrates the dependence described by Einstein formula (1). Experimental data of [10] are represented by triangles.

The dotted curve in Fig. 1 corresponds to the experimental correlation (2). It is well consistent with our data in nearly the entire region under study. The divergence on the order of 5–10% appears only in the regions of large and very small radii.

Finally, we should note that the diffusivity of nanoparticles, as in the case of the diffusion of molecules and Brownian particles, essentially depends on the temperature of the medium. The shape of the diffusivity curve as a function of temperature at atmospheric pres-

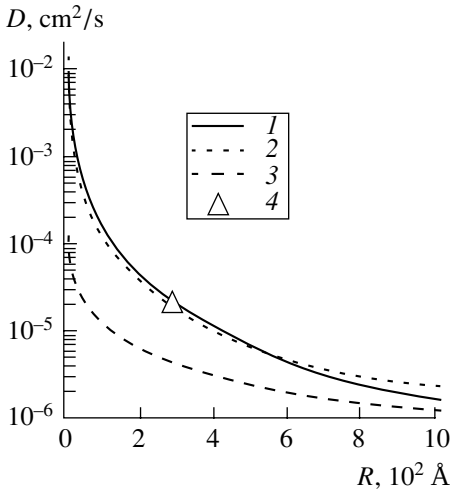

Fig. 1. Diffusivity D as a function of particle radius R: (*1*) calculations with potential (5); (*2*) calculations by the Cunningham–Millikan formula; (*3*) calculations by the Einstein formula; (*4*) experimental data of [10].

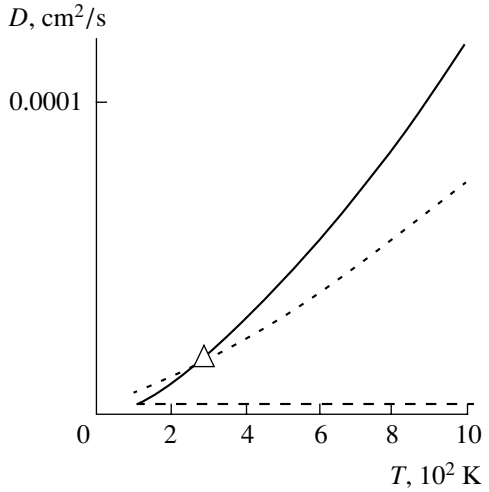

Fig. 2. Diffusivity D as a function of temperature T.

sure for a fixed value of R (R = 300 Å) is presented in Fig. 2. Again, diffusion of condensation nuclei in air at atmospheric pressure is considered as an example. The solid line in Fig. 2 corresponds to the dependence calculated by formulas (3), (5). The dependence shown by the dashed curve represents the calculation by Einstein formula (1). In the latter case, tabular data were used to determine the air viscosity as a function of temperature. The experimental data of [10] (triangles) and the data calculated according to correlation dependence (2) are plotted alongside. As is seen from Fig. 2, the diffusivity of an aerosol particle changes by tens times with temperature variation within the range 100–1000 K. On the other hand, the Einstein formula predicts a diffusivity that very weakly varies with temperature. Formula (2) has a sufficiently narrow temperature-application region. It is consistent with our data within an accuracy of 15% only in the temperature range from 100 to 300 K. At higher temperatures, the Cunningham–Millikan formula leads to strongly underestimated diffusivity and, thus, cannot be applied.

ACKNOWLEDGMENTS

This work was supported in part by the Russian Foundation for Basic Research, project nos. 00-15-96164 and 01-01-0045.

The authors are grateful to A.K. Rebrov for his interest in this work and for discussions.

REFERENCES

1. R. A. Millikan, Phys. Rev. **22** (1), 1 (1923).
2. S. K. Friedlander, *Smoke, Dust, and Haze. Fundamentals of Aerosol Dynamics* (Oxford Univ. Press, Oxford, 2000).
3. V. Ya. Rudyak, Pis'ma Zh. Tekh. Fiz. **18** (20), 77 (1992) [Sov. Tech. Phys. Lett. **18**, 681 (1992)].
4. M. Yu. Gladkov and V. Ya. Rudyak, Zh. Tekh. Fiz. **64** (4), 170 (1994) [Tech. Phys. **39**, 441 (1994)].
5. M. Yu. Gladkov and V. Ya. Rudyak, Izv. Akad. Nauk, Mekh. Zhidk. Gaza, No. 2, 165 (1994).
6. J. H. Ferziger and H. G. Kaper, *Mathematical Theory of Transport in Gases* (North-Holland, Amsterdam, 1972; Mir, Moscow, 1976).
7. V. Ya. Rudyak and S. L. Krasnolutski, Preprint No. 3(13)-98, NGASU (Novosibirsk, 1998).
8. V. Y. Rudyak and S. L. Krasnolutski, in *Proceedings of the XXI International Symposium on Rarefied Gas Dynamics, Marseille, 1998*, Vol. 1, p. 263.
9. F. O. Goodman and H. Y. Wachman, *Dynamics of Gas-Surface Scattering* (Academic, New York, 1976; Mir, Moscow, 1980).
10. J. J. Nolan and V. H. Guerrini, Trans. Faraday Soc. **32**, 1175 (1936).

Translated by G. Merzon

Doklady Physics, Vol. 46, No. 12, 2001, pp. 900–903. Translated from Doklady Akademii Nauk, Vol. 381, No. 5, 2001, pp. 626–629.

MECHANICS

Dynamics of Disperse Systems Containing a Gas Mixture and Hollow Selectively Permeable Microspheres

Corresponding Member of the RAS V. M. Fomin and S. V. Dolgushev

Received July 20, 2001

Flows of two-phase mixtures consisting of a gas and solid particles are quite common in both nature and technology. They are widely covered in the literature [1]. Systems of this class that remain improperly studied up to now are moving gas mixtures that contain hollow selectively permeable microspheres (with membrane-type shells [2, 3]) dispersed within them [4, 5]. Such particles are hollow spheres 10 to 1000 μm in diameter with shells 0.5–10 μm thick, which are usually made of different kinds of glass, corundum, plastic, or other materials [4, 5] and can also arise as a result of combusting certain kinds of coal [6]. These particles were even used in various applications, e.g., as targets for laser-induced nuclear fusion [7], fillers in the production of light high-strength composites [4], microballoons for storing hydrogen and helium isotopes [7], in pharmaceutics and medicine for the efficient transport of drugs to certain kinds of tissues [5], for considerable reduction in the noise level by microspheres with perforated shells [8], etc.

The authors of this paper have proposed a technique for the separation of gas mixtures using selectively permeable (membrane) shells transported through pipelines with the mixture being separated [9]. The goal of the present paper is to derive equations describing the dynamics of mixtures based on the model of interpenetrating continua first put forward by Pakhmatulin and Nigmatulin [1].

Furthermore, we use relationships for the balance of the mass, momentum, and energy [1, 10], which are related to a certain specified portion of individual components. We also employ the quasi-steady solution to the problem of filling microsphere hollows by gases penetrating through the membrane-type shell [2, 3]. Thus, we can write out the following partial differential equations for gas mixtures containing hollow selectively permeable solid microspheres

$$\frac{\partial m}{\partial t} + \nabla(m\mathbf{U}_\mathrm{s}) = 0;$$

$$\frac{\partial \rho_i^{(\mathrm{in})}}{\partial t} + \nabla(\rho_i^{(\mathrm{in})}\mathbf{U}_\mathrm{s}) = K_i;$$

$$\frac{\partial \rho_i^{(\mathrm{ex})}}{\partial t} + \nabla(\rho_i^{(\mathrm{ex})}\mathbf{U}^{(\mathrm{ex})}) = -K_i;$$

$$\frac{\partial \rho_\mathrm{s}^+\mathbf{U}_\mathrm{s}}{\partial t} + \nabla(\rho_\mathrm{s}^+\mathbf{U}_\mathrm{s}\cdot\mathbf{U}_\mathrm{s}) = n_\mathrm{s}\mathbf{f} - m\nabla p_0^{(\mathrm{ex})} + \sum_{i=1}^{N} K_i\mathbf{U}_\mathrm{s};$$

$$\frac{\partial \rho^{(\mathrm{ex})}\mathbf{U}^{(\mathrm{ex})}}{\partial t} + \nabla(\rho^{(\mathrm{ex})}\mathbf{U}^{(\mathrm{ex})}\cdot\mathbf{U}^{(\mathrm{ex})})$$

$$= -n_\mathrm{s}\mathbf{f} - (1-m)\nabla p_0^{(\mathrm{ex})} - \sum_{i=1}^{N} K_i\mathbf{U}_\mathrm{s};$$

$$\frac{\partial}{\partial t}\left[\rho_\mathrm{s}^+\left(e_\mathrm{s}^+ + \frac{\mathbf{U}_\mathrm{s}^2}{2}\right)\right] + \nabla\left[\rho_\mathrm{s}^+\mathbf{U}_\mathrm{s}\left(e_\mathrm{s}^+ + \frac{\mathbf{U}_\mathrm{s}^2}{2}\right)\right]$$

$$= -m\mathbf{U}_\mathrm{s}\nabla p_0^{(\mathrm{ex})} + n_\mathrm{s}q + n_\mathrm{s}\mathbf{f}\mathbf{U}_\mathrm{s} + \sum_{i=1}^{N} K_i\left[e_i(T_\mathrm{s}) + \frac{\mathbf{U}_\mathrm{s}^2}{2}\right];$$

$$\frac{\partial}{\partial t}\left[\rho^{(\mathrm{ex})}\left(e^{(\mathrm{ex})} + \frac{\mathbf{U}^{(\mathrm{ex})^2}}{2}\right)\right] + \nabla\left[\rho^{(\mathrm{ex})}\mathbf{U}^{(\mathrm{ex})}\left(e^{(\mathrm{ex})} + \frac{\mathbf{U}^{(\mathrm{ex})^2}}{2}\right)\right]$$

$$= -\nabla(p_0^{(\mathrm{ex})}\mathbf{U}^{(\mathrm{ex})})$$

$$+ m\mathbf{U}_\mathrm{s}\nabla p_0^{(\mathrm{ex})} - n_\mathrm{s}q - n_\mathrm{s}\mathbf{f}\mathbf{U}_\mathrm{s} - \sum_{i=1}^{N} K_i\left[e_i(T_\mathrm{s}) + \frac{\mathbf{U}_\mathrm{s}^2}{2}\right];$$

$$p_0^{(\mathrm{ex})} = \sum_{i=1}^{N} p_i^{(\mathrm{ex})},$$

$$p_i^{(\mathrm{ex})} = \rho_{0i}^{(\mathrm{ex})}R_iT^{(\mathrm{ex})} = \frac{\rho_i^{(\mathrm{ex})}R_iT^{(\mathrm{ex})}}{1-m};$$

$$e^{(\mathrm{ex})} = \sum_{i=1}^{N} e_i^{(\mathrm{ex})}, \quad e_\mathrm{s}^+ = e_\mathrm{s} + \sum_{i=1}^{N} e_i^{(\mathrm{in})},$$

$$e_i^{(\mathrm{ex})} = C_{Vi}T^{(\mathrm{ex})}, \quad e_i^{(\mathrm{in})} = C_{Vi}T_\mathrm{s},$$

$$e_\mathrm{s} = C_VT_\mathrm{s}, \quad i = 1, 2, \ldots, N.$$

In these equations, all symbols denote (if there are no particular indications) the effective parameters (i.e.,

Institute of Theoretical and Applied Mechanics, Siberian Division, Russian Academy of Sciences, Institutskaya ul. 4/1, Novosibirsk, 630090 Russia

1028-3358/01/4612-0900$21.00

those averaged over a small macroscopic volume of the mixture as a whole). Here, n_s is the number of microspheres per unit volume of the mixture, $m = n_s V_s$ is the volume fraction of the microspheres in the mixture, V_s is the volume of a microsphere, ρ is the density, $\mathbf{U}$ is the velocity, p is pressure, T is temperature, q is the heat flux towards the outer surface of an individual microsphere, and $\mathbf{f}$ is the resistance force acting on a microsphere from the carrier gaseous media. Furthermore, e is the internal energy per unit mass of the material (gas or solid shells), C_V and C_s are the specific heat at a constant volume per unit mass of the gas and of solid microsphere shells, R_i is the gas constant for the ith gas, and N is the number of the components in the gas mixture. The superscripts (in) and (ex) denote the gas parameters in the interior and exterior of the microspheres, respectively. The subscript i corresponds to the ith gas component, subscript 0 indicates true values of the parameters (not averaged over the mixture volume), and subscript "s" denotes the parameters relevant to the microsphere solid shells. The superscript (+) denotes values corresponding to a composite particle, i.e., to a microsphere together with the gas contained in it. A mass K_i of the ith gas component absorbed in a unit volume of the mixture per unit time equals $n_s\kappa_i$, where

$$\kappa_i = \frac{Q_i^* S_{\text{eff}} \mu_i}{\delta}(p_{0i}^{(\text{ex})} - p_{0i}^{(\text{in})})$$

is the mass of the ith gas component absorbed by one microsphere per unit time. This quantity is calculated on the basis of the steady-state approximation for the process of diffusion-induced penetration of molecules through a spherical membrane shell. In addition, $p_{0i}^{(\text{in})}$ is the pressure of the ith gas component inside the microsphere, μ is the mass of a gas molecule, S_{eff} is the effective surface area of the microsphere for the steady-state diffusion [4] ($S_{\text{eff}} = 4\pi R_+ R_-$, where R_+ and R_- are the radii of outer and inner surfaces of the microsphere shell), δ is the thickness of the microsphere shell, and Q_i^* is the permeability of the membrane material for the ith gas component (expressed in units of [molecule m/(m^2 s Pa)]). In the course of calculations, it is convenient to express values of K_i in terms of the effective gas density. Taking into account the equation of state for an ideal gas, we arrive at

$$K_i = \frac{n_s S_{\text{eff}} T_s Q_i R_u}{\delta}(\rho_{0i}^{(\text{ex})} - \rho_{0i}^{(\text{in})}),$$

where R_u is the universal gas constant, the values of permeability $Q_i = \dfrac{Q_i^*}{N_A}$ are expressed in units of kmol m/(m^2 s Pa), and N_A is the Avogadro's number.

The simplest case of motion in systems of the type under study is a steady-state (with respect to the temperature and velocity) flow of hollow permeable microspheres suspended in pure gas. As an example, we consider a problem concerning the dispersion and absorption coefficient for the acoustic perturbations propagating in a quiescent homogeneous mixture of hollow permeable microspheres in pure helium. To solve this problem, it is convenient to consider the system as a homogeneous mixture with a fixed mass percentage of the solid phase. In this case, besides the usual parameters (pressure, density, temperature, and velocity), there is an additional parameter, namely, the true gas density inside the microspheres. Simplifying the above equations (under the condition of equal velocities and temperatures of the mixture components), we find the gas-dynamics equations for a homogeneous two-phase mixture, which are closed by the equation of state in the form

$$p = \frac{\rho R T}{1 - \dfrac{\varphi_s \rho}{\bar{\rho}_s}}\left(1 - \frac{\varphi_s \beta^3}{1 - \varphi_s}\frac{\rho_0^{(\text{in})}}{\bar{\rho}_s}\right),$$

where p is the pressure in the mixture (outside the microspheres), ρ is the mixture density, $\bar{\rho}_s$ is the shell-material density averaged over the microsphere volume, φ_s is the mass concentration of the solid phase, $\beta = \dfrac{R_-}{R_+}$, $\rho_0^{(\text{in})}$ is the true gas density inside the microsphere, $R = (1 - \varphi_s)R_0$ is the effective gas constant for the mixture, and R_0 is the gas constant for the pure gas. In this case, the dynamics of the gas mass contained in microsphere hollows is described by the following relaxation equation:

$$\frac{\partial \rho_0^{(\text{in})}}{\partial t} + \mathbf{U}\nabla\rho_0^{(\text{in})} = -\frac{(1 - \varphi_s)\rho - \left[1 - \varphi_s(1 - \beta^3)\dfrac{\rho}{\bar{\rho}_s}\right]\rho_0^{(\text{in})}}{\tau},$$

where the effective relaxation time τ for the gas density inside the microspheres is determined by the relationship

$$\tau = \left(1 - \frac{\varphi_s \rho}{\bar{\rho}_s}\right)\tau_0 = (1 - m)\tau_0,$$

$$\tau_0(T) = \frac{(1 - \beta)\beta^2 R_+^2}{3 R_u Q T}.$$

We write out the dimensionless continuity equations for one-dimensional flows, namely, the conservation equations for the momentum, energy, and mass density of the gas inside the microspheres. Then we linearize these equations and consider infinitesimally weak sinu-

soidal perturbations of an arbitrary parameter y of the type

$$y = y_0\{1 + \delta y \exp[i(kx - \omega t)]\},$$

where ω is the dimensionless circular vibration frequency $\left(\omega = \frac{\Omega R_+}{c_0}\right.$, Ω is the dimensional circular frequency, c_0 is the sound velocity in the pure gas$\left.\right)$, k is the dimensionless wave number, and $i = \sqrt{-1}$. Thus, we find the dispersion relation for acoustic waves. Solving the equation obtained, we find the expression for the frequency dependence of the dimensionless sound velocity $\bar{c}$ and its attenuation coefficient γ at a distance equal to one wavelength

$$\bar{c} = \frac{a}{\sqrt{\kappa}\Phi\cos\alpha}, \quad \gamma = 2\pi\tan\alpha.$$

The sound velocity is normalized to its value in the pure gas; κ is the ratio for the specific heat of the pure gas at a constant pressure and volume. We also introduced the following notation:

$$\Phi = \frac{\left\{\left[\frac{(1-\varphi_s)A^2}{b^2}\left(1 + \frac{R}{C_V}\right) + \left(\frac{1}{b} + \frac{R_0}{C_V}\right)\omega^2\right]^2 + \left(\frac{\omega A\beta^3\varphi_s r}{ba^2}\right)^2\right\}^{\frac{1}{4}}}{\left[\left(\frac{A}{b}\right)^2\left(1 + \frac{R}{C_V}\right)^2 + \left(\frac{1}{b} + \frac{R_0}{C_V}\right)^2\omega^2\right]^{\frac{1}{2}}},$$

$$\alpha = 0.5\arctan\left[\frac{\omega A\beta^3\frac{\varphi_s r}{b^2}}{(1-\varphi_s)\left(\frac{A}{b}\right)^2\left(1 + \frac{R}{C_V}\right) + \left(\frac{1}{b} + \frac{R_0}{C_V}\right)\omega^2}\right],$$

$$a = 1 - \varphi_s[1 - (1-\beta^3)r], \quad b = 1 - \varphi_s(1 + \beta^3 r),$$

$r = \left(\frac{\rho_0^{(in)}}{\bar{\rho}_s}\right)_{eq}$ is the ratio of the gas densities inside (or outside) the microsphere to the density of the solid material averaged over the microsphere volume under equilibrium conditions for the nonperturbed medium,

$$A = \frac{3MQ\sqrt{R_0 T_0}}{(1-\beta)\beta^2 R_+}.$$

Here, M is the mass of 1 kmol of the gas, $C_V = (1 - \varphi_s)C_{V0} + \varphi_s C_s$, where C_V, C_{V0}, and C_s are specific heats at constant volume for the mixture, pure gas, and microsphere material, respectively.

The calculations were performed for hollow microspheres with porous glass shells characterized by the permeability coefficient $Q = 3.08 \times 10^{-16}$ kmol m/(m^2 s Pa). The unperturbed conditions correspond to $T_0 = 300$ K and $p_0 = 10^5$ Pa. We also took $C_s = 750$ J/(kg K) and $\rho_s = 2500$ kg/m^3.

In the figure, we present the frequency dependence for the attenuation coefficient at a distance equal to one wavelength and for the relative sound velocity at $\beta = 0.98$ and the volume fraction m of the solid phase in the mixture, which equals 0.1 (this corresponds to the mass fraction $\varphi_s = 0.989$). Characters *1*, *2*, and *3* denote curves corresponding to $R_+ = 2 \times 10^{-5}$ m, 3×10^{-5} m, and 4×10^{-5} m, respectively. The shape of these curves is typical of media with relaxation processes of different natures (vibrational and rotational relaxation [11], temperature and velocity relaxation of the particles suspended in the gas [12]). They exhibit a clearly pronounced peak of the attenuation coefficient γ at $\Omega_m = \frac{1}{\tau}$ and a gradual transition near this frequency from the equilibrium value of the sound velocity to its frozen value with the rise in frequency. The relaxation time for the internal pressure increases with the size of the microspheres, and the peak value of the attenuation coefficient is shifted to lower frequencies (thus the transition from the equilibrium sound velocity occurs at a lower frequency). The increase in the volume fraction of the microspheres is accompanied by a significant reduction in the sound velocity compared to its value in pure helium in both the equilibrium (low-frequency) and frozen (high-frequency) limits. Note that the peak values of the attenuation coefficient remain invariable: they only shift along the frequency axis with an increase in the microsphere radius.

The asymptotic values of the equilibrium ($\bar{c}_e$) and the frozen ($\bar{c}_f$) relative sound velocities are found as

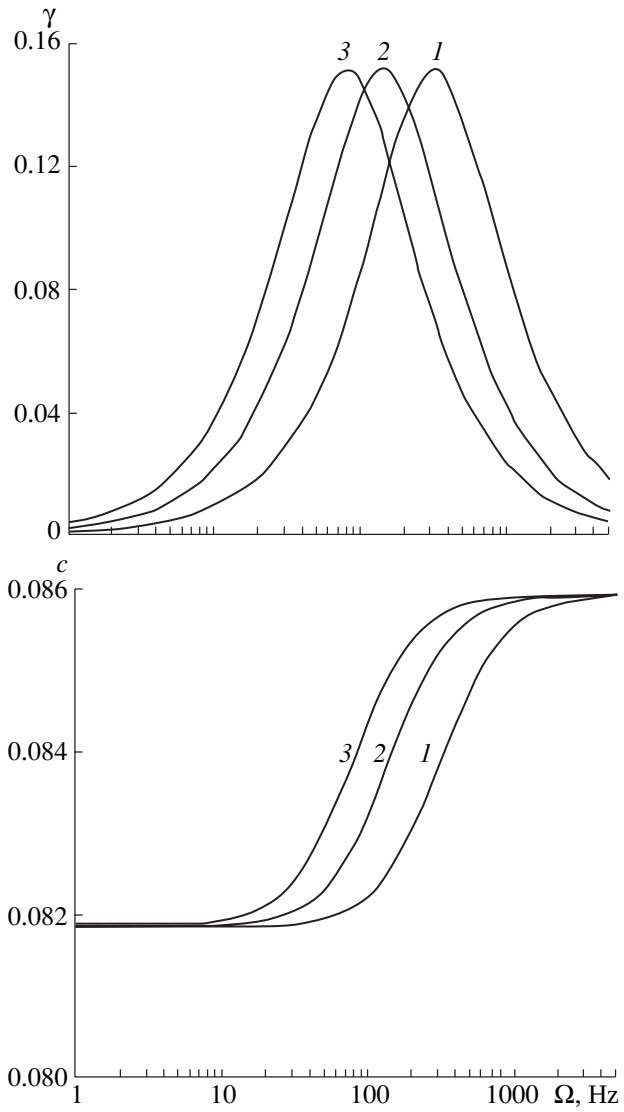

Acoustic attenuation coefficient γ at a distance equal to one wavelength and the sound velocity c as functions of the frequency in the mixture of helium with hollow permeable microspheres for the values of the parameters $\varphi_s = 0.989$, $\beta = 0.98$: (*1*) $R_+ = 2 \times 10^{-5}$ m; (*2*) $R_+ = 3 \times 10^{-5}$ m; and (*3*) $R_+ = 4 \times 10^{-5}$ m.

low- and high-frequency limits of the expression for $\bar{c}(\Omega)$. They are given by the following formulas:

$$\bar{c}_e = \sqrt{\frac{a^2}{(1-\varphi_s)\kappa}\left(1+\frac{R}{C_V}\right)}, \quad \bar{c}_f = \sqrt{\frac{a^2}{\kappa}\left(\frac{1}{b}+\frac{R_0}{C_V}\right)}.$$

We estimated characteristic times for the temperature and velocity relaxations of the microspheres in helium and the times for the diffusion-induced gas mixing inside the microspheres (according to the relationships given in [1]). The largest values of these times, namely, of the velocity-relaxation time for the particle sizes under study (smaller than 50 μm) and the values (larger than 0.9) of the quantity β, are always lower by approximately an order of magnitude than the characteristic time of equalizing gas densities inside and outside the microspheres. This undoubtedly allows us to use the assumption about the temperature and velocity equilibrium of particles at acoustic-vibration frequencies that do not (or slightly) exceed Ω_m.

Thus, the calculations performed demonstrate that the attenuation coefficient and the sound velocity in single-temperature single-velocity mixtures consisting of gas and hollow permeable microspheres are characterized by the frequency dependence of parameters, which is typical of most media exhibiting relaxation phenomena. In our case, the relaxation process is reduced to equalizing gas densities (pressures) inside and outside the microspheres. This occurs due to the penetration of molecules through the membrane shells of the microspheres. The relaxation time for the process under consideration can be controlled by varying the microsphere size and the ratio of inner and outer radii or the shell-permeability coefficient (changing the parameters of micropores or their density). This provides the possibility to vary within a wide range the frequency corresponding to the most efficient absorption of low-frequency acoustic vibrations ($\Omega < 1000$ Hz).

REFERENCES

1. R. I. Nigmatulin, *Mechanics of Multiphase Media* (Nauka, Moscow, 1987), Part 1.
2. Yu. I. Dytnerskiĭ, V. P. Brykov, and G. G. Kagramanov, *Membrane Separation of Gases* (Khimiya, Moscow, 1991).
3. N. I. Nikolaev, *Diffusion in Membranes* (Khimiya, Moscow, 1980).
4. V. V. Budov, Steklo Keram., Nos. 7/8, 7 (1994).
5. V. D. Solodovnik, *Microcapsulation* (Khimiya, Moscow, 1980).
6. L. Ya. Kizil'shteĭn, I. V. Dubov, A. L. Shpitsgluz, and S. G. Parada, *Components of Ashes and Slags of Thermal Power Plants* (Énergoatomizdat, Moscow, 1995).
7. *Proceedings of the Lebedev Institute of Physics, Russian Academy of Sciences*, Vol. 220: *Laser Thermonuclear Targets and Ultrastrong Microballoons*, Ed. by N. G. Basov (Nauka, Moscow, 1992).
8. K. K. Ahuja and R. J. Gaeta, Jr., AIAA Pap., 97-1701 (1997).
9. S. V. Dolgushev, V. M. Fomin, and V. P. Fomichev, RF Patent No. 2161527 (2001).
10. S. P. Kiselev, E. V. Vorozhtsov, and V. M. Fomin, *Foundations of Fluid Mechanics with Applications* (Birkhauser, Boston, 1999).
11. B. F. Gordiets, A. I. Osipov, and L. A. Shelepin, *Kinetic Processes in Gases and Molecular Lasers* (Nauka, Moscow, 1980).
12. N. A. Gumerov, A. I. Ivandaev, and R. I. Nigmatulin, Dokl. Akad. Nauk SSSR **272**, 560 (1983) [Sov. Phys. Dokl. **28**, 713 (1983)].

Translated by K. Kugel

Doklady Physics, Vol. 46, No. 12, 2001, pp. 904–907. Translated from Doklady Akademii Nauk, Vol. 381, No. 6, 2001, pp. 782–785.

MECHANICS

Exact Solution to the Dirichlet Problem for a Thick Elastic Wedge-Shaped Plate

G. Ya. Popov

Presented by Academician A.Yu. Ishlinskiĭ June 25, 2001

Received June 26, 2001

We consider the problem of an elastic medium occupying the region defined by the following relationships in the cylindrical coordinate system:

$$0 \le r < \infty, \quad \varphi_0 \le \varphi \le \varphi_1, \quad h_0 \le z \le h_1. \tag{1}$$

We assume that the stresses are given at the wedge faces $\varphi = \varphi_i$ and $z = h_i$ ($i = 0, 1$). For definiteness and brevity, we suppose that

$$\sigma_\varphi\big|_{\varphi = \varphi_i} = 0, \quad \tau_{\varphi r}\big|_{\varphi = \varphi_i} = 0, \quad \tau_{\varphi z}\big|_{\varphi = \varphi_i} = 0, \quad i = 0, 1, \tag{2}$$

$$\sigma_z\big|_{z = h_i} = -p^{(i)}(r, \varphi), \quad \tau_{zr}\big|_{z = h_i} = \tau_{z\varphi}\big|_{z = h_i} = 0, \quad i = 0, 1. \tag{3}$$

1. In order to solve the problem formulated, we write out the Lamé equations in the cylindrical coordinate system. For this purpose, we introduce the notation (G is the shear modulus)

$$2G(u_r, u_\varphi, u_z) = u, V, W \tag{4}$$

and the auxiliary functions

$$\begin{Vmatrix} Z(r, \varphi, z) \\ Z^*(r, \varphi, z) \end{Vmatrix} = \frac{1}{r}\left\{\begin{Vmatrix} r & u \\ r & V \end{Vmatrix}' \pm \begin{Vmatrix} V \\ u \end{Vmatrix}^{\cdot}\right\}. \tag{5}$$

As a result, the homogeneous Lamé equations in the cylindrical coordinate system are written out in the form [1]

$$\Delta u - r^{-2}(u + 2V^{\cdot}) + \mu_0(Z' + W'') = 0,$$

$$\Delta V - r^{-2}(V - 2u^{\cdot}) + \mu_0(Z^{\cdot} + W^{\cdot\prime}) = 0,$$

$$\Delta W + \mu_0(Z' + W'') = 0, \quad \mu_0 = (1 - 2\mu)^{-1}.$$

Here, Δ is the Laplace operator in the cylindrical coordinate system; μ is the Poisson ratio; and the prime, point, and comma stand for the partial derivatives with respect to r, φ, and z, respectively.

We now transform the Lamé equations in the following manner. We multiply the first equation by r, differentiate the product with respect to r, and then divide the result by r. The second equation is differentiated with respect to φ, and the result is divided by r. The equations obtained are summed, and then the operations performed with the two equations are exchanged. As a result, the Lamé equations are reduced to the form

$$\Delta W + \mu_0(Z' + W'') = 0, \quad \Delta Z + \mu_0(\nabla Z + \nabla W') = 0, \tag{6}$$

$$\Delta Z^* = 0, \tag{7}$$

$$\nabla f(z, \varphi, z) = r^{-1}[r f'(z, \varphi, z)]' + r^{-2} f^{\cdot\cdot}(z, \varphi, z).$$

If the functions Z and Z^* entering into Eqs. (6) and (7) are found, the functions u and V related to the displacements are determined from the equations

$$\nabla\begin{Vmatrix} r & u \\ r & V \end{Vmatrix} = \frac{1}{r}\left\{\begin{Vmatrix} (r^2 Z)' \\ (r^2 Z)' \end{Vmatrix} \mp \begin{Vmatrix} Z^{*\cdot} \\ Z^{\cdot} \end{Vmatrix}\right\}. \tag{8}$$

Equations (8) are derived from Eqs. (5) with the help of the same operations that were performed with the Lamé equations, while reducing them to the form (6) and (7).

2. We impose such boundary conditions to Eqs. (6)–(8) that conditions (2) and (3) are met. To do this, we introduce the superpositions of the tangent stresses, which are similar to (5):

$$\begin{Vmatrix} \tau(r, \varphi, z) \\ \tau^*(r, \varphi, z) \end{Vmatrix} = \frac{1}{r}\left\{\begin{Vmatrix} (r\tau_{zr})' \\ (r\tau_{z\varphi})' \end{Vmatrix} \pm \begin{Vmatrix} \tau_{z\varphi} \\ \tau_{zr} \end{Vmatrix}^{\cdot}\right\}. \tag{9}$$

Using the Hooke law that relates the stresses and displacements, we obtain the following expressions in the cylindrical coordinate system:

$$2\tau = Z' + \nabla W, \quad 2\tau^* = Z^{*\prime}, \tag{10}$$

Mechnikov University,
ul. Petra Velikogo 2, Odessa, 270100 Ukraine

1028-3358/01/4612-0904$21.00

With regard to (4) and (5), the normal stress σ_z satisfies the equation

$$(1-2\mu)\sigma_z = \mu Z + (1-\mu)W'. \tag{11}$$

Similarly, the remaining stresses entering into conditions (2) obey the equations

$$\begin{gathered}\sigma_\varphi = \mu'(Z + W') + r^{-1}(V^{\cdot} + u), \quad \mu' = \mu\mu_0, \\ -2\tau_{\varphi r} = Z^* - 2V', \quad 2\tau_{\varphi z} = V' + r^{-1}W^{\cdot}.\end{gathered} \tag{12}$$

By virtue of Eqs. (9)–(11), conditions (3) are met provided that the functions Z, W, and Z^* satisfy the equations

$$\begin{gathered}\mu Z|_{z=h_i} + (1-\mu)W'|_{z=h_i} = -(1-2\mu)p^{(i)}(r, \varphi), \\ i = 0, 1, \\ \nabla W|_{z=h_i} + Z'|_{z=h_i} = 0, \quad Z^{*\prime}|_{z=h_i} = 0, \quad i = 0, 1.\end{gathered} \tag{13}$$

For conditions (2) to be satisfied, we require that the following equalities be valid:

$$\begin{gathered}W^{\cdot}(z, \varphi_i, z) = Z^{\cdot}(z, \varphi_i, z) = 0, \\ V(r, \varphi_i, z) = Z^*(r, \varphi_i, z) = 0,\end{gathered} \tag{14}$$

together with the equalities

$$\begin{gathered}-u(r, \varphi_i, z) = \mu' r[Z(r, \varphi_i, z) + W'(r, \varphi_i, z)] \\ + V^{\cdot}(r, \varphi_i, z) = 0, \quad i = 0, 1.\end{gathered} \tag{15}$$

3. As is seen, the boundary conditions for Eq. (17) turn out to be homogeneous; hence,

$$Z^*(r, \varphi, z) \equiv 0. \tag{16}$$

For solving the system of equations (6) with boundary conditions (14), we carry out the integral transformation ($\varphi_0 = 0$)

$$\begin{gathered}\left\| \begin{matrix} u_n(r, \theta) \\ Z_n(r, \theta) \end{matrix} \right\| = \int_0^{\varphi_1} \cos\mu_n\varphi \left\| \begin{matrix} u(r, \theta, \varphi) \\ Z(r, \theta, \varphi) \end{matrix} \right\| d\varphi, \\ \mu_n = \frac{\pi(n-1)}{\varphi_1}, \quad n = 1, 2, \ldots.\end{gathered} \tag{17}$$

The inverse transformations have the form [2]

$$\left\| \begin{matrix} u(r, \theta, \varphi) \\ Z(r, \theta, \varphi) \end{matrix} \right\| = \frac{2}{\varphi_1}\sum_{n=1}^{\infty}{}' \cos\mu_n\varphi \left\| \begin{matrix} u_n(r, \theta) \\ Z_n(r, \theta) \end{matrix} \right\|. \tag{18}$$

Here, the prime implies that the first term should be doubled.

As a result, the system of equations (6) takes the form

$$\begin{gathered}\mu_* W_n'' - \nabla_n W_n + \mu_0 Z_n' = 0, \quad \mu_* = 2(1-\mu)\mu_0, \\ Z_n'' - \mu_* \nabla_n Z_n - \mu_0 \nabla_n W_n' = 0, \\ \nabla_n f(r, z) = \frac{\mu_n^2}{r^2} f(r, z) - \frac{[r f'(rz)]'}{r}, \quad n = 1, 2, \ldots,\end{gathered} \tag{19}$$

where μ_n is given by (17). In this case, conditions (13) are transformed into the following equalities:

$$\begin{gathered}\mu Z_n(r, h_i) + (1-\mu)W_n'(r, h_i) = -(1-2\mu)p_n^{(i)}(r), \\ Z_n'(r, h_i) - \nabla_n W_n(r, h_i) = 0, \quad i = 0, 1, \\ p_n^{(i)}(r) = \int_0^{\varphi_1} \cos\mu_n\varphi p^{(i)}(r, \varphi)d\varphi, \\ \mu_n = \frac{\pi(n-1)}{\varphi_1}, \quad n = 1, 2, \ldots.\end{gathered} \tag{20}$$

We then apply to Eqs. (19) and (20) the Hankel integral transformation

$$\begin{gathered}\left\| \begin{matrix} W_{n\beta}(z) \\ Z_{n\beta}(z) \end{matrix} \right\| = \int_0^{\infty} r J_\mu(\beta r) \left\| \begin{matrix} W_n(r, z) \\ Z_n(r, z) \end{matrix} \right\| dr, \\ \mu = \mu_n = \frac{\pi(n-1)}{\varphi_1}, \quad n = 1, 2, \ldots.\end{gathered} \tag{21}$$

The inverse transformations have the form

$$\left\| \begin{matrix} W_n(r, z) \\ Z_n(r, z) \end{matrix} \right\| = \int_0^{\infty} \beta J_\mu(\beta r) \left\| \begin{matrix} W_{n\beta}(z) \\ Z_{n\beta}(z) \end{matrix} \right\| d\beta. \tag{22}$$

As a result, instead of (19), we have

$$\begin{gathered}\mu_* W_{n\beta}''(z) - \beta^2 W_{n\beta}(z) + \mu_0 Z_{n\beta}'(z) = 0, \\ Z_{n\beta}''(z) - \mu_* \beta^2 Z_{n\beta}(z) + \mu_0 \beta^2 W_{n\beta}'(z) = 0, \\ h_0 < z < h_1,\end{gathered} \tag{23}$$

and boundary conditions (20) are transformed into the following equalities:

$$\begin{gathered}\mu Z_{n\beta}(h_i) + (1-\mu)W_{n\beta}'(h_i) = -(1-2\mu)p_{n\beta}^{(i)}, \\ Z_{n\beta}'(h_i) - \beta^2 W_{n\beta}(h_i) = 0, \quad i = 0, 1.\end{gathered} \tag{24}$$

The transform $p_{n\beta}^{(i)}$ is found from a formula similar to (21).

It can be directly verified that the functions

$$W_{n\beta}(z) = e^{-\beta z}(C_0 + C_1 z) + e^{\beta z}(C_2 + C_3 z),$$
$$Z_{n\beta}(z) = e^{-\beta z}(\beta C_0 - \kappa C_1 + \beta z C_1) - e^{\beta z}(\beta C_2 + \kappa C_3 + \beta z C_3), \quad (25)$$

with $\kappa = 3 - 4\mu$, are the general solution to system (23). Here, C_j are arbitrary constants ($j = 0, 1, 2, 3$).

Substituting (25) into boundary conditions (24), we find these constants:

$$\Delta_\beta \beta C_0 = P_{n\beta}^{(1)} e_\beta^{(1)} - P_{n\beta}^{(0)} e_\beta^*,$$
$$\Delta_\beta C_1 = 2P_{n\beta}^{(1)} e_\beta^{(0)} + P_{n\beta}^{(0)} e_\beta^{(2)},$$
$$(h_1 - h_0)_\beta \Delta_\beta C_2 = 2e_\beta^{(0)} P_{n\beta}^{(1)}(e_\beta^{(5)} + e_\beta^*) + P_{n\beta}^{(0)}(e_\beta^{(2)} e_\beta^{(5)} + e_\beta^* e_\beta^{(4)}), \quad (26)$$
$$(h_0 - h_1)_\beta \Delta_\beta C_3 = e_\beta^{(0)} P_{n\beta}^{(1)}(2e_\beta^{(3)} + e_\beta^{(1)}) + P_{n\beta}^{(0)}[2e_\beta^{(0)} e_\beta^* + e_\beta^{(2)}(e_\beta^{(3)} + e_\beta^{(1)})].$$

Here, we use the following notation:

$$\Delta_\beta = 2e_\beta^{(0)} e_\beta^* + e_\beta^{(1)} e_\beta^{(2)}, \quad P_{n\beta}^{(0)} = e^{-\beta h_1} p_{n\beta}^{(1)} - e^{-\beta h_0} p_{n\beta}^{(0)},$$
$$P_{n\beta}^{(1)} = e^{-\beta h_1}(\mu_0^* - 1) p_{n\beta}^{(1)} - e^{-\beta h_0}(\mu_1^+ - 1) p_{n\beta}^{(0)},$$
$$e_\beta^{(0)} = e^{-2\beta h_0} - e^{-2\beta h_1}, \quad e_\beta^{(1)} = \kappa_0^- e^{-2\beta h_0} - \kappa_1^- e^{-2\beta h_1},$$
$$e_\beta^{(2)} = \kappa_0^+ e^{-2\beta h_1} - \kappa_1^+ e^{-2\beta h_0},$$
$$e_\beta^{(3)} = \mu_0^- e^{-2\beta h_0} - \mu_1^- e^{-2\beta h_1}, \quad e_\beta^{(4)} = \mu_0^+ e^{-2\beta h_1} - \mu_1^+ e^{-2\beta h_0},$$
$$e_\beta^{(5)} = \mu_0^- \mu_1^+ e^{-2\beta h_0} - \mu_0^+ \mu_1^- e^{-2\beta h_1}, \quad (27)$$
$$e_\beta^* = \Delta_\beta^+ e^{-2\beta h_0} - \Delta_\beta^- e^{-2\beta h_1},$$
$$\mu_i^\mp = 2(1-\mu) \mp \beta h_i, \quad \kappa_i^\mp = \kappa \mp 2\beta h_i,$$
$$\Delta_\beta^\mp = a_\mu \mp \kappa\beta(h - h_0) - \beta^2 h_0 h_1,$$
$$a_\mu = 4(1-\mu)^2 + (1-2\mu)^2, \quad i = 0, 1.$$

Formulas (25)–(27) completely determine the transforms. Using inverse formulas (22) and (18), we can then find the functions $W(r, \varphi, z)$ and $Z(r, \varphi, z)$.

It remains to determine the functions $u(r, \varphi, z)$ and $V(r, \varphi, z)$ and to satisfy both condition (15) and

$$V(r, \varphi_i, z) = 0, \quad i = 0, 1. \quad (28)$$

4. To do this, we use Eqs. (8) with due regard to (16). Introducing the notations

$$rU(r, \varphi, z) = u^*(r, \varphi, z),$$
$$rV(r, \varphi, z) = V^*(r, \varphi, z), \quad (29)$$

we reduce boundary conditions (25) and (15) to the following equalities:

$$V^*(r, \varphi_i, z) = 0,$$
$$-u^*(r, \varphi_i, z) = F^{(i)}(r, z), \quad i = 0, 1, \quad (30)$$

where

$$F^{(i)}(r, z) = \mu' r^2 [Z(r, \varphi_i, z) + W'(r, \varphi, z)] + V^{*\cdot}(z, \varphi_i, z). \quad (31)$$

In order for conditions (30) to also be satisfied [with allowance for (29) and (16)], we apply to Eqs. (8) the integral transformation obtained from integral transformation (17) by the substitution in it of the sine and ν_n for the cosine and μ_n ($\nu_n = n\pi\varphi_1^{-1}$, $n = 1, 2, \ldots$). The inversion formulas for such a transformation are the following (see [2]):

$$\begin{Vmatrix} u^*(r, \varphi, z) \\ V^*(r, \varphi, z) \end{Vmatrix} = \frac{2}{\varphi_1} \sum_{n=1}^{\infty} \sin \nu_n \varphi \begin{Vmatrix} u_n^*(r, z) \\ V_n^*(r, z) \end{Vmatrix}. \quad (32)$$

As a result, the integral transform of Eqs. (8) takes the form

$$-\nabla_n^* u_n^*(r, z) = \frac{(r\bar{Z}_n)'}{r} - \nu_n \sum_{i=0}^{1} \frac{\cos \nu_n \varphi_i F^{(i)}(r, z)}{r^2}, \quad (33)$$

$$-\nabla_n^* V_n^*(r, z) = -\nu_n \int_0^{\varphi_1} Z(r, \varphi, z) \cos \nu_n \varphi d\varphi \quad (\varphi_0 = 0). \quad (34)$$

Here, the operator ∇_n^* is obtained by the substitution of ∇_n for μ_n in ν_n. The function $\bar{Z}_n$ is determined by formula (17), in which the cosine and μ_n should be substituted by the sine and ν_n, respectively.

To solve Eqs. (33) and (34), we use the Hankel transformation

$$\begin{Vmatrix} u_{n\beta}^*(z) \\ V_{n\beta}^*(z) \end{Vmatrix} = \int_0^{\infty} r J_\nu(r\beta) \begin{Vmatrix} u_n^*(r, z) \\ V_n^*(r, z) \end{Vmatrix} dr, \quad (35)$$
$$\nu = \nu_n = \frac{\pi n}{\varphi_1}, \quad n = 1, 2, \ldots.$$

With due regard for Eq. (34), we have

$$V^*_{n\beta}(z) = \frac{\nu}{\beta^2}\int_0^{\varphi_1}\int_0^{\infty} Z(\rho, \psi z)\cos(\nu\psi)\rho J_\nu(\beta\rho)d\psi d\beta.$$

Using formula (22), with ν substituted for μ, and inversion formula (32), we arrive at

$$V^*(r, \varphi, z) = \int_0^{\varphi_1}\int_0^{\infty} Z(\rho, \psi, z) \times [\Phi^{\cdot}(r, \rho, \varphi - \psi) - \Phi^{\cdot}(r, \rho, \varphi + \psi)]d\psi d\rho, \quad (36)$$

where

$$\Phi(r, \rho, \theta) = \frac{1}{\varphi_1}\sum_{n=1}^{\infty}\cos\frac{\theta\nu}{2}\int_0^{\infty}\frac{J_\nu(\beta r)J_\nu(\beta\rho)}{\beta}d\beta, \quad \nu = \frac{\pi n}{\varphi_1}, \quad n = 1, 2, \ldots. \quad (37)$$

Thus, the function $F^{(i)}(r, z)$ ($i = 0, 1$) entering into the right-hand side of Eq. (33) is completely determined. Solving this equation with the use of integral transformation (35), we have

$$u^*_{n\beta}(z) = \frac{1}{\beta^2}\left[\int_0^{\infty} r\bar{Z}_n J_\nu(r\beta)dr + \nu\sum_{i=0}^{1}\cos\nu\varphi_i\int_0^{\infty}\frac{F^{(i)}(r, z)}{r}J_\nu(r\beta)dr\right],$$

$$\varphi_0 = 0, \quad \nu = \pi n\varphi_1^{-1}, \quad n = 1, 2, \ldots.$$

Using the same inversion formulas as with Eq. (36), we obtain the solution

$$u^*(r, \varphi, z) = \int_0^{\varphi_1}\int_0^{\infty} Z(\rho, \psi, z) \times\left[\frac{\partial\Phi(\varphi - \psi, r, \rho)}{\partial\rho} - \frac{\partial\Phi(\varphi + \psi, r, \rho)}{\partial\rho}\right]d\psi d\rho + \sum_{i=1}^{1}\int_0^{\infty}\frac{F^{(i)}(\rho, z)}{\rho}[\Phi^{\cdot}(\varphi_i - \psi, r, \rho) - \Phi^{\cdot}(\varphi_i - \psi, r, \rho)]d\rho, \quad (38)$$

$$\varphi_0 = 0.$$

Formulas (38) and (36), together with (29) and (4), determine the displacements u_r and u_φ at any point of region (1). The third displacement, u_z, is already determined by formulas (25) and (26) with regard to (22), (18), and (4). Thus, we obtain an exact solution to the formulated problem. The solution depends on three arbitrary parameters, φ_1, h_0, and h_1. For a series of important particular cases, the solutions can be obtained by specifying these parameters. For example, we consider the problem of an elastic semi-infinite wedge ($0 \le r < \infty$, $0 \le \varphi \le \varphi_1$, $0 \le z < \infty$) under a normal load applied to the side $z = 0$. The solution to this problem is described by the formulas presented above, with $h_0 = 0$ and h_1 tending to infinity. As a result, instead of (25) and (26), we have the simpler formulas

$$\begin{Vmatrix} W_{n\beta}(z) \\ Z_{n\beta}(z) \end{Vmatrix} = p^{(0)}_{n\beta}e^{-\beta z}\begin{Vmatrix} 2(1-\mu)\beta^{-1} + z \\ \beta z - 1 + 2\mu \end{Vmatrix}.$$

Hence, all the formulas are also simplified. If we set $\varphi_1 = \pi$ in the formulas obtained, we arrive at the solution to the problem of a fourth of the elastic space under a normal load applied to one of its sides.

REFERENCES

1. W. Nowacki, *Theory of Elasticity* (PWN, Warsaw, 1970; Mir, Moscow, 1975).
2. N. A. Martynenko and L. M. Pustyl'nikov, *Finite Integral Transformations and Their Application to Studying the Systems with Distributed Parameters* (*Handbook*) (Nauka, Moscow, 1986).
3. É. M. Kartashov, *Analytical Methods in Heat Conductivity of Solids* (Vysshaya Shkola, Moscow, 1979).

Translated by V. Chechin